Inorganic Building Blocks for the Synthesis of Self-Healing Nanocomposites based on Diels-Alder Reaction

Dissertation

Zur Erlangung des Grades des Doktors der Naturwissenschaften der Naturwissenschaftlich-Technischen Fakultät III, Chemie, Pharmazie, Bio- und Werkstoffwissenschaften der Universität des Saarlandes

vorgelegt von

Tom Engel

Saarbrücken,

Juni 2015

Tag des Kolloquiums: 30. Oktober 2015

Dekan: Prof. Dr.-Ing. Dirk Bähre

Berichterstatter: Prof. Dr. Guido Kickelbick

     Prof. Dr. Gerhard Wenz

Vorsitz: Prof. Dr. David Scheschkewitz

Akad. Mitarbeiter: Dr. Bernd Morgenstern

für Martine

Die vorliegende Arbeit entstand in der Zeit von Juni 2010 bis August 2014 im Institut für Anorganische Festkörperchemie an der Universität des Saarlandes im Arbeitskreis von Herrn Prof. Dr. Guido Kickelbick.

Danksagung

Ich möchte mich auch bei meinen Kollegen und Kolleginnen aus Wien, Christoph, Angelika, Jakob und Bernhard bedanken, die mir während ihrer Gastaufenthalte in Saarbrücken viel Unterstützung boten.

Dank gilt meinen Freunden, Thierry, Eric, Laurent, Christophe, Jo, Joël und Christiane für die notwendige Ablenkung an den Wochenenden.

Großer Dank gilt meinen Eltern, die mir Schule, Studium und Leben ermöglichten. Sie standen immer hinter meinen Entscheidungen und unterstützten mich. Danke!

Vielen Dank, meine liebste Martine, dass Du immer für mich da warst, Dich mit mir gefreut und mich getröstet hast. Danke für Deine Liebe und Deine Geduld!

Kurzzusammenfassung

Die vorliegende Arbeit untersucht die Möglichkeit funktionelle anorganische Nanobausteine als Vernetzungsvermittler für selbstheilende Materialien zu verwenden. Intelligente Polymere und Verbundwerkstoffe, welche die reversible Diels-Alder-Reaktion zur intrinsischen Selbstheilung von Materialdefekten nutzen, gehören einer neuartigen Materialklasse an. Maleimid- und Furanfunktionalitäten dienen zur reversiblen Vernetzung von anorganischen Nanopartikeln und Polymermatrix. Das eigentliche Ziel ist die Bestimmung von universell geeigneten Techniken zur Herstellung von thermoreversibel vernetzbaren Hybridmaterialien.

Zunächst wurde gezeigt, dass sterische Oberflächeneffekte an SiO_2-Nanopartikel, welche mit kurzen Silankupplungsreagenzien mit Maleimidfunktionalitäten modifiziert wurden, nur sehr geringe Diels-Alder-Reaktivität erlauben. Oberflächeninitiierte radikalische Atomtransferpolymerisation wurde genutzt um Kern-Schale Nanopartikel mit erhöhter Reaktivität zu erzeugen. Durch den Gebrauch von Methacrylsäurebutylester als Comonomer wurde die Glasübergangstemperatur herabgesetzt und die Distanz zwischen den Vernetzungspunkten wurde erhöht. Außerdem wurden Hybridmaterialen basierend auf käfigartigen kubischen Spherosilikaten hergestellt. Die Art des Vernetzers bestimmte die mechanischen Eigenschaften sowie die Selbstheilungsfähigkeit.

Den Beweis für eine erfolgreiche Selbstheilung der Hybridmaterialien lieferte die Heilung von Oberflächenkratzern nach thermischer Behandlung.

Abstract

This work investigates the possibility to employ functional inorganic nano building blocks as cross-linking agents for self-healing materials. Smart polymers and composites using reversible Diels-Alder reaction as mechanism for intrinsic self-healing of defects represent a novel class of materials. Maleimide and furan functionalities have been selected to ensure Diels-Alder reaction between inorganic nanoparticles and polymeric matrix. The ultimate goal was to identify universally suitable techniques to prepare thermally remendable hybrid materials.

Initially, surface-modification of silica nanoparticles with short silane coupling agents containing maleimide functionalities displayed low Diels-Alder conversion because of steric effects on the surface. Surface-initiated atom transfer radical polymerization yielded core-shell nanoparticles with increased reactivity by utilizing butyl methacrylate as comonomer to lower glass transition temperature and increase the distance between cross-links. Additionally, two hybrid materials based on cage-like cubic spherosilicates were prepared. Mechanical properties as well as self-healing abilities could be tuned by the choice of the cross-linker.

Spectroscopic, thermal and mechanical analytical tools displayed the extent of the Diels-Alder reaction during curing as well as the reversibility of the cross-linking. Healing of surface scratches by thermal treatment provided evidence for successful self-healing properties of the hybrid materials.

ABBREVIATIONS

AFM	atomic force microscopy
APTES	3-aminopropyltriethoxysilane
ARGET	activators regenerated by electron transfer
ATR	attenuated total reflectance
ATRP	atom transfer radical polymerization
BF	ethane-1,2-diyl difuran-2-carboxylate
BMA	butyl methacrylate
BMI	bismaleimide
CP	cyclopentadiene
D	molecular diffusion coefficient
DA	Diels-Alder
DCDC	double cleavage drilled compression
DCP	dicyclopentadiene
DGBEA	diglycidyl ether of bisphenol A
DLS	dynamic light scattering
DMA	dynamic mechanical analysis
DSC	differential scanning calorimetry
ESR	electron spin resonance
EXAFS	extended X-ray absorption fine structure
FAE	furfuryl allyl ether
FMA	furfuryl methacrylate
FTIR	Fourier transform infrared
FUPTES	1-(furan-2-ylmethyl)-3-(triethoxysilyl)urea
HDA	hetero-Diels-Alder
HMTETA	1,1,4,7,10,10-hexamethyltriethylenetetramine
HOMO	highest occupied molecular orbital
hrs	hours
IBMK	isobuthyl methyl ketone
IPN	interpenetrating polymer network
K	Kelvin
LUMO	lowest unoccupied molecular orbital

M	molecular weight
min	minute/minutes
MPTES	N-((3-triethoxysilyl)-propyl)maleimide
M_w	mass weighted molecular weight
NMR	nuclear magnetic resonance
PBMA	poly(butyl methacrylate)
PCL	poly(ε-caprolactone)
PCMS	polychloromethylstyrene
PDI	polydispersity index
PDMS	polydimethylsiloxane
PFCB	perfluorocyclobutane
PMDETA	*N,N,N',N',N''*-pentamethyldiethylenetriamine
pMiMA	protected maleimide methacrylate
PMMA	poly(methyl methacrylate)
pMPGE	poly(methacrylated phenyl glycidyl ether)
POSS	polyhedral oligomeric silsesquioxanes
PPFCP	poly(perfluorocyclobutane)
PVC	poly(vinyl chloride)
rDA or RDA	retro-Diels-Alder
RHDA	retro-hetero-Diels-Alder
ROMP	ring opening metathesis polymerization
RT	room temperature
SEC	size-exclusion chromatography
SFRP	stable free radical polymerization
SI-ATRP	surface initiated atom transfer radical polymerization
TEM	transmission electron microscopy
TEMPO	2,2,6,6-tetramethyl-1-piperidinyloxy
TEOS	tetraethylorthosilicate
TFVE	trifluorovinylether
T_g	glass transition temperature
TGA	thermogravimetric analysis
T_m	melting point/melting temperature

TABLE OF CONTENT

1   INTRODUCTION

1.1   Self-Healing Materials

All natural and artificial materials are exposed to mechanical, thermal and chemical influences. In consequence, degradation over time can lead to fatigue, which results in deterioration of mechanical properties up to complete failure. Structural elements of machines may undergo periodic deformations causing micro-cracks, which propagate with every movement leading to bigger and bigger defects.[1, 2] Besides mechanical degradation by abrasion caused by contact with harder materials, coatings are mainly affected by atmospheric influences e.g., light, temperature changes and oxidations.[3-5] Differences in the thermal expansion coefficients of the coating and the substrate may cause crack formation. Normally these damages would involve a replacement of the damaged parts or renewal of the coating.

Nature developed various techniques to heal injuries, from the "bleeding" of the rubber tree to close the end of broken branches, up to the numerous stages involved during the healing of bone fractures.[6]

A chemist dream is to mimic such self-healing behavior within engineered polymeric and composite materials using physical and chemical mechanisms. Self-healing materials were defined by White et al.: "Self-healing materials exhibit the ability to repair themselves and to recover functionality using resources inherently available to them […] whether the repair process is autonomic or externally assisted (e.g., by heating)."[7]

This ingenious new class of materials offers a road towards renewable, longer-lasting products for various applications e.g., coatings in electronics, aeronautics and the automotive industry.[8-14] Unlike thermoplastic materials, standard thermosets irreversibly cure and cannot be melted to be shaped differently. In the event of a

failure, the absence of plastic flow prevents healing by rearrangement of polymer chains. By incorporation of healing additives or functionalities, chemists and material engineers are able to create a new class of materials.

Three main self-healing principles have been identified. Capsule based self-healing and vascular self-healing appertain to the class of extrinsic self-healing, needing secondary healing agents do perform the repair of damage. The third category is composed of intrinsically self-healing materials.[7]

1.2 Self-Healing Approaches

1.2.1 Capsule-based self-healing

Capsule based self-healing approaches enclose a liquid healing agent in spherical capsules until a damage triggers breaking of the reservoirs and release of the healing agent (Figure 1). Different encapsulation techniques and a great variety of healing agents have been employed. Encapsulation in the case of self-healing materials is mainly achieved by forming a solid polymer shell at the interface of droplets in an oil-water emulsion. The polymer can be formed by *in situ* polycondensations (urea-formaldehyde, melamine-formaldehyde) or polyadditions (polyurethane).[15-24] Another successful technique proceeds by the dispersion of the healing agent in a molten polymer followed by emulsification and solidification by temperature decrease. This technique is called meltable dispersion encapsulation.[25]

Different healing mechanisms were used involving one or more encapsulated liquid healing agents. White et al. used ring opening metathesis polymerization (ROMP) with encapsulated dicyclopentadiene.[26] Grubbs catalyst necessary for the reaction was previously dispersed within the polymer matrix. Other groups used epoxy-resin filled capsules in combination with an imidazole catalyst that could be thermally activated.[27]

In the multicapsule-based systems, both the healing agent and the polymerizer are encapsulated separately. Keller et al. established multicapsule self-healing in elastomeric matrix by employing platin-catalysed hydrosilation reaction of vinyl-terminated polydimetylsiloxane (PDMS).[18, 28] Later, multicapsule healing was extended to spatially separated epoxide and mercaptane.[29]

A third approach in the field of capsule-based self-healing uses remaining latent functionalities of the polymeric matrix that is to be repaired. An example is the solvent-promoted self-healing of remaining amine-functionalities within an epoxy matrix. Caruso et al. tested different encapsulated solvents that trigger self-healing by swelling of the polymeric matrix, thereby facilitation addition of amine to epoxide.[30, 31] The results suggested that polar aprotic solvents are best suited to promote healing.

Disadvantages of capsule-based self-healing mechanism are the non-repeatability of self-healing, the deterioration of the mechanical properties by incorporation of macroscopic capsules and the need to tune the mechanical properties of the capsule shell. Once the healing agent is depleted, no more self-healing can be observed at the same position. Another important requirement in the design of crack-healing material is that the fracture toughness of the capsule shell and the fracture toughness of the matrix matches.[32] If they do not match, the crack will be deflected around the capsules without harming it.
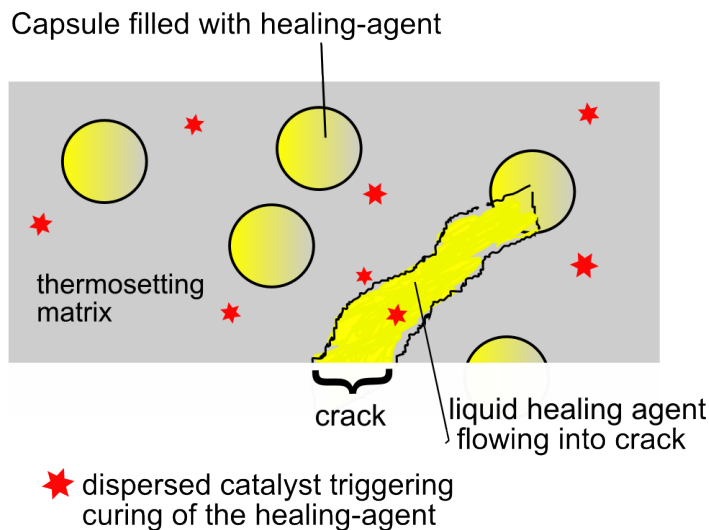
FIGURE 1: SCHEMATIC REPRESENTATION OF CAPSULE-BASED SELF-HEALING

1.2.2 Vascular self-healing

Vascular self-healing materials use hollow channels in 1D, 2D or 3D orientation as reservoirs for healing agent storage (Figure 2). These systems mimic the blood vessels within living tissue. 1D-systems were achieved by incorporation of hollow glass fibers, filled with a healing agent.[33-38] 2D and 3D vascular systems can be constructed by building a sandwich-like material out of polymer sheets topped with

silicone or poly (vinyl chloride) (hetero-DA) tubing acting as channels.[39] A more elegant technique is direct-ink writing of the channels within an uncured polymer precursor.[40, 41] After solidification the ink-scaffold is removed, which leaves hollow channels within the polymer matrix. Connectivity of the channels can easily be controlled, thereby facilitating refilling of the network and increasing the volume of accessible healing agent. The same healing agents and healing mechanisms as presented in chapter 1.2.1 can be applied. Only some properties, like surface wettability and viscosity may play a role in the choice of the healing agent, because these properties as well as the interconnectivity and the size of the channels affect the efficiency of filling and release in case of damage. [42-44]
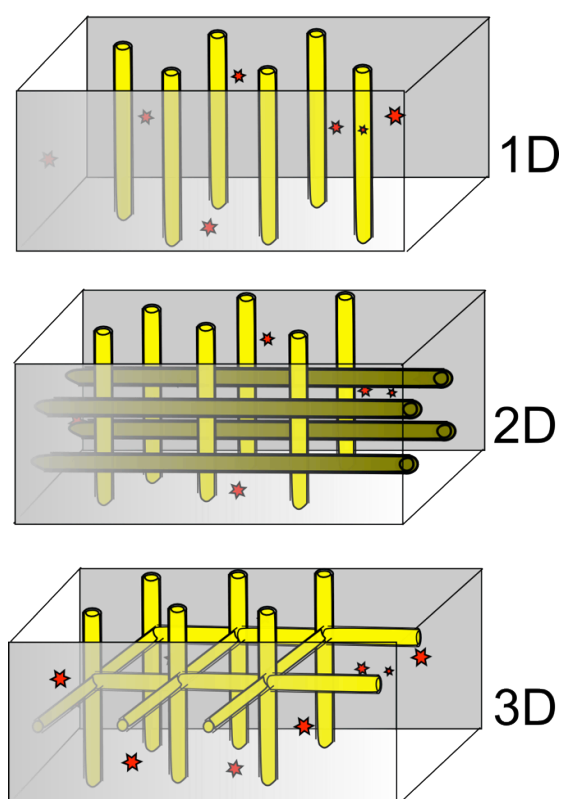
FIGURE 2: SCHEMATIC REPRESENTATION OF VASCULAR SELF-HEALING MATERIALS. CURING OF HEALING-AGENT IS TRIGGERED BY CATALYST DISPERSED IN THE MATRIX (REPRESENTED BY STARS).

1.2.3   Intrinsic self-healing

Intrinsic materials come as close to the definition of self-healing materials as possible. They use functionalities that are directly incorporated into the material to allow bonding and de-bonding. These reversible bonds can be physical, covalent, ionic or hydrogen bonds. No incorporation of extrinsic bodies, which will deteriorate the

mechanical properties of the matrix, is necessary. No capsules or channels are needed. Blending of a cross-linked polymer matrix with a linear polymer enables healing by physical rearrangement and entanglement.[45-47] Functionalization of the polymer backbone with pendant groups that are able to form reversible bonds affords a chemical way to heal damage upon a trigger.[48-50] The trigger that is needed is the only drawback of intrinsic systems. In order to break bonds, it is necessary to introduce energy in some form to the system. This may be thermal, chemical, photochemical or mechanical energy. Thermal energy is most commonly used and the easiest method to trigger bonding and de-bonding in self-healing materials. In the next chapter different intrinsic self-healing techniques involving a thermal trigger are summarized.

1.3   Principles of Thermal Healing

1.3.1   Physical Methods

Physical self-healing mechanisms involve a repair of physical damage by interdiffusion of polymer chains at crack interfaces. No chemical bonds are formed or broken during this process. Only physical links between entangled macromolecular chains are released, rearranged and new entanglements form after diffusion of chain segments across crack interfaces.

1.3.2   Molecular Diffusion across Crack Interface

Self-healing of thermoplastic polymers through molecular diffusion across crack interfaces has been extensively studied in the 1980s. The research covers amorphous, semi-crystalline block copolymers and composites. Bringing two pieces of the same polymer in contact at a temperature higher than the glass transition temperature T_g, results in a gradual disappearance of the crack interface and an increase in strength at the healing site due to interdiffusion of polymer chains. [51]

Jud and Kausch investigated the crack-healing behavior of a series of PMMA samples differing in their molecular weights. The interpenetration is strongly dependent on the temperature, the healing-time and molecular weight of the polymer. [52] Healing occurs already at 5 K above T_g but the effect is much faster if the system is heated

15 K above T_g. A slight normal pressure on the sample is needed to insure the initial contact between fracture surfaces. The amount of pressure depends on the molecular weight because the stiffness increases with M_w. After 1 min penetration time, two surfaces brought together establish a bond, which is considerably stronger than that of pure adhesion. [52] In short time experiments, fracture strength comparable to the initial strength of the material was regained quickly. On the other hand, long time experiments showed that the optically healed samples fail 10 times faster than the original material. This means that no fully entangled network has been established in the crack region and an interdiffusion of chain segments rather than that of whole polymer chains is responsible for the regain of strength. [51] The effect of the time expired between the formation of the crack and the re-healing was investigated. Immediate (several minutes) penetration led to a much faster healing process than a penetration delay of several days. There has to be some reorganization of chain ends at the crack surfaces and surface reactions cannot be excluded. [52]

Different models were established to explain the dynamics of concentrated polymer systems and the phenomenon of crack healing at thermoplastic interfaces. [53-55] According to the reptation model (a chain in a tube) introduced by de Gennes (Figure 3), the molecular diffusion coefficient D of a polymer chain is proportional to M^{-2}. [53] The reptation model predicts the dependence between thermal motions of entangled macromolecules in polymer melts or concentrated polymer solutions and the molecular weight. Movements of chains are constrained and therefore the macromolecules need to move in a snake-like fashion. In particular, Wool and O'Connor used the reptation model to determine a recovery ratio of mechanical properties. Their five stages model consists of rearrangement, surface approach, wetting, diffusion and randomization. [55]
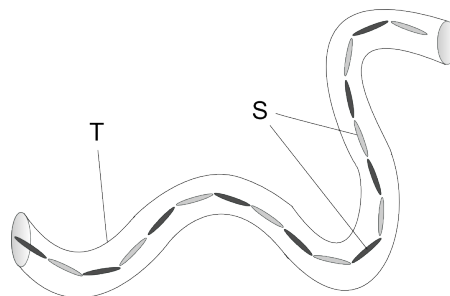
FIGURE 3: A POLYMER CHAIN P COMPOSED OF SEGMENTS S CANNOT MOVE SIDEWAYS. THE CHAIN IS TRAPPED IN A VIRTUAL TUBE T AND CAN ONLY MOVE BY REPTATION.

1.3.3 Interpenetrating Networks

Another physical thermally engaged self-healing mechanism uses thermoplastic polymers as a system to heal thermosets. These interpenetrating polymer networks (IPN) are composed of a cross-linked thermosetting polymer network and an interpenetrating linear polymer (Figure 4). Upon heating, diffusion of linear polymer to the crack interface promoted closure of the rupture. They use the concepts of molecular diffusion extended to heal materials that are inherently unable to move across crack interfaces.
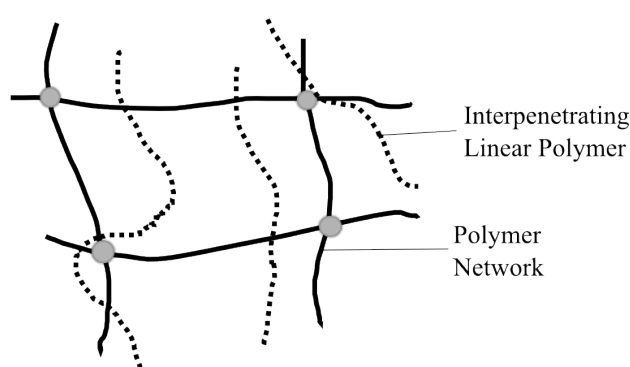
FIGURE 4: SEMI-INTERPENETRATING POLYMER NETWORK (SIPN)

Palmese et al. formulated an *in situ* sequential synthesis of an IPN using diglycidyl ether of bisphenol A (DGEBA) cured with 4,4'-methylene biscyclohexanamine as the cross-linked phase and poly(methacrylated phenyl glycidyl ether) (pMPGE) as the linear polymer phase. [45] Using soxhlet extraction, they showed first of all that the linear polymer is mobile within the network, which is a necessary condition for the self-healing mechanism. The incorporation of the linear polymer chains allowed increasing retention of healing capacity over additional healing cycles.

Hayes et al. mixed a commercially available thermosetting epoxy resin with a linear thermoplastic poly(bisphenol-A-co-epichlorohydrin). The matrix system can be induced to regain up to 70% of its virgin properties upon healing by raising the temperature above 140 °C after a fracture event has been demonstrated. [46]

Luo et al. blended two non-miscible materials, an epoxy network and poly(ε-caprolactone) (PCL). The phase-separated blend has "a bricks and mortar" morphology with polyepoxide spheres in a PCL matrix. On heating the PCL "mortar"

melts and wets all free surfaces and cracks. On cooling, recrystallization of PCL closes cracks and even two separated pieces could be reattached to each other. [47]

1.3.4 Shape Memory assisted Self-Healing

The shape memory effect in polymers permits a polymeric piece to be deformed to a temporary shape until later being triggered to return to its original shape when stimulated by external heating or other means. [56, 57]

For semi-crystalline networks crystallites serve as physical cross-links that can temporary fixate a deformation below the melting point T_m and the permanent shape may be recovered when the sample is heated above T_m. Beyond the melting point rubber elasticity, resulting from permanent covalent cross-links, is responsible for the return to the initial shape. In particular, the cross-links serve as permanent anchors for the network chains to return to their state of highest conformational entropy. [58]

Mather et al. used shape memory effect to assist in the self-healing process. Their strategy is demonstrated in a blend system consisting of cross-linked PCL network and linear PCL interpenetrating the network. The shape memory closes any cracks formed during deformation and the linear chains diffuse to the crack interface where they re-entangle during the same heating step. [59]

1.3.5 Chemical Methods

Contrary to physical self-healing mechanisms, chemical methods require breaking and regeneration of new chemical bonds. Reversible ionic and supramolecular networks are able to form very flexible cross-linking. Many studies have been carried out investigating these possibilities. In this work, only mechanisms involving reversible covalent bonds will be mentioned.

1.3.6 Thermoreversible Mechanisms

Thermoreversible mechanisms involve chemical reactions forming reversible bonds. Formation or breakage of covalent bonds is controlled by temperature. At low temperature cross-linking or polymerization occurs. Increase in temperature above a critical temperature causes the back reaction, breaking up the previously formed

bonds. This critical temperature dictates a temperature range for application. The material can only be employed at temperatures below which the material does not lose any of its mechanical stability. Ideally, the back reaction occurs at a higher temperature to allow application at room temperature or above room temperature.

1.3.7   Diels-Alder Reactions

Diels-Alder (DA) chemistry has been widely used to synthesize self-healing materials. One of the most relevant aspects of the DA reaction for re-mendable polymers is its thermal reversibility, known as the retro-Diels–Alder (RDA) reaction. [60] Different systems were investigated e.g. dicyclopentadiene, maleimide/furan, Hetero-DA (HDA) (Scheme 1).
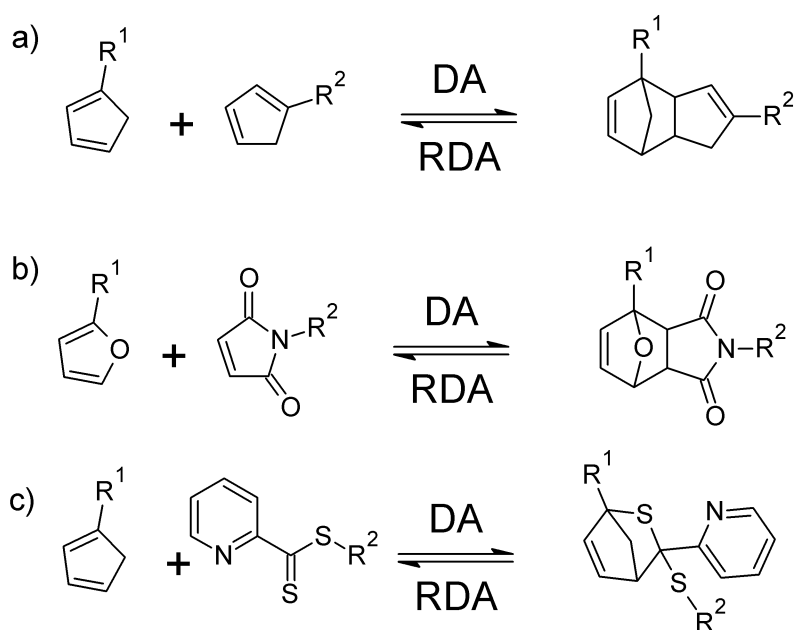
SCHEME 1: DIELS-ALDER/RETRO-DIELS-ALDER EQUILIBRIUM BETWEEN A) TWO CYCLOPENTADIENES B) FURAN AND MALEIMIDE C) CYCLOPENTADIENE AND PYRIDINYLDITHIOFORMATE (HDA).

The DA reaction is a thermoreversible [4+2]-cycloaddition involving diene and dienophile reactants. DA reaction enables the formation of two carbon–carbon bonds in a specific manner to form a cyclic (bicyclic) product. Electrons move simultaneously in a cyclic fashion without the need of intermediates. The DA reaction proceeds in a single step, simply on heating. The transition state has six delocalized

π–electrons and is therefore somewhat aromatic in character, stabilizing the transition to the DA product (Scheme 2).
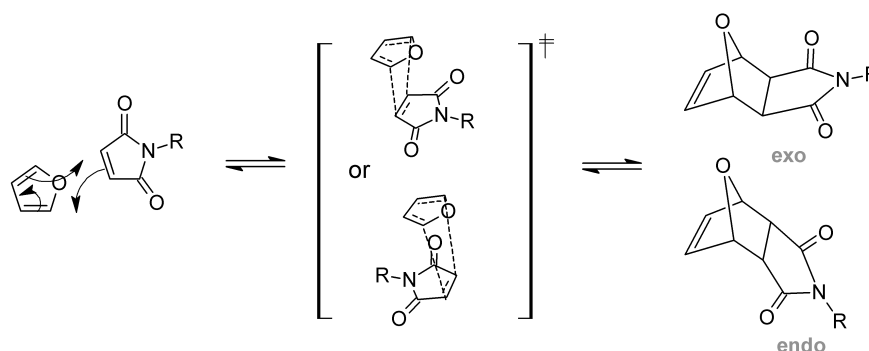
SCHEME 2: SCHEMATIC DA REACTION BETWEEN A DIENE AND A DIENOPHILE. THERE ARE TO POSSIBLE SIX-CENTERED TRANSITION STATES, RESULTING IN THE KINETICALLY FAVORED *ENDO*-PRODUCT AND THE THERMODYNAMICALLY FAVORED *EXO*-PRODUCT.

DA reactions occur between a conjugated diene and an alkene called the dienophile, in the example above butadiene and a maleimide. Cyclic dienes like furan or cyclopentadiene (CP) are exceptionally good DA reagents because the conjugated diene in cyclic systems are trapped in *cis*-position. Butadiene normally prefers the *trans*-conformation, making it necessary to rotate around the σ-bond. Because the involved orbitals are normally the HOMO of the diene and the LUMO of the dienophile, it is preferable to approach the energy level of these two orbitals. This can happen by electron-donating functional groups at 1-position of the diene. The HOMO of furan is higher in energy than that of CP because of the extra electron density brought to the system by the oxygen. Normally, furan and maleimide are reacted together because the energies of the involved molecular orbitals are closest, permitting faster DA reaction at lower temperatures.
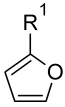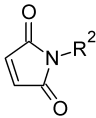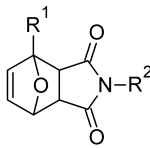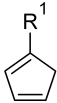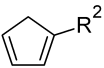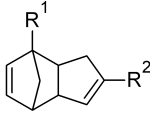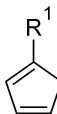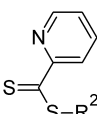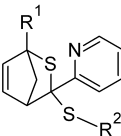
On the other hand, the dienophile reactant needs some kind of conjugation of the alkene for the DA reaction to occur. Simple alkenes have relatively high energy LUMOs and do not react well with nucleophiles. In the case of the maleimide ring, the π-system is extended onto two carbonyl-functional groups thereby withdrawing electron density from the double bond by –M effect.

DA cycloaddition reaction forms not only carbon–carbon bonds but also heteroatom–carbon bonds (HDA) and it is widely used synthetically to prepare six-membered

rings. [61] Dithioester are very reactive dienophiles when reacted with cyclic dienes. They react very fast, even at temperatures below room temperatures and in bulk, especially, when the reaction is catalyzed by a Lewis acid or trifluoroacetic acid. [62, 63] These catalysts coordinate to sulfur atoms of the dithioester end-group in order to increase the electrophilicity on the thiocarbonyl bond. [61] Table 1 summarizes the different reaction partners and reaction conditions for DA reactions used in preparation of thermally remendable polymers.

TABLE 1: SUMMARY OF DIFFERENT DA REACTION PARTNERS AND THE CORRESPONDING REACTION CONDITIONS.

Diene	Dienophile	Conditions	Adduct
Furan	Maleimide	DA: between RT and 120 °C RDA: >120°C Several hrs to days	
Cyclopentadiene	Cyclopentadiene	DA: between 80°C and 120°C[*] RDA: >120°C or >180°C[*] Several hrs to days (*) depending on R^1 and R^2	
Cyclopentadiene	Dithioester	HDA: between RT and 80 °C RHDA: >80 °C Minutes (Cat: Trifluoroacetic acid)	

The system using cyclopentadiene as both the diene and the alkene, demonstrate a distinctive feature that none of the other DA couples show. Wudl et al. showed that the cyclopentadiene dimer (dicyclopentadiene, DCP) is able to react as dienophile with a third CP molecule to form a trimer (Scheme 3). [64] In fact, even linear molecules with telomeric CP-units are able to form network-like materials.
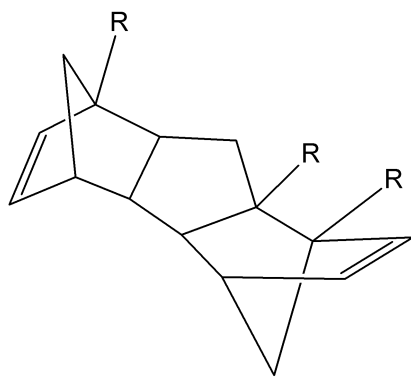
SCHEME 3: REPRESENTATION OF A CYCLOPENTADIENYL-TRIMER RESPONSIBLE FOR CROSS-LINKS IN CP-POLYMER. **[64]**

The reactivity of the functional groups in a polymeric material is strongly dependent on the mobility of these groups in the bulk of the polymer. In order to afford a DA-adduct, the reactants must be able to reach the six-centered transition state required to undergo the concerted cycloaddition. If the reactive units are trapped in a rigid matrix, not able to reach one-another, no DA reaction will be observed. This can be the case if too many cross-linking points are present or if the temperature is lower than the glass transition temperature of the linear polymer chains.

Polymers of CP have been known since Staudinger and Bruson. [65] They discovered not only that CP undergoes a self-DA reaction to produce DCP, but also that DCP is an even better DA substrate, and therefore continues to react with itself to produce a polymer. The major advantage of CP as DA-active units for polymer materials is the fact that CP acts as both the diene and the dienophile. [50] In 1961, Stille and Plummer investigated the polymerization of 1,6-bis(cyclopentadienyl)hexane, 1,9-bis(cyclopentadienyl)nonane and α,α'-bis(cyclopentadienyl)-*p*-xylenes in a homopolymerisation and in copolymerization with bismaleimides. [66]

CP derivatives of common chlorinated polymers have been widely synthesized and have been used as cross-linkers for the DA reaction. They are easily obtained by reacting the chlorinated polymers e.g PVC or polychloromethylstyrene (PCMS) with the sodium or lithium salts of CP. [67] The first to demonstrate the thermal reversibility of the DCP-system were Kennedy and Castner. [68] They thermally reversed *via* RDA at 215 °C, but because of the high temperatures these systems were not very stable.

Recently, Wudl et al. reported the synthesis of two DA-monomers starting from dicyclopentadiene, which was first transformed to dicylopentadiene dicarboxylic acid. Afterwards, the monomer was obtained by bislactonization with variable diols (Scheme 4). Mechanical and thermal properties of the resulting material can be tuned by varying the nature of the backbone of the diol. [64]
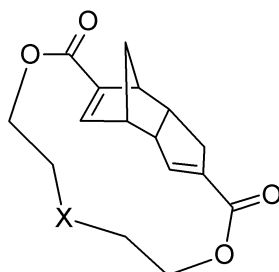
SCHEME 4: DICYCLOPENTADIENYL-MONOMER FOR SINGLE COMPONENT SELF-HEALING POLYMER [61]

By heating to the RDA reaction temperature of 120 °C, the monomer opens, releasing two CP-units, which can react intermolecularly to form a remendable polymer. The same authors could demonstrate, that these systems tent to form cross-linked networks when a DCP-unit acts like the dienophile in the DA reaction and reacts with a third CP. [64] Compression tests followed by healing showed remarkable shape recovery (Figure 5).

(a) (b)
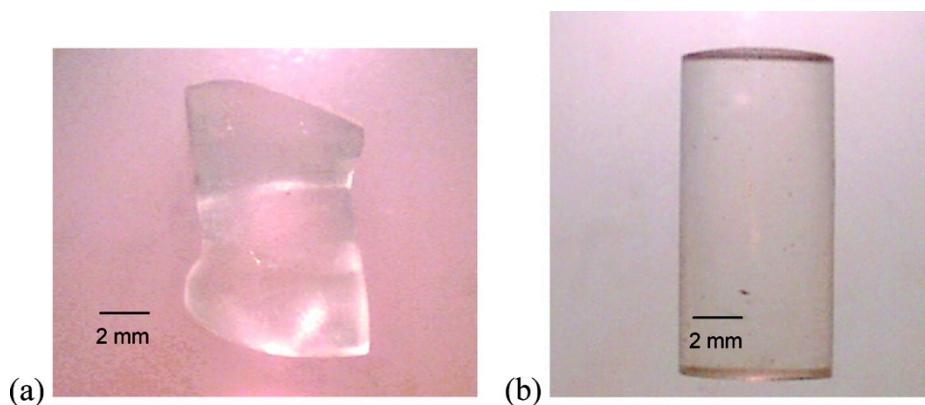
FIGURE 5: CPD-POLYMER (A) AFTER COMPRESSION TESTING AND (B) AFTER HEALING. REPRINTED WITH PERMISSION FROM [64]. COPYRIGHT (2008) AMERICAN CHEMICAL SOCIETY.

The first to use maleimide and furan moieties as cross-linking species for polymeric materials were Stevens and Jenkins. [69] They incorporated maleimide functional groups into a polystyrene backbone by Friedel-Crafts alkylation and envisioned the creation of a self-healing material using DA reactivity with a bifunctional furan linker. However this idea was not exploited until a decade later, when Stevens and

Canary mixed maleimide-modified polystyrene with difurfuryl adipate. [70] They achieved a remendable cross-linked material with a RDA temperature of 150 °C. Thermal instability of the furfuryl groups however limited healing cycles. Wudl et al. widely investigated maleimide and furan moieties to develop a remendable polymeric network. [48, 49, 71] The materials had comparable mechanical properties to those of commercially available epoxy resins, but a thermal treatment at a temperature above 120 °C allowed disconnecting 30 % of the cross-linking, which reconnected upon cooling. [48] Monomers were composed of divalent, trivalent or tetravalent maleimides and furans varying also in the nature of the spacer backbone. Diethylenglycol segments are used e.g. to lower the glass transition temperature of the resulting polymer, which increases mobility of polymer chains within the material. Both Wouters et al. and Singha et al. used furfuryl methacrylate as a co-monomer for co-polymerization with butyl methacrylate or methyl methacrylate, respectively. [72, 73] In the first example, free radical polymerization was used to synthesize the polymethacrylate backbone baring pendant furan-groups. [72] This leads to a polymer gel because under these reaction conditions, some of the furfuryl-groups cross-link. By mixing the swollen polymer with a bismaleimide as cross-linking-agent a powder coating system was obtained. The powder is applied onto a substrate and molten at elevated temperatures above 120 °C to form a coating which solidifies upon cooling. Subsequent heating and cooling cycles revealed reversible behavior and no significant loss of properties. [72] On the other hand, Singha et al. used atom transfer radical polymerization (ATRP) to prepare furfuryl methacrylate co-polymers together with methyl methacrylate. Thereby they achieved a better polydispersity index of 1.3 [73] and no cross-linking of the pendant furfuryl-groups was observed. The resulting linear co-polymer was cross-linked *via* DA reaction using bismaleimides.

Within the wide variety of dienes and dienophiles usable for self-healing based on DA chemistry, there are very few couples that allow fast cross-linking or polymerization. Reaction times of several days can be necessary for the DA reaction in the bulk of a polymer. Probably the fastest DA reaction reported until now, is the HDA reaction between CP and pyridinyldithioformate linkers. [62, 63] The monomers could be cross-linked in the solid state within minutes at room temperature and de-cross-linked at temperatures above 80 °C within minutes. Disadvantages for the application of these fast-healing systems are the small window of temperatures, relatively high costs and instability at higher temperatures limiting the number of healing-cycles. [63]

1.3.8 NO-C-Bonds

Self-healing polymeric materials, using dynamic covalent bonds like the NO-C-bonds as healing mechanism, are based on the same principles as stable free radical polymerization (SFRP) first mentioned by Kazmaier et al. [74] SFRP is a living polymerization technique using reversible termination of radical chain growth. Reversible terminators, such as 2,2,6,6-tetramethyl-1-piperidinyloxy (TEMPO), must have an endothermic enthalpy of reaction with styrene monomer so that they are not able to initiate new chains once they are liberated.

During SFRP, TEMPO is required to capture reversibly any radical at chain ends to prevent preliminary chain termination. To use this procedure as a self-healing mechanism the NO-C-bonds have to be used as cross-linking points in the thermosetting material. Therefore it is necessary to attach on one hand pendant styryl-groups captured by TEMPO on the backbone of any polymer. On the other hand, attachment of TEMPO-units to the polymer, which are linked to a styryl-moiety, provides the counterpart for cross-linking reaction. [75-77] By heating above 60 °C, free radicals are released, TEMPO and styryl-radical, which can recombine through radical exchange reaction, thereby cross-linking the material (Scheme 5). The biggest advantage is the rate at which the bonds dissociate and reform, leaving the material with all its mechanical properties even above the dissociation temperature.
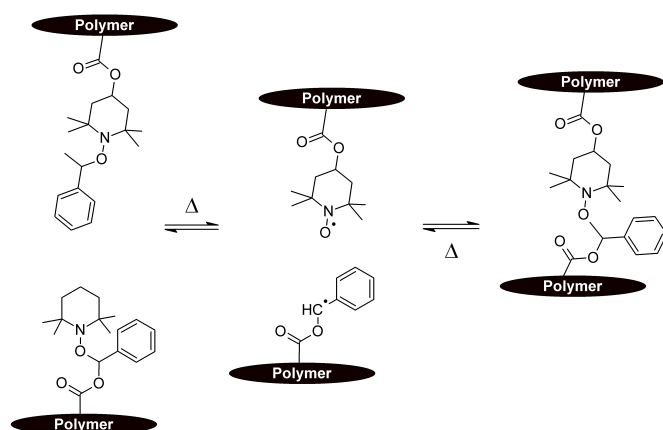
SCHEME 5: SCHEMATIC REPRESENTATION OF THE THERMODYNAMIC FORMATION OF
CROSS-LINKED POLYMERS VIA RADICAL EXCHANGE REACTION OF ALKOXYAMINES.

Stable organic radicals have received much attention over the last years. The
advantages of these systems are that the C-ON-bonds of alkoxyamines quite easily
breaks and reforms (Scheme 6). The resulting N-O-radicals are stable enough to give
the material the apparent dynamic features of a supramolecular system and the
mechanical strength of a covalently bonded polymer. [50] For the first time, Otsuka et
al. demonstrated the dynamic covalent bond between a TEMPO and a styryl-radical.
[75, 78, 79]
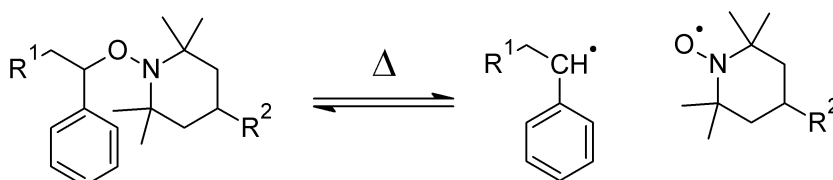
SCHEME 6: DISSOCIATION/ASSOCIATION OF ALKOXYAMINE-DERIVATIVES.

Model compounds were used to demonstrate the exchange reaction after breaking the
bond. [75] Otsuka et al. prepared linear polymers containing dynamic bonds in their
backbone [79] or as pendant groups on a PMMA chain. [75] Zhang et al. developed a
synthetic pathway to attach the dynamic unit on a PCMS polymer. [76] Both Zhang
and Otsuka demonstrated the gelation of these systems by radical exchange reaction
(Figure 6). By heating up the polymer, the covalent bonds break up in two radicals,
which can recombine with a different radical to form chemical cross-links. These
cross-links can easily be cleaved by adding an excess amount of free alkoxyamine.
[75]
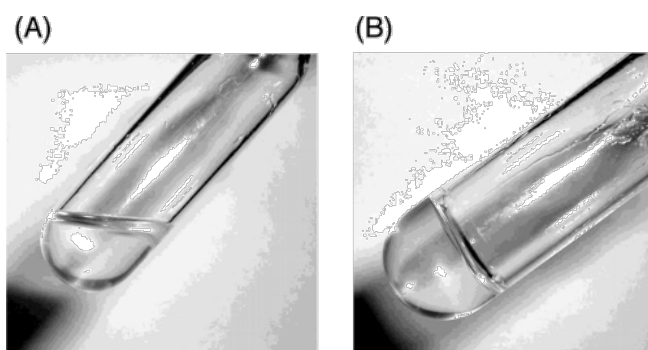
FIGURE 6: PICTURES OF THE SOLUTION OF THE POLYMER IN ANISOLE (10 WT%) (A) BEFORE AND (B) AFTER HEATING AT 100 °C FOR 24 H. REPRINTED WITH PERMISSION FROM [75]. COPYRIGHT (2006) AMERICAN CHEMICAL SOCIETY.

1.3.9 Alternative Mechanism

Thermal decomposition of perfluorocyclobutanes (PFCB) is an effectively irreversible reaction yielding different products. [80] On the other hand, pure mechanical decomposition, like in the case of ultrasonic pulses lead to breaking of the cyclobutane into two vinylethers. These can be thermally triggered to form PFCB-bonds once again. This healing mechanism is technically no thermoreversible mechanism and therefore it is treated apart.

1.3.10 Perfluorocyclobutanes

The C-F-bond in fluoroalkenes are with 460-540 kJ/mol very strong bonds. But vicinal fluorination has been shown to weaken the strength of the alkene. Tetrafluoroethene has a π-dissociation energy of only 220 kJ/mol. The double bond instability is responsible for the well-known propensity of fluorinated alkenes to undergo [2+2]-cycloaddition. Thermal [2+2]-cyloaddition is normally forbidden, because of molecular-orbital symmetry. In simple alkenes a biradical intermediate product has to be induced photochemically which recombines into a cyclobutane. [81] The weakness of the π-bond in fluorinated alkenes enables thermal dissociation into a biradical transition state.

Craig et al. investigated the self-healing properties of poly(perfluorocyclobutane) (PPFCB), an important class of polymers for aerospace and electronics. [80] PFCB-units were interesting because they break under mechanical stress to form trifluorovinylethers (TFVE), which is the starting material for the formation of

PPFCB. A simple thermal treatment (>150 °C) leads to re-mending (Scheme 7). The breaking mechanism involves a diradical transition state, which enables secondary self-healing mechanisms. The 1,4-diradical makes stress-induced cross-linking a possible self-healing mechanism and stress-induced isomerization, from *cis* to *trans*, could be the cause for stress-release like in the case of *gem*-dibromocyclopropane. [82]
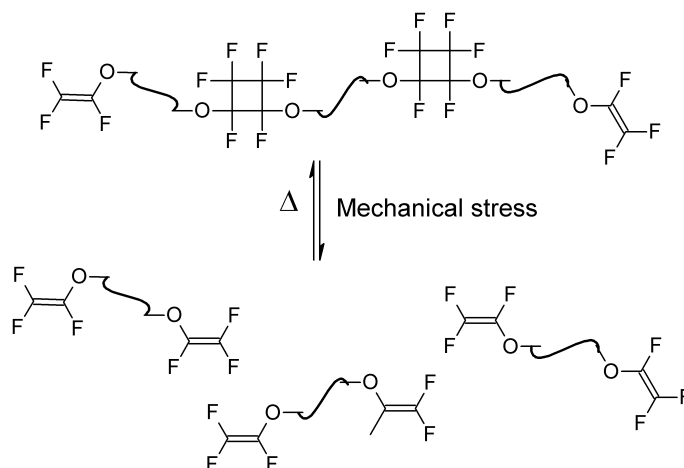
SCHEME 7: PFCB POLYMERS ARE CLEAVED BY MECHANICAL CHAIN STRESS INTO SMALLER PARTS CONTAINING TFVE GROUPS THAT CAN BE REPOLYMERIZED THERMALLY.

It must be distinguished between a thermal decomposition and a mechanical decomposition, because they do not yield the same product. [80] The major thermal decomposition products are hexafluorocyclobutene and phenol, an effectively irreversible reaction that is not suitable for remending. Only pure mechanical decomposition results in a cycloreversion of PFCB-moieties to thermally remendable TFVE-units. Ultrasonic pulses simulated these pure mechanical reaction conditions.

1.4 Inorganic-Organic Systems

In inorganic-organic composite and nanocomposite materials, properties of different material classes can be combined, to increase thermal stability, mechanical strength, electrical conductivity and/or the index of refraction. Inorganic particles or fibers have been widely used in the field of (nano)composites. These principles can be expanded onto self-healing composites and (nano)composites.

In particle or fiber-reinforced materials, the adhesion of the filler to the polymer matrix is important to guarantee load transfer from the polymer matrix to the reinforcement material. [83] Normally surface modification of the filler particles with polymerizable groups, allows chemical binding between both phases.

Peterson and coworkers attached dienophile maleimido functional groups to the surface of glass fibers. These glass fibers were combined with a thermosetting furan-functionalized epoxy resin. [83] Reversible DA reaction was used to impart reversible covalent binding at the polymer-glass interface. Mechanical stress was followed by complete failure of the interface. Significant healing could be observed after thermal treatment of 1 h at 90 °C.

Kwok and Hahn proposed to use carbon fibers as a resistive heating network for the use in self-healing composites based on the DA mechanism. [84] An electrical current passing through fibers of a carbon fiber filled polymer matrix causes heat dissipation through resistance heating. The heat created in the composite is then transferred to the insulating resin utilizing DA reaction to heal itself. Removal of any resin rich top layer may be necessary to expose the fibers and reduce local contact resistance as much as possible. [84]

Bowman et al. were interested in using the magnetic properties of metal-oxide nanoparticles to trigger self-healing by external alternating magnetic field. Therefore chromium oxide CrO_2, which has an ideal Currie temperature for RDA reaction (113 °C), was mixed with a trifuran monomer. To this mixture a diphenylbismaleimide was added and upon melting at 150 °C and re-cooling the monomers combined to a thermoreversible network. The black thermoset melted within a magnetic field and cross-linked again upon slow cooling. The maximum temperature depends on the weight-percentage of CrO_2 and the magnetic field strength. [85] The incorporation of magnetically susceptible particles in a thermoreversible gel results in a material that undergoes a reversible gel-to-sol transition when placed in an alternating magnetic field. The gel-to-sol transition allows the material to flow, and upon cooling macroscopic fractures are healed by diffusion.

1.5   Efficiency, Assessment of healing performance

In this subsection, popular methods for the control of healing performance will be mentioned. First of all, there are general analytical methods, like nuclear magnetic resonance (NMR) and infrared (IR) spectroscopy, differential scanning calorimetry (DSC), size-exclusion chromatography (SEC) or mechanical tests. On the other hand, some specialized tools are used depending on the system and the self-healing mechanism.

Besides liquid NMR and IR spectroscopy, solid-state ^{13}C NMR spectroscopy is another general method to study self-healing polymers. [48, 49] NMR allows to investigate the thermally reversible DA reaction in the macromolecular solid by differentiating e.g. between free furan groups and the pericyclic DA product.

In the case of PFCB as healing mechanism, ^{19}F NMR is a useful tool to distinguish between the PFCB unit and free fluoroalkenes. [80] SEC is especially useful in the analysis of soluble uncross-linked macromolecules. [62, 63, 80] If a thermoreversible reaction like DA or HDA or the thermal cyclisation of fluoroalkens is used to polymerize beginning from monomers, SEC can be used to monitor reversibility by checking for de-polymerization, by RDA reaction or mechanical damage.

DSC was also used to monitor DA and RDA reaction in self-healing polymers. [48, 49, 86] Wudl and coworkers used a specialized DSC technique called temperature modulated DSC. Using this method they could differentiate between reversible and non-reversible effects. Non-reversible effects, like degradation of the material tend to overlap with signals of the reaction of interest.

Dynamic mechanical analysis (DMA) has been proven helpful for self-healing performance assessment. [64, 77] It is applicable for all types of thermally self-healing materials, physical methods or chemical methods. In the case of dynamic covalent bonds, Yuan et al. used DMA to compare the temperature dependency of loss factor tan ∂ of reversibly cross-linked polystyrene and permanently cross-linked polystyrene. Both systems show similar glass transition temperatures signal at 125 °C. The dynamic equilibrium of dissociation/association is very fast and the apparent molecular weight does not change, allowing the part to retain the shape and mechanical properties even during healing process. [77]

Mechanical testing is very important to study the bulk properties of a healed material, which should be as similar as possible compared to the original materials properties.

Table 2 summarizes healing efficiencies of some materials using different mechanical tests. A general method to assess these properties is the three-point bending flexural test. [85] Three-point bending was used in the nanocomposite using CrO_2 as magnetic susceptible particles transferring the energy of an alternating magnetic field into the polymer matrix in the form of heat. The flextural test was used to determine the flextural strength of a specimen before and after several healing cycles. In these experiments, complete recovery of the flexural modulus and ultimate strength was demonstrated.

TABLE 2: SUMMARY OF HEALING EFFICIENCIES OF SELF-HEALING MATERIALS DETERMINED WITH DIFFERENT MECHANICAL TESTS.

Healing mechanism	Mechanical test	Healing conditions	Maximum healing efficiency
Cyclopentadiene Diels-Alder [64]	Three-point bending test	120 °C, 12 h	≈ 60 %
Maleimide/Furan Diels-Alder with CrO_2 [85]	Three-point bending test	110 °C , 12 h	≈ 100 %
C-ON bond [77]	Double cleavage drilled compression test	130 °C, 2.5 h	≈ 75 %
Maleimide/Furan Diels-Alder epoxy resin [86]	Double cleavage drilled compression test	120 °C, 20 min 80 °C , 72 h	≈ 96 %
Maleimide/Furan Diels-Alder [48]	Compact tension test	120 - 150 °C, 24 h	≈ 57 %
Interpenetrating Network (IPN) [46]	Compact tension test	130 °C, 1h	≈ 70 %
Interpenetrating Network (IPN) [45]	Compact tension test (modified)	165 °C, 1h	≈ 52 %
Maleimide/Furan Diels-Alder coatings [72]	Rheology, measurement of viscosity during heating cycles	175 °C , 1h	≈ 100 %

Fracture toughness is an indication of the amount of stress required to propagate a preexisting flaw. It is a very important material property since the occurrence of flaws is not completely avoidable in the processing, fabrication, or service of a material/component. There are different popular fracture test specimen geometries. Double Cleavage Drilled Compression (DCDC) specimens are particularly suitable for brittle materials (Figure 7A). [87] Janssen originally designed DCDC fracture tests

for measuring the fracture toughness of glass. [88] DCDC sample refers to a rectangular column with a circular hole drilled through its center that is subjected to axial compression. [87] This geometry was used by Zhang and coworkers to evaluate the healing efficiency of their maleimide and furan modified epoxy resin. The design allows for controlled incremental crack growth so that the cracked specimen remains in one piece after the test, ensuring realignment of the fracture surfaces prior to healing. A blade was wedged into the central hole of the DCDC specimen before to the test to create pre-cracks at the upper and lower extremities. [86] The same method was used in the case of the radical mechanism using alkoxyamines for self-healing. Healing efficiency was calculated from the ratio of critical stress required to propagate the crack to a given length in the healed material and in the virgin material. Nearly complete rehabilitation is observed for the cured resin, as characterized by the average healing efficiency of 96 %. [77]

Wudl et al. used a different geometry to test the fracture toughness of their DA self-healing materials. [48, 49] Hayes et al. investigated with the same test the properties of an IPN. [46] They chose compact tension test specimen geometry (Figure 7B). Gently tapping a fresh razor blade into a machined starter notch of the sample created a sharp pre-crack.
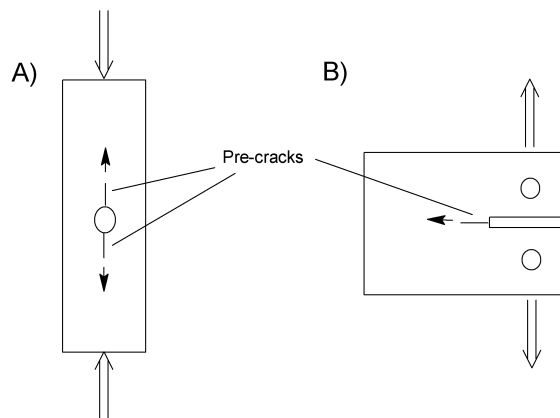
FIGURE 7: FRACTURE TEST SAMPLE GEOMETRIES (A) DOUBLE CLEAVAGE DRILLED COMPRESSION (DCDC) TEST (B) COMPACT TENSION TEST. PRE-CRACKS ARE FORMED BY TAPPING WITH A RAZOR BLADE.

Application of a tension perpendicular to the pre-crack, led to a complete fracture of the specimen by crack propagation. After structural failure, the two pieces were matched and held together with a clamp, treated at 120 to 150 °C under nitrogen for about 2 hrs, and cooled to room temperature (Figure 8). Fracture tests before and after

healing showed recovery of about 57 % of fracture strength. [48] Palmese et al. used the same geometry for the assessment of healing properties of their IPN, with the addition of a crack-arresting hole drilled in the middle of the crack-propagation pathway. [45]
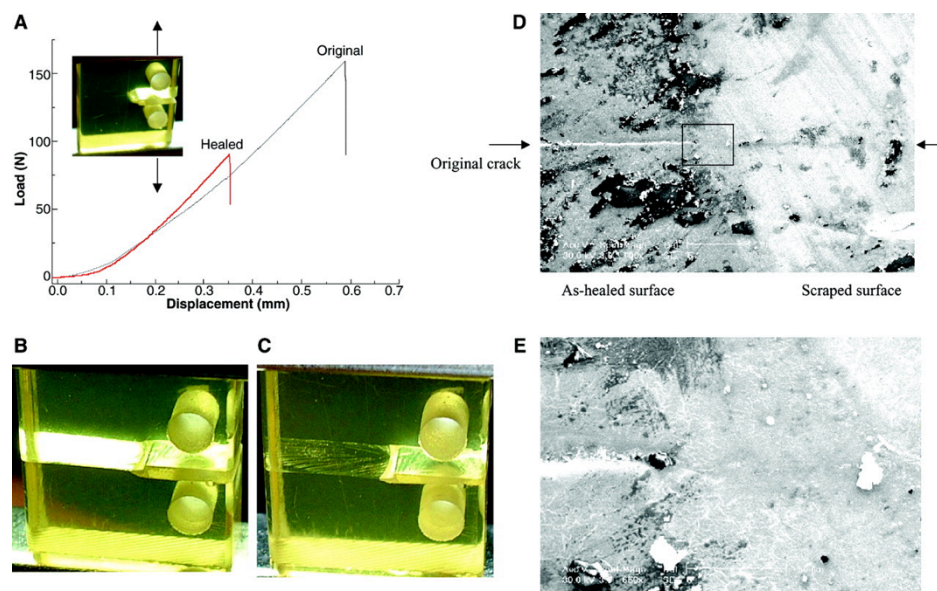
FIGURE 8: (A) MENDING EFFICIENCY OBTAINED BY FRACTURE TOUGHNESS TESTING. VALUES FOR THE ORIGINAL AND HEALED FRACTURE TOUGHNESS AT THE CRITICAL LOAD. (B) IMAGE OF A BROKEN SPECIMEN BEFORE THERMAL TREATMENT. (C) IMAGE OF THE SPECIMEN AFTER THERMAL TREATMENT. (D) SEM IMAGE OF THE SURFACE OF A HEALED SAMPLE: THE LEFT SIDE IS THE AS-HEALED SURFACE AND THE RIGHT SIDE IS THE SCRAPED SURFACE. (E) ENLARGED IMAGE OF THE BOXED AREA IN (D). REPRINTED WITH PERMISSION FROM[48]. COPYRIGHT (2002) SCIENCE MAGAZINE.

The free stable radical approach developed by Otsuka and Takahara allows a special analytical tool, which detects free radicals. [75, 78, 79] Electron Spin Resonance (ESR) spectroscopy was first used by Rong et al. and later by Zhang et al. to examine fission behavior of alkoxyamine moieties at increasing temperatures. [76, 77] Starting from a temperature of 100 °C, free radical concentration increased gradually. Cyclic ESR measurement between 20 and 130 °C showed that the relative intensity of the radical signal fluctuates and that the process is fully reversible apart from irreversible recombinations of styrene radicals. [77]

1.6   Silsesquioxanes and Spherosilicates

1.6.1   Nomenclature

Silsesquioxanes have the general formula $[RSiO_{1.5}]_x$, where R can by either hydrogen or an organic rest. Polymeric silsesquioxanes often demonstrate a ladder-like structure, which can be easily prepared by acid or base catalyzed hydrolysis of silane precursors (Scheme 8).[89-91]
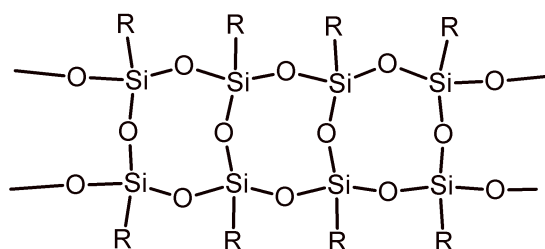
SCHEME 8: LADDER-LIKE POLYMERIC SILSESQUIOXANE

A more interesting class of materials are polyhedral oligomeric silsesquioxanes (POSS), the smallest siloxane structures known. The smallest known POSS is the T_8 silsesquioxane, which has a cubic structure and presents eight functionalities at the corners (Scheme 9). Higher homologues are the polyhedral T_{10}, T_{12}, and so on.

The T nomenclature originates from the three oxygen atoms bonded to each silicon atom. The subscribed number expresses the number x of repeating units in the formula $[RSiO_{1.5}]_x$.
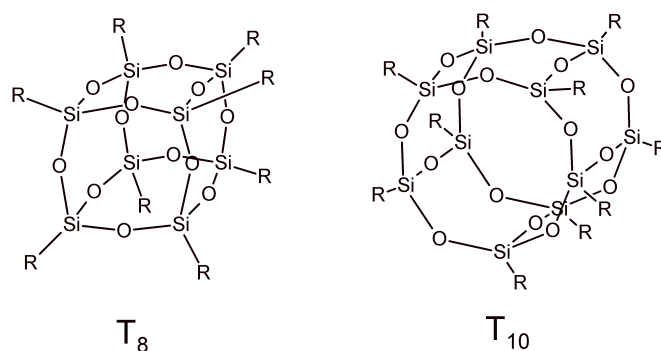
SCHEME 9: STRUCTURES OF T_8 AND T_{10} SILSESQUIOXANES.

A special class of silsesquioxanes is composed of silicon atoms with four neighboring oxygen atoms, referred to as spherosilicates. They have the general molecular formula $[ROSiO_{1,5}]_x$ and are designated with the letter Q. The most commonly used spherosilicate is the polyanion Q_8 (Scheme 10).

Q_8
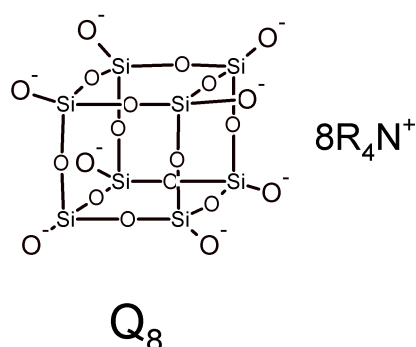
SCHEME 10: SPHEROSILICATE ALSO REFERED TO AS POLYANION Q_8

1.6.2 Synthesis and applications of cubic T_8 and Q_8 derivatives

Preparation of T_8 cubes from trialkoxysilanes requires catalysis because the relatively slow condensation reaction leads to a broad variety of products, from polyhedral to linear or branched macromolecular structures.[92] Typically, yields of 30 % are not exceeded. In some cases the use of a superacid may increase the yield and decrease the number of products. Kaneko et al. used trifluoromethanesulfonic acid for the preparation of T_8 structured (3-aminopropyl)silsesquioxane.[93] On the other hand highly reactive trichlorsilanes were also used for the preparation of POSS.[94] The fast condensation in the presence of water minimizes secondary reactions and relatively high yields of the cubic structures are obtained.

Hydridosilsesquioxane $H_8Si_8O_{12}$ has shown to be useful for the preparation of various functional T_8 materials. Agaskar et al. developed a simple method for the preparation of $H_8Si_8O_{12}$ by hydrolysis of trichlorsilane $HSiCl_3$ using Fe^{3+} as catalyst.[95] Subsequent hydrosilation can be applied to introduce many desired organic rests. The introduction of one or more polymerizable groups was employed to incorporate the inorganic cages in nanostructured hybrid materials by copolymerization.[94, 96] Lin et al. were the first to use POSS as building blocks for DA based self-healing nanocomposites. Therefore, they reacted furfurylamine with commercially available glycidyl POSS to create a octafunctional dienic silsesquioxane.[97]

Spherosilicates with the cubic structure Q_8 are mainly interesting because they are easily prepared in high yield. They can be prepared either by a bottom-up or a top-down technique using tetraalkylammonium hydroxides. Q_8 spherosilicate was first reported by Hoebbel et al. in 1971, when they treated silicic acid with

tetramethylammonium hydroxide.[98] Laine et al. investigated the top-down approach using various R_4NOH species to dissolve rice hull ash, a waste product of the rice industry previously considered as useless.[99] The most commonly used precursors for spherosilicates are tetraalkoxysilanes, which can be hydrolyzed in methanol using tetramethylammonium hydroxide (Scheme 11).[100, 101]
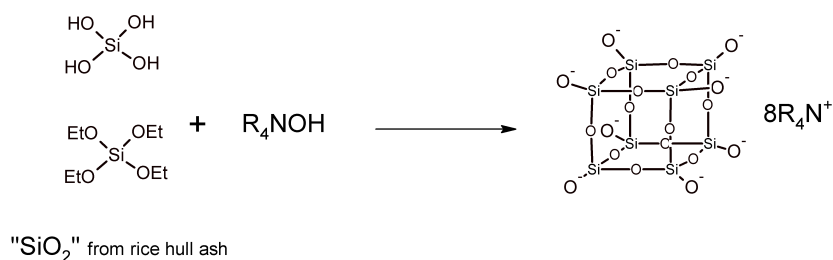
SCHEME 11: SYNTHESIS OF Q_8 POLYANION FROM VARIOUS PRECURSORS.

The bulky counter ion R_4N^+ prevents the formation of polymeric products, directing the formation of only the cubic polyanion. The resulting spherosilicate solution can be functionalized in a biphasic reaction with chlorosilanes leading to the desired functionalities.

End capping with dimethylchlorosilane yields the $Q_8M_8^H$ species (Scheme 12), which can be used for further modification of the corners via hydrosilation reaction, in a similar way to $H_8Si_8O_{12}$.
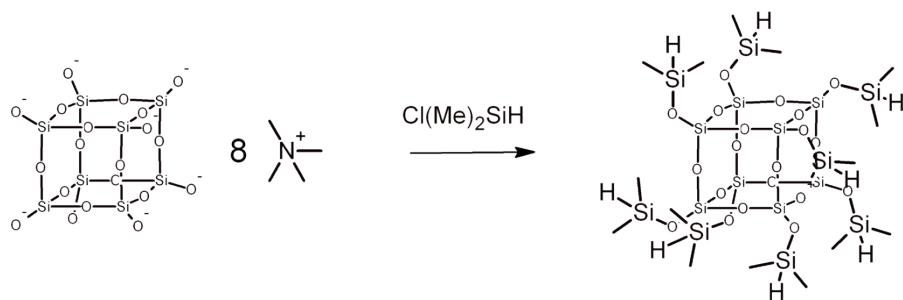
SCHEME 12: END CAPPING OF OCTAANION WITH DIMETHYLCHLOROSILANE TO FORM $Q_8M_8^H$ SPECIES.

The introduction of polymerizable groups, such as acrylates or methacrylates and the copolymerization with standard monomers results in cross-linked hybrid materials.[96] Kickelbick et al. as well as Laine et al. managed to modify the $Q_8M_8^H$ cage with initiator groups and photoinitiator groups for surface-initiated polymerization.[102-104] Grafting-from ATRP or photopolymerization yielded star-shaped polymers with inorganic cage-like cores.

2   RESEARCH GOALS

The aim of this work is to investigate synthetic routes to employ silica based nano-building blocks as the counterpart for reversibly cross-linkable polymer matrices. In recent years substantial progress was observed in the field of thermally remendable polymers using DA chemistry as the self-healing mechanism. Both simple polymeric materials and composite materials were investigated. Composite approaches focused primarily on the use of nanoparticles as means of triggering the self-healing by taking advantage of their physical properties. Magnetic nanoparticles were introduced into self-healing polymeric matrices to exploit hyperthermia resulting from the exposure to an alternating magnetic field. Nevertheless, there is still a need to investigate the role that inorganic nano-building blocks could play as cross-linking agents within DA based self-healing nanocomposites.

Different methods for surface modification of silica nanoparticles with maleimide or furan functionalities are applied in order to identify universal and practical techniques to accomplish the goal of self-healing nanocomposites.

Synthesis of SiO$_2$ nanoparticles

Silica nanoparticles are chosen as an ideal starting point, because of their uniform size and shape and their well-established surface chemistry. They can be easily prepared by a sol-gel method. The main focus will remain on the design of the surface functionalities and their chemical properties towards the reversible DA reaction within a polymer/particle mixture. In opposition to homogenous systems, functional nanoparticles and their surface chemistry are controlled by additional constrictions.

DA reaction on sterically crowded surfaces

Molecular trialkoxysilanes are first examined as surface functionalities. Various commercially available alkoxysilanes can serve as starting material to prepare maleimde functionalized coupling agents. Their synthesis and attachment to the silica surface are investigated. Elemental analysis, TGA and FTIR spectroscopy will be used to confirm modification of the nanoparticles and will provide a way to quantify the surface coverage. The use of IBMK as an alternative solvent for the modification

step should facilitate functionalization and decrease agglomeration of the nanoparticles. DLS allows examining the quality of the nanoparticle dispersions obtained.

Model reactions are performed to compare the reactivity of free soluble maleimides and furans with the reactivity of surface attached reaction partners. UV-Vis spectroscopy allows following maleimide consumption during DA reaction. Due to the low organic content of the surface modified nanoparticles and their light scattering properties, combinations of analyzing techniques are employed to quantify DA conversion and conclude on the suitability of the modified silica nanoparticles for the creation self-healing nanocomposites.

Core-shell nanoparticles by grafting-from polymerization

Surface-initiated grafting-from polymerization is chosen as supplementary surface modification technique. This method provides the possibilities to increase the number of functional groups as well as the distance between the surface of the nanoparticle and the functional groups. The choice of comonomers offers the potential to adapt and tune the properties of the interface between inorganic particle and polymeric matrix. Glass transition temperature and polarity are the essential variables on the way to an effective self-healing nanocomposite. Methacrylic monomers are available with various alkyl chain lengths and are easily modified to incorporate dienic and dienophilic functionalities. As counterpart for the inorganic functional building blocks, a linear thermoplastic polymer matrix is synthesized from maleimide or furan bearing monomers and non-functional comonomers using ATRP. By mixing both the linear polymer and the core-shell particles a hybrid material is formed. DA reactivity, mechanical and thermal properties, as well as self-healing abilities are investigated with different techniques.

Spherosilicates as building blocks for self-healing materials

Additionally to Stöber particles, molecular nanosilica, known as spherosilicates are considered as cross-linking agents for DA self-healing composites. They serve as model system to study reactivity. Their solubility facilitates homogenous distribution within the functional polymeric matrix and the diffusion of the inorganic cross-linking agents towards crack interfaces. Functionalization with furan moieties is facilitated by the aromaticity of the diene, limiting side reactions during hydrosilation. DA

reactivity, mechanical properties and self-healing performance will be investigated using different maleimide cross-linkers.

Comparative study of inorganic building blocks

Finally, a comparative study is carried out to show which inorganic building block is most suitable to prepare a self-healing hybrid material. Therefore the kinetics of the DA reaction, the reversibility of the cross-linking, the mechanical properties of the cured materials and the self-healing capacities are investigated.

3   RESULTS AND DISCUSSION

The results of this work have been published.

3.1   Thermoreversible Reactions on Inorganic Nanoparticle Surfaces: Diels−Alder Reactions on Sterically Crowded Surfaces

The easiest way to use silica nanoparticles as reactive moieties for the synthesis of self-healing nanocomposites using the DA reaction as cross-linking mechanism is a direct modification of their surface with dienophilic or dienic functionalities.

The first publication describes the synthesis of silica nanoparticles with a diameter below 5 nm baring different coupling agents with incorporated maleimide groups. Trialkoxysilanes were used as anchoring group for the surface modification. They react with silanols on the surface to form stable Si-O-Si bonds. The kinetics of hydrolysis and condensation strongly depends on the type of alkoxy rest. Methoxy-groups are far more labile and react relatively fast compared to ethoxysilanes. In the case of maleimdo baring alkoxysilanes, synthetic strategies starting from trimethoxysilanes were not successful because they did not endure the harsh reaction conditions during the synthesis of the coupling agent. The use of triethoxysilanes on the other hand required increasing the reactivity by heating the reaction mixture during surface modification. In literature toluene is often used as a solvent with high boiling point. A great drawback is that the particle suspension, previously stabilized by electrostatic repulsion in alcoholic solution is not stable in toluene. As soon as toluene is added, the particles precipitate and eventually form a gel. The solution to this problem was the use of a solvent that has both a high boiling point and a relatively high dielectric constant. Isobuthyl methyl ketone (IBMK) has both of these characteristics. A solvent exchange procedure starting from the suspension in methanol was used to slowly transfer the nanoparticles into IBMK without previous isolation. Three different coupling agents baring maleimide functionalities were prepared starting from commercially available triethoxysilanes. N-((3-Triethoxysilyl)-propyl)maleimide (MPTES) was prepared from 3-aminopropyltriethoxysilane (APTES) and maleic anhydride. The second coupling agent was prepared from 2-

hydroxyethylmaleimide and N-(3-isocyanoatopropyl)triethoxysilane by a tin catalysed urethyl formation to form 2-(2,5-dioxo-2,5-dihydro-1**H**-pyrrol-1-yl)ethyl(3-(triethoxysilyl)propyl)carbamate (MUPTES). The third synthetic strategy employed the Michael addition between APTES and 1,1′-(methylendi-4,1-phenylene)bismaleimide. The amino group of APTES adds across the double bond of one of the dienophiles of the bismaleimide. All three coupling agents could be used to modify the surface of the previously prepared Stöber silica particles. The successful surface functionalization could be demonstrated by FTIR spectroscopy and TGA experiments. The nitrogen percentage determined by elemental analysis as well as the surface area of the nanoparticles from nitrogen adsorption/desorption measurements were used to calculate the surface coverage. The ability of the maleimide groups attached closely to the particle surface to undergo DA reaction was investigated by reacting a nanoparticle suspension in isopropanol with molecular furan. The results and comparison with model reaction of maleimide compounds not attached to a particle surface revealed that the reactivity is strongly inhibited and increases with decreasing surface coverage. Model reactions of maleimide compounds with comparable substitutions next to the maleimide ring showed that increasing the electron deficiency of the dienophile could increase the kinetics of the DA reaction. A phenyl group attached to the nitrogen atom of the maleimide ring draws electron density out of the conjugated π-system by mesomeric -M effect. An alkyl chain like the propyl in MPTES on the other hand, increases the electron density by inductive +I effect.

In conclusion, DA reaction on the surface of silica nanoparticles modified by short dienophilic coupling agents is possible but its conversion is strongly dependent on steric effects. DA reaction on sterically hindered silica surfaces is not the best choice for the creation of self-healing nanocomposites. The relatively low DA reactivity will drastically decrease within a polymeric matrix, where the kinetics are dominated by diffusion of polymer chains and the accessibility of the reactive surface groups will decrease as cross-linked macromolecules block the surface of the nanoparticles.

In order to achieve a higher reactivity, the distance of the reactive groups to the surface of the nanoparticles has to be greatly increased. Longer spacer groups between the anchoring triethoxysilane and the maleimide were envisioned by using the hydrosilation reaction, but all attempts were in vain because secondary hydrosilation took place at the double bond of the maleimide. Protection of the

maleimide by DA reaction with furan prior to the addition of the silane led also to secondary products and the presence of primary amine is not tolerated by the hydrosilation reaction.

The results have been published in *Chemistry of Materials*:

T. Engel, G. Kickelbick**,** Thermoreversible Reactions on Inorganic Nanoparticle Surfaces: Diels−Alder Reactions on Sterically Crowded Surfaces, *Chem. Mater.* **2013**, *25*, 149-157. © 2012 American Chemical Society.
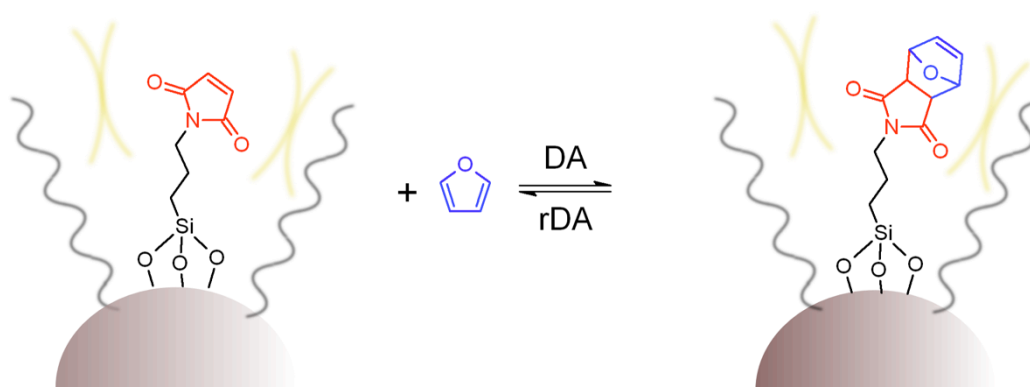

FIGURE 9: *TABLE OF CONTENT*: SCHEMATIC REPRESENTATION OF A STERICALLY CROWDED DA REACTION ON THE SURFACE OF SILICA NANOPARTICLES.
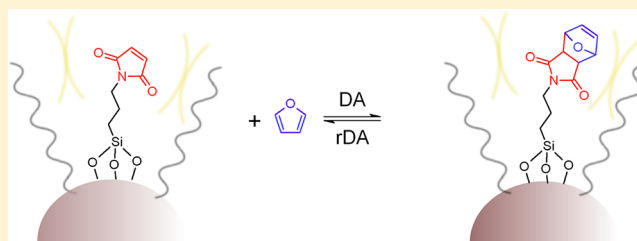
Thermoreversible Reactions on Inorganic Nanoparticle Surfaces: Diels−Alder Reactions on Sterically Crowded Surfaces

Tom Engel and Guido Kickelbick*

Inorganic Solid State Chemistry, Saarland University, Am Markt Zeile 3, 66125 Saarbrücken, Germany

S *Supporting Information*

ABSTRACT: Organically surface-functionalized nanoparticles are important cross-linkers for nanocomposites. In the past, many cross-linking reactions were based on simple radical additions. However, novel smart materials require reversible reactions. These reactions, such as the Diels−Alder reaction, often have a specific sterical demand, e.g., a six-centered transition state. In this study, < 5 nm silica particles were functionalized with maleimide groups, and their reactivity with regard to Diels−Alder reactions were investigated, applying various techniques. A new method for the surface modification of silica nanoparticles is presented, minimizing agglomeration in organic solvents and thus increasing the accessibility of the functional groups on the particle surface. Kinetic studies of substituted model compounds were carried out to evaluate the reactivity of the maleimide functionality. The Diels−Alder reaction between 2,5-dimethylfuran and *N*-propylmaleimide, *N*-ethyl(*N*-propylcarbamato)maleimide, and *N*-phenylmaleimide was followed by UV/Vis spectroscopy. The reaction rate increases in this order, showing the effect of maleimide substitution. Afterwards *N*-((3-triethoxysilyl)propyl)maleimide was used to graft maleimidopropyl functional groups onto the nanoparticle surface. 3-Aminopropyltriethoxysilane, which could then be reacted with 1,1′-(methylenedi-4,1-phenylene)bismaleimide, was used to attach phenyl-substituted maleimide functionality to the surface. 3-Isocyanatopropyltriethoxysilane introduced the electron-drawing carbamato functionality into the system. The surface coverage of the samples was characterized applying CHN analysis, TGA-FTIR coupling, and FTIR spectroscopy. All analytical methods revealed that the functional groups are covalently bonded to the silica surface and the maleimide rings remain intact. Diels−Alder reactions of the surface groups show that the reactivity of the molecules attached to the particles depends on sterical crowding, but the reaction rate is not significantly changed by surface effects.

KEYWORDS: *nanoparticles, surface-functionalization, thermoreversible reaction, Diels−Alder*

■ INTRODUCTION

Inorganic nanoparticles are important building blocks for many novel materials. The incorporation of nanoparticles in polymer matrixes can dramatically change their properties. Particularly the mechanical and thermal properties are influenced by the incorporated inorganic phase. In many cases it is necessary to provide a surface-functionalization to enhance the compatibility and the dispersion of the nanoparticles in an organic matrix.[1,2] Changing the polarity and the availability of functional groups has a significant effect on the dispersibility in the monomer or polymer matrix and allows a tight bonding to the latter by the formation of cross-linked networks. The grafting of polymerizable functional groups onto the nanoparticle surface allows covalent bonding with the matrix, improving the compatibility of the phases and preventing phase separation and agglomeration of particles.[2,3] Methacryloxy and epoxy functionalities have been used to incorporate silica nanoparticles into organic matrixes through copolymerization.[3] This increases homogeneity of the particle distribution and also mechanical strength of the resulting nanocomposite. A drawback of highly cross-linked materials is crack formation and crack propagation. In addition, the often observed absence of glass transition and melting

points prevents the cross-linked nanocomposite from being reprocessed and reshaped.

In recent years, compounds with reversible bonding became the focus of materials scientists, due to self-healing properties and the possibility to reprocess and reshape cross-linked nanocomposites.[4−8] One of the major mechanisms used in this respect is the Diels−Alder (DA) reaction, applying maleimide and furan functional groups as dienophiles and dienes. Due to the thermoreversible reaction type these materials show also a self-healing ability.

Wudl et al. were the first to synthesize a thermally remendable macromolecule and to investigate its self-healing properties.[4] They found that cuts or cracks could be healed by a simple thermal treatment. Our aim is the combination of reversible DA chemistry with the advantages of nanocomposite materials.

By using reversible DA cross-linking, the inorganic particles can be separated from the polymer matrix by a simple thermal

treatment. Beyer et al. used reversible DA chemistry to develop polymer films in which a change in optical clarity can be thermally triggered.[9] Rahman et al. grafted free maleimide functional groups through nucleophilic addition of a commercially available bismaleimide onto the surface of amino-functionalized silica nanoparticles.[10] They investigated the reactivity of the maleimide groups to undergo Michael reaction on the surface of the particles.

In the same spirit we investigated the surface functionalization of silica nanoparticles with maleimide functional groups. An important aspect of our work was the investigation of the reactivity of the dienophiles on the surface of nanoparticles. Because of the sterical hindrance and the demand of a six-membered transition state for the DA reaction, it is important to judge the effect of sterical crowded surfaces on this reaction type. Therefore, different coupling agents with maleimide functionality were synthesized and grafted onto particles, and the surface coverage was determined. A model reaction with furan was used to investigate the influence of steric hindrance on DA and retro-Diels−Alder (retro-DA) chemistry.

■ RESULTS AND DISCUSSION

Synthesis and Characterization of Silica Nanoparticles. Spherical amorphous silica nanoparticles were prepared following a modified Stöber process.[11] Tetraethyl orthosilicate (TEOS) was first hydrolyzed and then condensed in alcoholic solution, applying ammonia as base. Transmission electron microscopy (TEM) (Figures S1 and S2, Supporting Information) and dynamic light scattering (DLS) measurements of the obtained nanoparticles in methanol revealed a diameter of 3.8 ± 0.9 nm and 4.8 ± 0.8 nm, respectively. Nitrogen sorption measurements were performed to calculate the surface area of particles according to Brunauer, Emmett, and Teller (BET).[12] The nitrogen sorption measurement shows a specific surface area of 750 m^2 per gram of silica nanoparticles. When assuming a spherical shape of the particles and a density for silica of 2.2 g cm^{-3}, the calculated diameter is 3.6 nm, which corresponds to the diameter measured in the TEM experiment. Some discrepancy may be explained by porosity. The physisorption isotherm revealed a characteristic hysteresis loop, which is associated with capillary condensation taking place in mesopores (IUPAC Type IV H2).[13]

Surface functionalization was carried out by applying a solvent-exchange methodology, which allows for higher surface coverage and very low agglomeration of the particles.[14] Isobutyl methyl ketone (IBMK) was used as the suspension medium for the silica particles during the modification step because of its relatively high dielectric constant, $\varepsilon = 13.1$, which results in ionized hydroxyl groups on the nanoparticle surface. Another advantage of this solvent is the relatively high boiling point of 115 °C, which favors the elimination of ethoxy groups and condensation of the silane coupling agents during functionalization reactions.

In previous studies, toluene was the preferred solvent because of the high boiling point, but its low dielectric constant of $\varepsilon = 2.4$ made it a poor choice because the particle suspension is not stable in toluene and the particles tend to agglomerate. Green et al. isolated the bare silica particles and redispersed them in IBMK after drying.[14] In this work, it was examined if the solvent could be changed without isolation of the particles. Therefore, IBMK was added to a freshly prepared silica suspension in methanol, and the two solvents were codistilled by rotary evaporation. This step was repeated two times.

Dynamic light scattering measurements before and after the solvent exchange showed that the particle suspensions remained stable during this procedure (Figure 1).
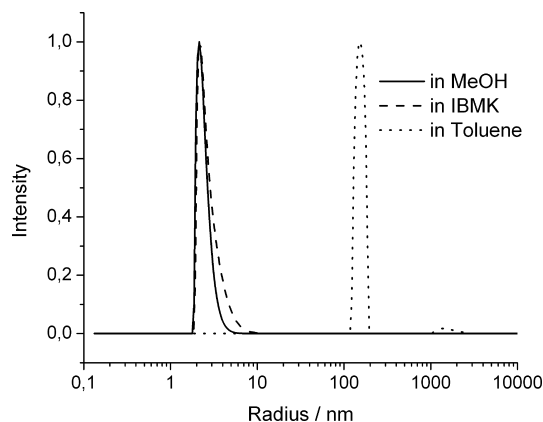
Figure 1. DLS size distribution of silica particles before and after solvent exchange and after suspension in toluene.

The particles in the original alcoholic dispersion had a diameter of 4.8 ± 0.8 nm. The particles transferred to IBMK showed a diameter of 5.4 ± 1.2 nm (DLS). In addition, Figure 1 shows the size distribution plot of the same silica particles if suspended in toluene. Agglomerates with a diameter of more than 300 nm were formed in toluene.

Coupling Agents. Different coupling agents for the surface modification of the nanoparticles were used. *N*-((3-Triethoxysilyl)propyl)maleimide **1**, 2-(2,5-dioxo-2,5-dihydro-1*H*-pyrrol-1-yl)ethyl(3-(triethoxysilyl)propyl)carbamate **2**, and 1-(4-{[4-(2,5-dioxo-3-{[3-(triethoxysilyl)-propyl]amino}-pyrrolidin-1-yl)phenyl]methyl}phenyl)-2,5-dihydro-1*H*-pyrrole-2,5-dione **3**. These molecules are composed of a triethoxysilane anchor group, a spacer, and a maleimide functional group used as the dienophile functionality for DA reaction.

1 was synthesized according to a literature procedure (Scheme 1)[15] with an overall yield of 96%.

Scheme 1. Reaction Scheme for the Preparation of 1^a
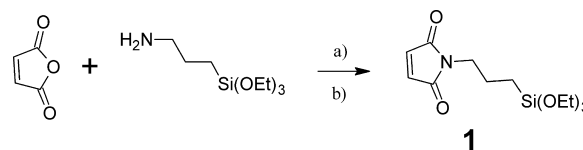
^{a}Reagents and conditions: (a) dry DCM, RT, 1 h; (b) ZnCl, HMDS, dry toluene, 80 °C, 5 h.

2 was prepared according to a modified literature procedure via a dibutyltin dilaurate-catalyzed addition of protected 2-hydroxyethylmaleimide with *N*-(3-isocyanoato-propyl)-triethoxysilane (Scheme 2).[16] The protection of maleimide functionality with furan via DA reaction is necessary because 2-hydroxyethylmaleimide tends to polymerize via Michael addition of the hydroxyl group to the maleimide double bond. Deprotection takes place during the surface modification step of the silica nanoparticles. The boiling point of the suspension medium IBMK is sufficiently high to provoke retro-DA reaction with liberation of furan.

Scheme 2. Reaction Scheme for the Preparation of 2[a]
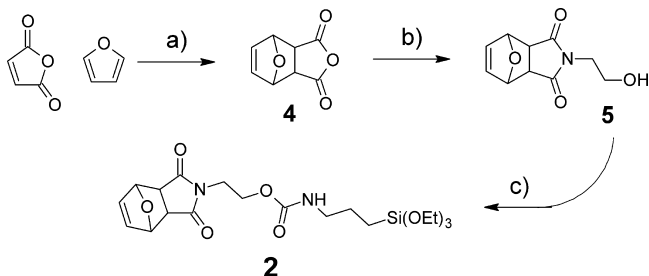
[a]Reagents and conditions: (a) Toluene, rt, 24 h; (b) ethanolamine, dry MeOH, reflux, 24 h; (c) isocyanatopropyltriethoxysilane, dibutyltin dilaurate, acetone, reflux, 12 h.

Commercially available APTES was used to react with 1,1'-(methylendi-4,1-phenylene)bismaleimide via Michael addition as shown in Scheme 3 to form **3**.

Surface Modification and Characterization. Dynamic Light Scattering. DLS was used to investigate the dispersibility of the isolated particles, which is an important proof of the availability of the functional groups at the surface. The particles were mixed with different solvents, and they were sonicated for 10 min. For **1@SiO$_2$** and **2@SiO$_2$**, the best results were achieved with 2-propanol as suspension medium (Figure 2). The other solvents resulted in agglomerates of more than 100 nm. Only suspension in 2-propanol resulted in a narrow distribution around 15 and 60 nm, respectively. This could be explained by the duality of the 2-propanol properties. On the one hand, it has a hydroxyl group, which can undergo hydrogen bonding with either the particle surface or the carbonyl groups of the maleimide ring, and on the other hand, it has an isopropyl chain, which can develop weak interactions with the surface functionalities. **3@SiO$_2$** was not dispersible in 2-propanol and most other suspension mediums. The best result, a relatively broad size distribution of 100 nm, was achieved in dimethylformamide (DMF). This study shows how critical the suspension medium is for the accessibility of the functional groups.

FTIR Analysis. The success of functionalization was studied by FTIR spectroscopy (Figure 3). All samples showed multiple peaks in the "fingerprint"-region of silica between 460 and 1200 cm^{-1}: A strong asymmetric Si−O−Si vibration at about 1100 cm^{-1}, weaker asymmetric Si−OH vibration at 957 cm^{-1}, symmetric Si−O−Si vibration at 797 cm^{-1}, and two additional peaks at 573 and 460 cm^{-1}.[17] The FTIR spectrum of pure silica shows the presence of molecular water through scissor bending vibration at ~1630 cm^{-1}. The broad signal between 3300 and 3700 cm^{-1} is a superimposition of H-bonded molecular water
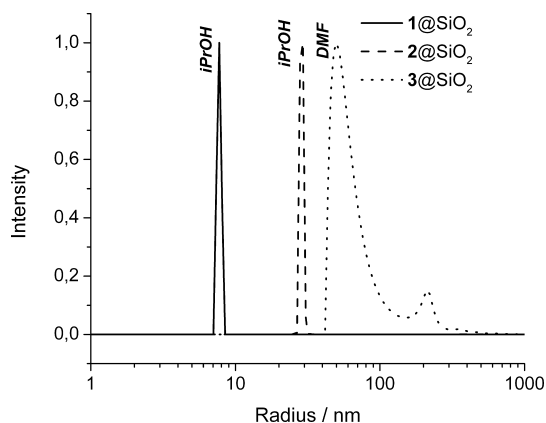
Figure 2. Dynamic light scattering size distributions of **1@SiO$_2$** in 2-propanol, **2@SiO$_2$** in 2-propanol, and **3@SiO$_2$** in DMF.
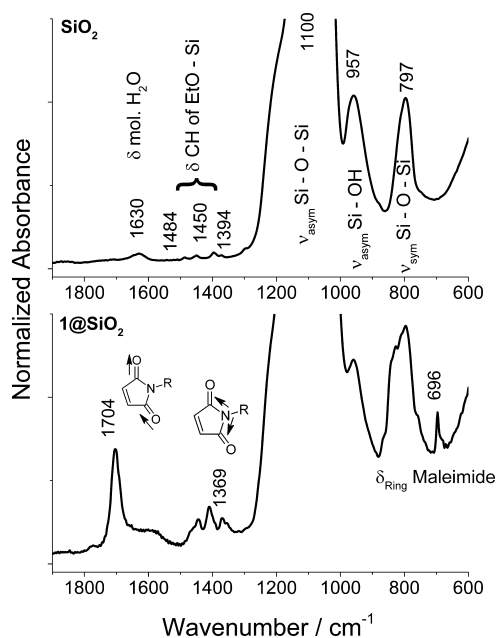
Figure 3. Infrared spectra of bare silica and the sample modified with **1**.

and hydroxyl terminals of silanol groups. An O−H stretching vibration, characteristic of free surface silanol groups, was only detected in the pure silica sample at 3746 cm^{-1}.[18] CH$_2$ and CH$_3$ (2907, 2945, and 2984 cm^{-1}) vibrational modes can be assigned to the remaining ethoxy groups on the surface of the

Scheme 3. Reaction Scheme for the Preparation of BMPTES
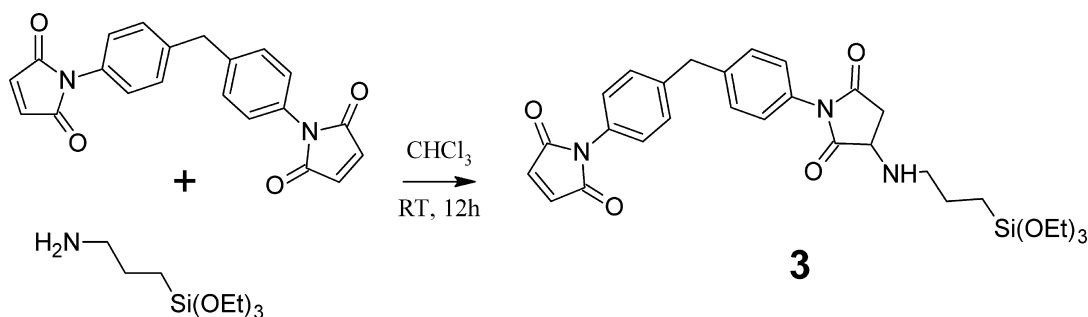
nanoparticles as well as the weak signals at 1484, 1450, and 1394 cm^{-1}, which rise from C−H bending modes..

Attenuated total reflection infrared (ATR-FTIR) measurements of the **1**-functionalized particles revealed characteristic signals for organic coupling agents (Figure 3). The strong asymmetric stretch of the carbonyls could be detected at 1704 cm^{-1}, and even the weak symmetric stretching mode is visible at 1770 cm^{-1}. The symmetric C−N−C stretching vibration at 1369 cm^{-1} is another proof of the successful functionalization with maleimide functionality. Another indication for the high surface modification is the peak at 696 cm^{-1} assigned to maleimide ring deformation.[19]

The FTIR spectrum of **3**@SiO$_2$ (Figure S4, Supporting Information) shows signals for both the symmetric and asymmetric stretching modes of the conjugated maleimide carbonyl groups at 1773 cm^{-1} (very weak) and 1714 cm^{-1} (strong). The last mentioned signal is stronger than all the other carbonyl signals because the surface molecules are composed of two imides. The signal at 1513 cm^{-1} could be assigned to aromatic C−C stretching mode of the benzene rings and the peak at 1388 cm^{-1} is caused by a symmetric C−N−C stretching vibration within the maleimide ring as shown by Parker et al.[19]

In the spectrum of **2**@SiO$_2$ (Figure S3, Supporting Information), both symmetric and asymmetric stretching modes of carbonyls at 1773 cm^{-1} and 1710 cm^{-1} were present but the signals are weaker because of lower surface coverage. Weak C−H bending modes could be observed at 1439 cm^{-1} and 1409 cm^{-1}. A signal at 1546 cm^{-1} could arise from maleimide C=C stretching or N−H bending of the urethyl group. The high amount of surface modification is also verified by the maleimide ring deformation at 697 cm^{-1}.

Thermogravimetric Analysis. TGA was coupled with infrared spectroscopy to investigate the thermal stability of modified particles. The three-dimensional IR plots are shown in Figures S5−S7, Supporting Information. The temperature-dependent mass loss of **1**@SiO$_2$ revealed two discernible steps. The first one at 110−300 °C released mainly IBMK adsorbed to the particle surface and ethanol from excess ethoxy groups not reacted during condensation. This mass loss totaled 6%. The second step from 300 °C to 700 °C released CO$_2$, ammonia, water, carbon monoxide, and ethylene, pointing to the thermal decomposition of the maleimidopropyl functionality. During this step 17.5% of the initial mass was lost. Burning of residual carbon under oxygen released additional 6.5%. According to the TGA measurements, 24% of the mass of the **1**@SiO$_2$ sample could be assigned to the coupling agent.

The temperature-dependent mass loss of **3**@SiO$_2$ showed three discernible steps. The first one at 30−200 °C released water adsorbed to the particle surface and ethanol from excess ethoxy groups not reacted during condensation. This mass loss totaled 1.2%. The second step from 200 °C to 360 °C released CO$_2$, ammonia, water, carbon monoxide, and an organic acid, pointing to the thermal decomposition of the maleimido-functionality. During this step 3.2% of the initial mass was lost. The third decomposition step released 22.4% of CO$_2$, water, CO and ethylene. Burning of residual carbon under oxygen released additional 13.7%. According to the TGA measurements, about 39% of the mass of the **3**@SiO$_2$ sample could be assigned to the coupling agent.

The temperature dependent mass loss of **2**@SiO$_2$ showed three discernible steps. The first one at 30−150 °C released water adsorbed to the particle surface and ethanol from excess

ethoxy groups not reacted during condensation. This mass loss totaled 2.0%. The second step from 150 °C to 310 °C released CO$_2$, ammonia, water, carbon monoxide, and an organic acid, pointing to the thermal decomposition of the maleimido functionality. During this step, 3.3% of the initial mass was lost. The third decomposition step released 14.0% of CO$_2$, water, CO, and ethylene. No residual carbon was burned under oxygen. According to the TGA measurements, about 17% of the mass of the **2**@SiO$_2$ sample could be assigned to the coupling agent.

Elemental Analysis. The percentage of nitrogen is the perfect tool to calculate the number of functional groups on the surface of the silica particles, because the nitrogen atoms are only present in the coupling agent and not in residual solvent or ethoxy groups. Equation 1 gives the molar amount of functional groups per gram of particles. This calculation gave 1.5 ± 0.2, 0.3 ± 0.1, and 1.3 ± 0.1 mmol of maleimide per gram of particle for **1**@SiO$_2$, **2**@SiO$_2$, and **3**@SiO$_2$, respectively.

By taking into account the surface area per gram of silica, the number of functional groups per surface area could be calculated (eq 2) and resulted in the following surface coverages: 1.2 ± 0.2 functional groups per nm^2 for **1**@SiO$_2$; 0.3 ± 0.1 functional groups per nm^2 for **2**@SiO$_2$; 1.0 ± 0.1 functional groups per nm^2 for **3**@SiO$_2$.

Diels−Alder Reaction on the Surface of Nanoparticles. The particles were reacted with furan at room temperature to prove their ability to carry out DA reactions. All three samples were isolated and were dispersed in furan by sonication. The suspensions were stirred for 2 days at RT. Afterward the particles were collected by centrifugation, washed three times with diethyl ether, and dried in vacuum. ATR-FTIR, TGA-IR, and elemental analysis were used to characterize the samples F-**1**@SiO$_2$, F-**2**@SiO$_2$, and F-**3**@SiO$_2$.

Afterward retro-DA reaction was carried out at 150 °C in a vacuum-oven. TGA measurements were used to determine the difference in mass loss between the samples before and after retro-DA reaction.

Figure 4 shows a comparison between the IR spectra of **1**@SiO$_2$ and F-**1**@SiO$_2$. The first difference is the small red-shift of

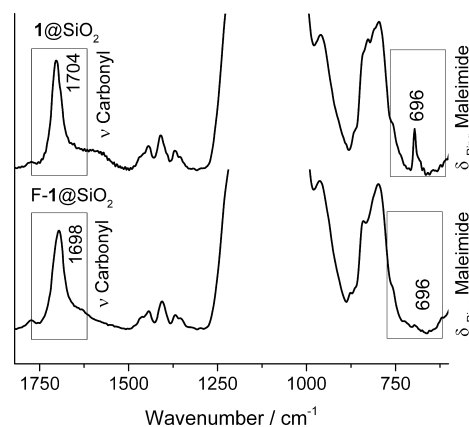
Figure 4. Comparison of **1**@SiO$_2$ and F-**1**@SiO$_2$ by infrared spectroscopy.

the carbonyl peak from 1704 to 1698 cm^{-1}, which could be explained by breaking the conjugation between the carbonyls and the maleimide double bond during DA reaction. On the other hand, the maleimide ring deformation signal at 696 cm^{-1} disappeared almost completely. The integration of this signal

was used to follow the conversion over time of the maleimide system to the DA product.

F-**2**@SiO$_2$ showed the same vibrational changes, but the changes were more difficult to observe. The red-shift of the carbonyl peak is partly overlapped by the signal of the carbamate. Furthermore, the maleimide ring deformation disappeared during the reaction, but initially the signal was very weak.

No clear differences in the spectra of F-**3**@SiO$_2$ and **3**@SiO$_2$ could be observed. The red-shift is covered by carbonyl stretching modes of the additional imide and several signals in the region between 700 and 650 cm^{-1} overlap with the deformation of the maleimide ring, making it impossible to distinguish between these signals.

A comparison of the thermal decomposition between **1**@SiO$_2$ and F-**1**@SiO$_2$ showed a larger mass loss in the sample reacted with furan (Figure 5). The difference between the two
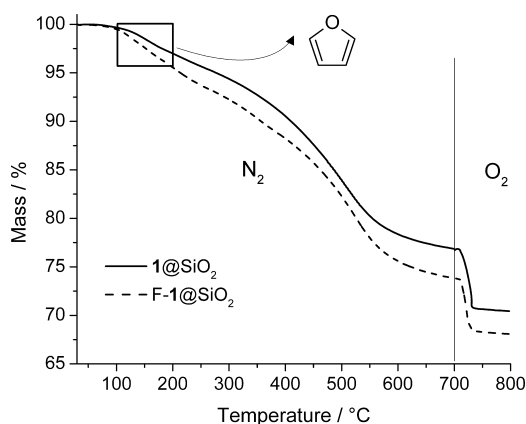

Figure 5. Comparison of TGA measurements of **1**@SiO$_2$ and F-**1**@SiO$_2$.

samples represented 1.62%. This difference was determined from 100 °C to 200 °C because IR measurements of the decomposition gases showed that furan is liberated in between these temperatures. Furan, released by retro-DA reaction, was detected by IR spectroscopy showing the typical strong signal at 745 cm^{-1} characteristic for furan (Figure 6). The maximum release of furan from the sample was detected at 135 °C. Above this temperature, ideal reaction conditions for the rDA reaction
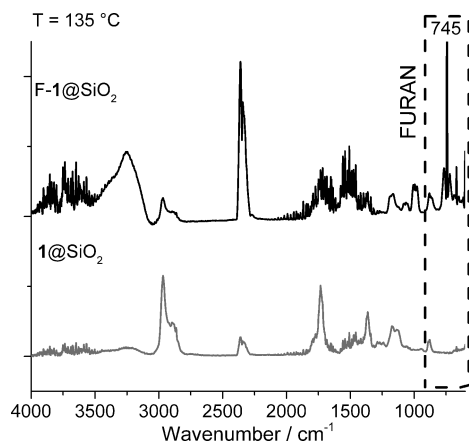

Figure 6. IR Spectra of the decomposition gases at 135 °C of samples **1**@SiO$_2$ and F-**1**@SiO$_2$.

on the surface of nanoparticles should be fulfilled. This 1.62% equals 0.24 mmol furan per gram of particles reacted via DA reaction to the maleimide surface groups. Comparing this value with the number of functional groups per gram of particles, the percentage of groups reacting with furan equals 16%.

TGA of F-**2**@SiO$_2$ gave rise to an additional mass loss of 0.75% between 100 °C and 200 °C (Figure S8, Supporting Information). Taking into account the number of functional groups on the surface of the particles, we could estimate a conversion of 37% of the **2** moieties. F-**3**@SiO$_2$ liberates 1.50% furan, meaning that 17% of the maleimde groups reacted with furan (Figure S9, Supporting Information).

These results suggest that the percentage of maleimide moieties reacting with furan depends on the surface coverage of the particles and not on the type of surface modification. The more the surface of the particles is crowded, the less of the functional groups are able to react. In total, **1**@SiO$_2$ shows the highest amount of furan reacted via DA reaction because these samples show the highest surface coverage of 1.2 molecules per nm^2, but relative to surface coverage it exhibited the lowest reactivity. **2**@SiO$_2$, which presented a much lower coverage of 0.3 molecules per nm^2, showed higher reactivity with respect to the number of functional groups. **1**@SiO$_2$ expressed four times as many maleimides on the surface than **2**@SiO$_2$ but only twice as much furan reacted via DA reaction. This observation suggests that there is an ideal number of surface molecules per nm^2 where both effects are compensated.

Elemental analysis results could not be analyzed as easily because the different decomposition steps cannot be distinguished and only carbon, hydrogen, and nitrogen composition can be obtained. The nitrogen content followed the same trend as the TGA results. For all three samples, the relative nitrogen content was lower if the samples were reacted with furan.

Kinetic Studies of Differently Funtionalized Maleimides. The DA reaction between maleimides with various pendant groups and dimethylfuran (MF) was studied with UV spectroscopy and compared to the surface-functionalized nanoparticles. All the reactions followed the same scheme as that shown in Scheme 4.

Scheme 4. General Reaction Scheme for Model DA Reactions
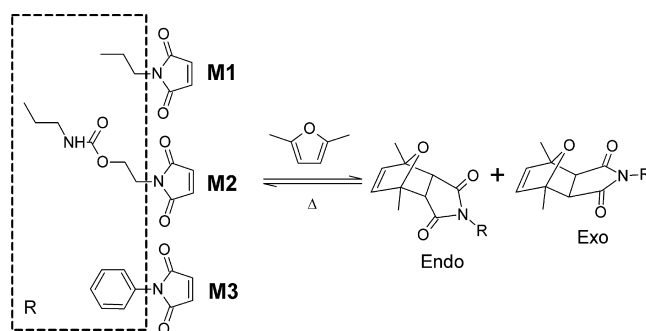
The proportions of exo and endo products are not relevant in the context of the use of DA reaction as a cross-linking reaction between nanoparticles and macromolecular systems. Kinetic studies were only performed to compare reactivity of the maleimdes and to study the effects of different functionalities on the rate constant k. Given the structures of the used coupling agents for particle functionalization, we chose three different model compounds for preliminary kinetic

studies. These model compounds were *N*-propylmaleimide **M1**, *N*-ethyl(*N*-propylcarbamato)maleimide **M2**, and *N*-phenyl-maleimide **M3**, respectively. Whereas the UV spectrum of MF in 1,2-dichloroethane did not show any absorption above 270 nm, **M1** in the same solvent (c = 0.02 M) displayed a characteristic maximum at about 290 nm (ε_λ = 656 M^{-1} cm^{-1}) arising from the excitation of the conjugated system of C=C and C=O bonds. During the reaction and as the DA products form, this conjugation breaks, which results in the hipsocromic shift of the absorption corresponding now to the excitation of the remaining carbonyls. The progress of DA reaction could therefore be followed by UV spectroscopy by keeping track of the decrease of the absorbance at 290 nm (for **M1**) with time. This was carried out for the three molecules at different temperatures, specifically 50 °C, 60 °C, and 70 °C. The maximum absorptions for **M2** and **M3** were at 298 nm (ε_λ = 348 M^{-1} cm^{-1}) and 295 nm (ε_λ = 457 M^{-1} cm^{-1}), respectively. Figures S10−S12 (Supporting Information) show the results of kinetic measurements of the three molecules at 60 °C with a 30-fold excess of MF. The high excess of MF was chosen to guarantee pseudo-first-order kinetics with regard to the maleimides and to minimize reaction time. A first experiment with a 10-fold excess of MF lasted several hours, so the concentration of MF was tripled.

Figure S10 shows the natural logarithm of the conversion over time of the three different model maleimides. Table 1 lists

Table 1. Reaction Rate Constants k for Temperatures 50 °C, 60 °C, and 70 °C for Model DA Reactions (confidence interval 95%)

model compound	k [10^{-4} s^{-1}], T = 50 °C	k [10^{-4} s^{-1}], T = 60 °C	k [10^{-4} s^{-1}], T = 70 °C
M1	3.8 ± 0.1	6.2 ± 0.1	12.0 ± 0.3
M2	9.0 ± 0.6	13.3 ± 1.0	15.8 ± 2.7
M3	11.9 ± 0.6	21.6 ± 1.7	28.8 ± 0.4

the reaction rate constants k for each temperature as calculated from the slope of the graphics in Figures S13−15, Supporting Information. Only the linear domain was used to calculate the rate constants because the reactions are not quantitative. The back reaction takes place in different amounts depending on the temperature and the nature of maleimides. As we were only interested in a comparison of the rate at which the reactions take place, we do not take into account measurements near the reaction equilibrium.

Analysis at the k values at 50 °C showed that **M1** is the slowest reactant for the conversion with MF because the propyl chain increases the electron density in the maleimide system, raising the energy level of the LUMO of the dienophile and therefore decreasing energy compatibility of reactive orbitals. The urethyl functionality in **M2** is withdrawing electron density from the maleimide system, therefore lowering the energy level of the LUMO and increasing the interaction with the HOMO of the diene. The phenyl ring of **M3** withdraws even more electron density from the system, which results in even a higher reaction rate constant with regard to **M1**.

Kinetic Studies at the Surface of Particles with Furan at RT. To investigate if the reaction rate is drastically changed at the surface of nanoparticles, the reaction rate constant was estimated by monitoring the maleimide ring deformation signal in the infrared spectra during DA reaction on the surface of silica nanoparticles. Unfortunately, this method could only be

used for the propylmaleimide **1**-modified samples because integration of the signal at 696 cm^{-1} over time gave no evaluable results for the other samples. A 200 mg amount of **1**@SiO$_2$ was dispersed in 20 mL of 2-propanol, and 1 mL of furan was added. Samples were withdrawn from this suspension after various time intervals. The samples were dried immediately, and ATR-IR measurements were carried out (Figure 7). The spectra were normalized using the strongest
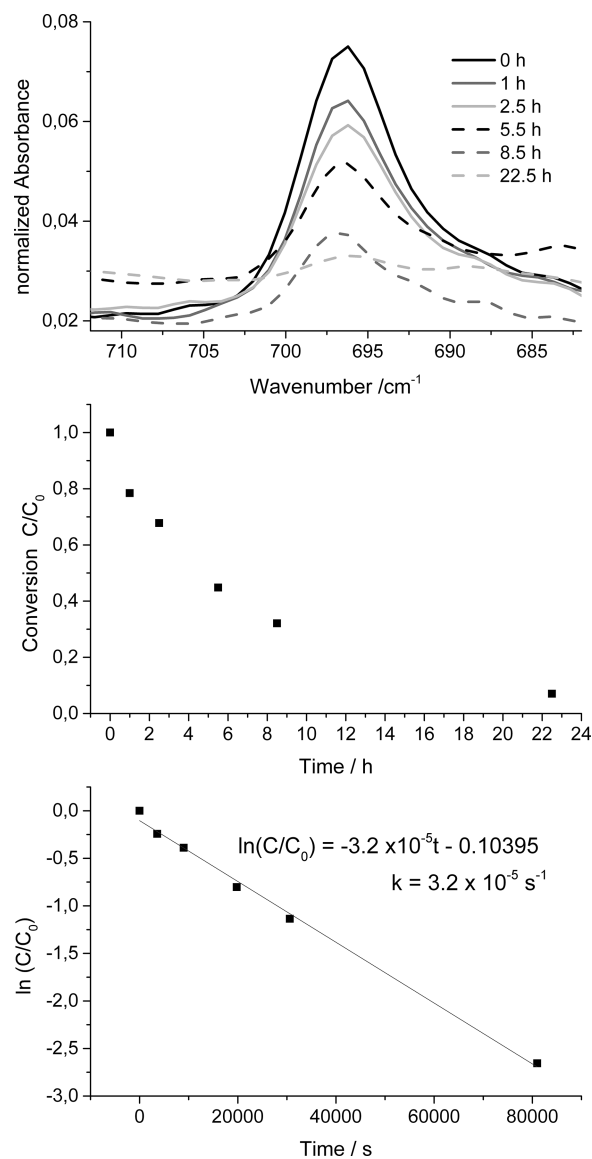
Figure 7. (a) Infrared spectra of **1**@SiO$_2$ at different time intervals during the reaction with furan. (b) Conversion over time plot. (c) Plot for first-order kinetics as a function of the linear fit and reaction rate value k.

unchanged signal, the asymmetric Si−O−Si stretching, as reference to obtain quantitative information. After a basis line correction, the area under the signal at 696 cm^{-1} was used to plot the conversion against reaction time. The conversion follows exponential decay, as in the case for first-order kinetics (Figure 7). The kinetic rate constant is in the order of 10^{-5} s^{-1}. This value is in the same order of magnitude as that for the reaction rate in the case of molecular systems at room temperature, meaning that the reaction rate is not significantly

154

dx.doi.org/10.1021/cm303049k | *Chem. Mater.* 2013, 25, 149−157

altered by surface effects. UV/Vis spectroscopic measurements could not be performed because of the light scattering properties of the silica nanoparticles.

■ CONCLUSIONS

This study ascertained that the conditions chosen to conduct surface modification of nanosized silica particles, involving an exchange of the suspension medium from methanol to IBMK, ensures high surface coverage and low agglomeration of the particles. The low dielectric constant of toluene makes it a poor choice because ionization of surface silanols is unlikely.

Another goal of this work was to determine the reactivity of differently substituted maleimides. It was shown in molecular systems that phenyl-substituted maleimides are three times more reactive than propyl-substituted maleimdes. Furthermore, it has been demonstrated that the amount of active sites for the DA reaction on the surface of silica nanoparticles is dependent on the grafting density of the dienophile species. The higher the grafting density and the sterical effects near the reaction site, the lower the conversion of DA reaction. Already reacted furan/maleimide groups interfere with other approaching furan molecules, hindering the continuation of DA reaction. Finally, a kinetic study of DA reactions between maleimide moieties on surfaces and molecular furan has shown that surface effects do not dramatically decrease the reaction rate.

■ EXPERIMENTAL SECTION

Methods. Fourier transform infrared spectroscopy (FT-IR) measurements were performed on a Bruker Vertex 70 Spectrometer under ambient air (40 scans at a resolution of 4 cm^{-1}) in attenuated total reflectance (ATR) mode. Thermogravimetric analysis (TGA) were performed on a Netzsch Iris TG 209 C in an alumina crucible heating from room temperature to 700 °C under nitrogen followed by heating to 800 °C under oxygen with a rate of 20 K min^{-1}. Differential scanning calorimetry (DSC) measurements were carried out on a Netzsch DSC 204 F1 Phoenix calorimeter in aluminum crucibles with pierced lids, heating under nitrogen with a rate of 15 K min^{-1}. Liquid-state NMR spectra were recorded on a Bruker AC 200F spectrometer (^{1}H at 200.13 MHz, ^{13}C at 50.32 MHz). Liquid-state ^{29}Si NMR spectra were recorded on a Bruker Avance 300 spectrometer at 69.63 MHz. Elemental analysis was carried out on a Leco 900 CHN Analysator. The percentage of nitrogen was used to calculate the number of functional groups on the surface of the silica particles. Equation 1 gives the molar amount of functional groups per gram of particles:

$$c_{FG} = \frac{100}{\Delta m_{SiO_2}} \times \frac{\Delta m_N}{M_N} \times \frac{0.01}{N} \quad (1)$$

where c_{FG} is the molar concentration of functional groups per gram [mol g^{-1}], Δm_{SiO_2} is the residual mass of SiO$_2$ from TGA measurement [%], Δm_N is the mass of nitrogen from EA [%], M_N is the molar mass of nitrogen [g mol^{-1}], and N is the number of nitrogen atoms per functional group.

By taking into account the surface area per gram of silica, the number of functional groups per surface area N_{FG-A} can be calculated according to eq 2:

$$N_{FG-A} = c_{FA} \times N_A \times \frac{1}{A} \times 10^{-18} \quad (2)$$

where N_{FG-A} is the number of functional groups per area [nm^{-2}], n_{FG} is the molar concentration of functional groups per gram [mol g^{-1}], N_A is Avogadro's number, and A is the specific surface area of the nanoparticles per gram [m^2 g^{-1}].

Transmission electron microscopy (TEM) images were recorded on a JEOL JEM-2010 microscope. The samples were attached to Plano S160-3 copper grids by dispersing them in ethanol using an ultrasound

cleaning bath, adding one drop (30 µL) on the copper grid and evaporating the solvent.

Dynamic light scattering (DLS) measurements were carried out by noninvasive backscattering on an ALV/CGS-3 compact goniometer system with an ALV/LSE-5003 correlator and multiple tau correlator at a wavelength of 632.8 nm (He−Ne Laser) and at a 90° goniometer angle. The dispersing media were purified before use with a syringe filter (200 nm mesh). The determination of the particle radius was carried out by the analysis of the correlation function via the g2(t) method followed by a linearized number-weighting (n.w.) of the distribution function.

Nitrogen sorption measurements were performed on a Sorptomatic 1900 instrument from Fisons Instruments at 77 K. The samples were degassed under vacuum at 60 °C for at least 2 h prior to measurement. The surface area was calculated according to Brunauer, Emmett, and Teller (BET).

Materials. Tetraethyl orthosilicate (TEOS) was provided by Wacker Silicones. 3-Aminopropyltriethoxysilane (APTES), 3-isocyanatopropyltriethoxysilane, 1,1′-(methylenedi-4,1-phenylene)-bismaleimide, isobutyl methyl ketone, dry toluene, dry dichloromethane, furan, dimethylfuran, hexamethyldisilazane, and dibutyltin dilaurate (95%) were purchased from Sigma-Aldrich and were used as received. All other solvents and chemicals were purchased from the central chemical depot of the Saarland University and dried according to standard procedures if necessary. Zinc chloride was purified in boiling dioxane with zinc dust and recrystallized from dioxane.

Synthesis of Silica Nanoparticles. The silica nanoparticles were synthesized according to a modified literature procedure.[20] In a 250 mL round-bottom flask, methanol (100 mL) was mixed with 51 mg (1.0 mmol) of 33% ammonia and 1.98 g (110 mmol) of water and stirred for 10 min. Then 10.41 g (50 mmol) of TEOS were added. The solution was stirred for 2 days, and a part of the particles was isolated to characterize the unmodified sample. The particles were precipitated with 100 mL of hexane and 50 mL of diethyl ether. Afterwards they were isolated and washed three times with ethanol by centrifugation at 13000 rpm and dried overnight in a vacuum oven (≈50 mbar) at 60 °C. Yield: 1.5 g silica particles; TEM: diameter 3.8 ± 0.9 nm; DLS: diameter 4.8 ± 0.8 nm; surface area: BET 750 m^2 g^{-1}.[12]

Synthesis of N-((3-Triethoxysilyl)propyl)maleimide 1. The synthesis was carried out following a literature procedure.[15] The reaction was carried out under argon atmosphere. In a 250 mL three-neck round-bottom flask equipped with a dropping funnel, 1.73 g (17.6 mmol) of maleic anhydride were dissolved in 60 mL of dry dichloromethane. A mixture of 3.90 g (17.6 mmol) of 3-(aminopropyl)triethoxysilane (APTES) and 20 mL of dry dichloromethane were added through a dropping funnel while stirring. After allowing the mixture to stand for 1 h at room temperature, the solvent was removed under vacuum. The intermediate product was collected as a white powder. ^{1}H NMR (200.13 MHz, CDCl$_3$, 25 °C) δ = 0.68 (t, ^3J = 7.7 Hz, 2H), 1.23 (t, ^3J = 7.0 Hz, 9H), 1.74 (p, ^3J = 7.7 Hz, 2H), 3.39 (q, ^3J = 6.5 Hz, 2H), 3.84 (q, ^3J = 7.0 Hz, 6H), 6.33 (s, 2H), 7.83 (br s, 1H). ^{13}C NMR (50.32 MHz, DMSO-d_6, 25 °C) δ = 7.80 (CH$_2$Si), 18.24 (CH$_3$CH$_2$O), 21.95 (CH$_2$CH$_2$CH$_2$), 42.64 (CH$_2$NH), 58.59 (CH$_3$CH$_2$O), 131.54 (=CHCONH), 136.08 (=CHCOOH), 165.56 (COOH), 166.03 (CONH).

In the next step, the intermediate product was dissolved in 60 mL of dry toluene, and 2.40 g (17.6 mmol) of zinc chloride were added at once. After the reaction mixture was heated to 80 °C, a solution of 2.84 g (17.6 mmol) of hexamethyldisilazane with 20 mL of toluene was added dropwise. The temperature was held during 5 h at 80 °C. After cooling, the solution was filtered to remove zinc chloride and the solvent was removed in vacuum. Yield: 5.12 g (17.0 mmol; 96.5%) of a colorless oily liquid. ^{1}H NMR (200.13 MHz, CDCl$_3$, 25 °C) δ = 0.55−0.64 (m, 2H), 1.22 (t, ^3J = 6.9 Hz, 9H), 1.62−1.78 (m, 2H), 3.51 (t, ^3J = 7.37 Hz, 2H), 3.81 (q, ^3J = 6.9 Hz, 6H), 6.68 (s, 2H). ^{13}C NMR (50.32 MHz, CDCl$_3$, 25 °C) δ = 7.49 (CH$_2$Si), 18.25 (CH$_3$CH$_2$O), 25.06 (CH$_2$CH$_2$CH$_2$), 45.36 (CH$_2$N), 58.44 (CH$_3$CH$_2$O), 134.21 (HC=CH), 171.10 (C=O). ^{29}Si NMR (59.63 MHz, CDCl$_2$, 25 °C) δ = −46.34. IR (cm^{-1}): 3099, 2974, 2932, 2887, 1770, 1703, 1440,

1406, 1365, 1255, 1220, 1166, 1101, 1072, 956, 829, 783, 756, 694, 453.

Synthesis of Protected Maleic Anhydride 3,6-Epoxy-1,2,3,6-tetrahydrophthalic Anhydride 4. The synthesis was carried out following a modified literature procedure.[16] In a 250 mL three-neck round-bottom flask under argon atmosphere, 20 g (0.204 mol) of the maleic anhydride and 14.04 g (0.206 mol) of furan were dissolved in 100 mL of toluene. The mixture was stirred for 24 h at room temperature. A white precipitate formed during this time. The solid was collected by filtration and washed two times with cold diethyl ether. The filtrate was reduced by rotary evaporation to 20 mL and cooled to 4 °C overnight. A second crop crystallized which was again collected by filtration and washed with diethyl ether. Finally, the crystals were dried in vacuum ($\approx 10^{-2}$ mbar) overnight. Yield: 27.36 g (0.165 mol; 80.6%) of a white solid. ^{1}H NMR (200.13 MHz, CDCl$_3$, 25 °C) δ = 3.01 (s, 2 H), 5.40 (s, 2 H), 6.57 (s, 2 H). ^{13}C NMR (50.32 MHz, CDCl$_3$, 25 °C) δ = 47.52 (CH), 81.40 (CHO), 136.67 (C=C), 175.29 (C=O). IR (cm^{-1}): 3606, 3143, 3099, 3089, 3066, 3033, 3000, 2991, 1857, 1780, 1309, 1282, 1230, 1211, 1193, 1145, 1083, 1018, 948, 921, 902, 877, 848, 821, 800, 732, 690, 674, 634, 574, 428. Onset of decomposition (DSC, N$_2$, 15 K min^{-1}): 117.9 °C. Elemental analysis (%): Calcd for C$_8$H$_6$O$_4$: C 57.84, H 3.64, N 0.00; Found: C 56.75, H 3.71, N 0.00.

Synthesis of Protected 2-Hydroxyethylmaleimide 5. The synthesis was carried out following a modified literature procedure.[16] In a 100 mL round-bottom flask equipped with a reflux condenser, 5.80 g (35 mmol) of **4** were dissolved in 30 mL of dry MeOH. Afterwards 2.14 g (35 mmol) of ethanolamine were added dropwise at 0 °C. The mixture was refluxed for 24 h. The MeOH was removed by rotary evaporation, and the crude product was recrystallized from diethyl ether at −20 °C. The crystals were collected by filtration and washed with cold diethyl ether. Reducing the filtrate and recrystallizing again gained a second crop. The final product was dried in vacuum ($\approx 10^{-2}$ mbar) overnight. Yield: 5.75 g (18.5 mmol; 52.7%) of a white solid. ^{1}H NMR (200.13 MHz, CDCl, 25 °C) δ = 0.86 (bs, 1H), 2.90 (s, 2H), 3.76 (m, 4H), 5.30 (s, 2H), 6.54 (s, 2H). ^{13}C NMR (50.32 MHz, CDCl$_3$, 25 °C) δ = 41.74 (CHOCHC=O), 47.46 (NCH$_2$), 60.22 (CH$_2$OH), 80.95 (HCO), 136.49 (C=C), 176.74 (C=O). IR (cm^{-1}): 3473, 3097, 3026, 3006, 2993, 2972, 2931, 2895, 1766, 1681, 1469, 1434, 1404, 1386, 1334, 1317, 1286, 1267, 1218, 1168, 1155, 1099, 1053, 1033, 1012, 958, 937, 916, 873, 850, 806, 771, 721, 703, 653, 594, 563, 530, 487, 428. Onset of decomposition (DSC, N$_2$, 15 K min^{-1}): 138.1 °C. Elemental analysis (%): Calcd for C$_{10}$H$_{11}$NO$_4$: C 57.41, H 5.30, N 6.70; Found: C 57.39, H 5.43, N 6.59.

Synthesis of Protected 2-(2,5-Dioxo-2,5-dihydro-1*H*-pyrrol-1-yl)ethyl 3-(Triethoxysilyl)propylcarbamate 2. The reaction was carried out under argon atmosphere. In a 100 mL three-neck round-bottom flask, 935 mg (3 mmol) of protected hydroxyethyl maleimide **5** was suspended in 10 mL of dry acetone. 890 mg (3.6 mmol) 3-Isocyanotopropyltriethoxysilane were added via a syringe while stirring. The solution was stirred at reflux overnight followed by the addition of 3 drops of dibutyltin dilaurate catalyst. The reaction mixture was refluxed for an additional 1 h. The crude mixture was concentrated under vacuum and washed with hexane three times. ^{1}H NMR (200.13 MHz, CDCl$_3$, 25 °C) δ = 0.56 (t, ^3J = 7.9 Hz, 2H), 1.17 (t, ^3J = 7.0 Hz, 9H), 1.54 (m, 2H), 2.84 (s, 2H), 3.09 (m, 2H), 3.67 (m, 2H), 3.77 (q, ^3J = 7.0 Hz, 6H), 4.13 (t, ^3J = 5.0 Hz, 2H), 5.20 (s, 2H), 6.48 (s, 2H). ^{13}C NMR (50.32 MHz, CDCl$_3$) δ 7.46 (CH$_2$Si), 18.24 (CH$_3$CH$_2$O), 23.17 (CH$_2$CH$_2$CH$_2$), 37.38 (OCH$_2$CH$_2$N), 41.74 (CHOCHC=O), 43.39 (CH$_2$NCO), 58.41 (CH$_3$CH$_2$O), 61.71 (CH$_2$OCN), 80.90 (HCO), 136.17 (C=C), 155.97 (NCOO), 170.48 (C=O). ^{29}Si NMR (59.63 MHz, CDCl$_2$, 25 °C) δ = −45.72. IR (cm^{-1}): 3356, 3080, 2974, 2927, 2885, 1774, 1701, 1600, 1512, 1436, 1388, 1361, 1336, 1240, 1222, 1190, 1166, 1099, 1074, 1022, 954, 877, 854, 771, 717, 648, 594, 530, 470, 428.

Syntheses of 1-(4-{[4-(2,5-Dioxo-3-{[3-(triethoxysilyl)-propyl]amino}pyrrolidin-1-yl)phenyl]methyl}phenyl)-2,5-dihydro-1*H*-pyrrole-2,5-dione 3. The reaction was carried out under argon atmosphere. In a 100 mL round-bottom flask, 2 g (5.8 mmol) of 1,1′-(methylenedi-4,1-phenylene)bismaleimide were dissolved in 50

mL of chloroform. 1.1 g (5 mmol) APTES were added, and the mixture was stirred for 12 h at RT. The crude product was used without further purification. ^{1}H NMR (200.13 MHz, CDCl$_3$, 25 °C) δ = 0.69 (t, ^3J = 8.0 Hz, 2H), 1.24 (t, ^3J = 7.0 Hz, 9H), 1.72 (m, 2H), 2.72 (m, 2H), 3.03−3.42 (m, 2H), 3.84 (q, ^3J = 7.0 Hz, 6H), 3.99 (s, 1H), 4.05 (s, 2H), 6.86 (s, 2H), 7.29 (m, 8H). ^{13}C NMR (50.32 MHz, CDCl$_3$) δ = 7.62, 18.09, 23.91, 36.62, 40.95, 46.48, 53.58, 58.11, 126.31, 126.51, 129.27, 129.51, 134.02, 140.02, 140.81, 168.16, 175.19, 176.31. ^{29}Si NMR (59.63 MHz, CDCl$_2$, 25 °C) δ = −46.03. IR (cm^{-1}): 3346, 3039, 2974, 2931, 2885, 1776, 1703, 1670, 1512, 1438, 1382, 1307, 1168, 1101, 1074, 1020, 952, 856, 811, 773, 671, 605, 513, 466, 408.

Solvent Exchange. Methanol was exchanged with isobutyl methyl ketone (IBMK) by adding 20 mL of IBMK to 50 mL of the particle suspension. A first fraction of methanol and excess ammonia were removed by rotary evaporation to reach a volume of approximately 10 mL. Then a second volume of 10 mL of IBMK was added, and the suspension was again concentrated to approximately 10 mL. This procedure was repeated two times. Afterwards the suspension was diluted with 90 mL of fresh IBMK.

Surface Functionalization of Silica Particles in IBMK. In a 250 mL three-neck round-bottom flask with a reflux condenser, 2 g of **1**, 3 g of **2**, or 3 g of the crude **3** was added to the silica particle suspension in IBMK and heated to 115 °C for 24 h. Afterwards the suspension was cooled to room temperature, and half of the solvent was removed by rotary evaporation. The particles were isolated by centrifugation at 13000 rpm for 10 min. Afterwards they were washed three times with acetone and dried overnight in a vacuum oven (≈ 50 mbar) at 80 °C. The particles were stored in a desiccator over P$_2$O$_5$. Yield: 0.8 g of yellowish particles.

■ ASSOCIATED CONTENT

ⓢ Supporting Information

Supplementary infrared spectra, TGA/FTIR data, and UV/Vis spectra. This material is available free of charge via the Internet at http://pubs.acs.org.

■ AUTHOR INFORMATION

Corresponding Author

*E-mail: kickelbick@mx.uni-saarland.de.

Notes

The authors declare no competing financial interest.

■ REFERENCES

(1) Feichtenschlager, B.; Lomoschitz, C. J.; Kickelbick, G. *J. Colloid Interface Sci.* **2011**, *360*, 15.

(2) Lomoschitz Christoph, J.; Feichtenschlager, B.; Moszner, N.; Puchberger, M.; Muller, K.; Abele, M.; Kickelbick, G. *Langmuir* **2011**, *27*, 3534.

(3) Delattre, L.; Dupuy, C.; Babonneau, F. *J. Sol-Gel Sci. Technol.* **1994**, *2*, 185.

(4) Chen, X.; Wudl, F.; Mal, A. K.; Shen, H.; Nutt, S. R. *Macromolecules* **2003**, *36*.

(5) Gandini, A.; Coelho, D.; Silvestre, A. J. D. *Eur. Polym. J.* **2008**, *44*, 4029.

(6) Gousse, C.; Gandini, A.; Hodge, P. *Macromolecules* **1998**, *31*, 314.

(7) Liu, X.; Zhu, M.; Chen, S.; Yuan, M.; Guo, Y.; Song, Y.; Liu, H.; Li, Y. *Langmuir* **2008**, *24*, 11967.

(8) Tesoro, G. C.; Sastri, V. R. *Ind. Eng. Chem. Prod. Res. Dev.* **1986**, *25*, 444.

(9) Costanzo, P. J.; Beyer, F. L. *Chem. Mater.* **2007**, *19*, 6168.

156

dx.doi.org/10.1021/cm303049k | *Chem. Mater.* 2013, 25, 149−157

(10) Vejayakumaran, P.; Rahman, I. A.; Sipaut, C. S.; Ismail, J.; Chee, C. K. *J. Colloid Interface Sci.* **2008**, *328*, 81.

(11) Stoeber, W.; Fink, A.; Bohn, E. *J. Colloid Interface Sci.* **1968**, *26*, 62.

(12) Brunauer, S.; Emmett, P. H.; Teller, E. *J. Am. Chem. Soc.* **1938**, *60*.

(13) Sing, K. S. W.; Everett, D. H.; Haul, R. A. W.; Moscou, L.; Pierotti, R. A.; Rouquerol, J.; Siemieniewska, T. *Pure Appl. Chem.* **1985**, *57*, 603.

(14) Huang, C.; Tassone, T.; Woodberry, K.; Sunday, D.; Green, D. L. *Langmuir* **2009**, *25*, 13351.

(15) Proupin-Perez, M.; Cosstick, R.; Liz-Marzan, L. M.; Salgueirino-Maceira, V.; Brust, M. *Nucleosides Nucleotides Nucleic Acids* **2005**, *24*, 1075.

(16) Adachi, K.; Achimuthu, A. K.; Chujo, Y. *Macromolecules* **2004**, *37*.

(17) Beganskiene. *Mater. Sci. (Medziagotyra)* **2004**, *10*, 287.

(18) Knofel, C.; Martin, C.; Hornebecq, V.; Llewellyn, P. L. *J. Phys. Chem. C* **2009**, *113*, 21726.

(19) Parker, S. F.; Mason, S. M.; Williams, K. P. J. *Spectrochim. Acta, Part A* **1990**, *46A*, 315.

(20) Kickelbick, G.; Holzinger, D.; Ivanovici, S. Organically Functionalized Silica Nanoparticles. In *Materials Syntheses*; Schubert, U., Hüsing, N., Laine, R., Eds.; Springer: Wien, 2008; pp 127−133.

3.2   Self-healing nanocomposites from silica-polymer core-shell nanoparticles

As the use of silica nanoparticles functionalized with short maleimide containing coupling agents revealed to be a poor choice for self-healing nanocomposites, a completely different approach was established. In order to increase the distance between the particle surface and the functional DA groups, a grafting-from polymerization technique was chosen. Starting from initiator-modified SiO_2 nanoparticles, a reactive polymeric shell can be created by surface-initiated atom transfer polymerization (SI-ATRP). Maleimide or furan moieties can be introduced in the form of polymerizable monomers. Therefore furfuryl methacrylate (FMA) and a protected maleimide methacrylate (pMiMA) were synthesized. The maleimide double bond had to be protected by DA reaction with furan in order to prevent polymerization of the maleimide. The aromatic character of the furfuryl ring prevents polymerization under radical conditions. The use of FMA and pMiMA without a comonomer would yield a glass transition temperature of the polymeric shell exceeding 100 °C, which averts DA reaction by lowering the mobility of the macromolecules. As DA reaction typically takes place from room temperature to 90 °C, a relatively low glass transition temperature is of advantage. Therefore a comonomer with flexible side groups can be added. Poly(butyl methacrylate) (PBMA) has a glass transition temperature situated around room temperature. Therefore butyl methacrylate (BMA) was used as a comonomer for the polymer shell created by ATRP. A ratio of BMA and FMA of 10:1 was employed because low functionalities increase the length of polymer segments between cross-links thereby increasing flexibility and reactivity. The more flexible the chains the easier the DA reaction can achieve its six-centred transition state, which is necessary for an optimal overlapping of the π-orbitals of diene and dienophile.

Standard ATRP afforded the polymer matrix used as counter-part for the self-healing material. Under these conditions the same monomers yielded linear polymers with low polydispersity index. In the case of the protected maleimide monomer, lower reaction temperature was necessary in order to prevent deprotection resulting in an irreversibly cross-linked polymer network. In polar solvents, linear tridentate ligands for Cu ions such as *N,N,N',N',N''*-pentamethyldiethylenetriamine (PMDETA) are more reactive than linear tetradentate ligands like 1,1,4,7,10,10-

hexamethyltriethylenetetramine (HMTETA). The Cu^{II}/PMDETA complex is stronger than the Cu^{II}/HMTETA complex, which increases the concentration of the active radical species and the reaction rate. By using toluene as solvent, these reactivities are switched. Cu^{I}/PMDETA is more soluble in toluene as Cu^{I}/HMTETA because of the less ionic character of the complex. Modeling and EXAFS measurements in toluene at room temperature suggest the neutral complex with the structure Cu^{I}(PMDETA)Br.[105]

On the other hand, Cu^{I}Br is likely to form the ionic complex $[Cu^{I}(HMTETA)^{+}][Cu^{I}Cl_2]^{-}$.[106] The much higher solubility of Cu^{I}/PMDETA in toluene lowers the equilibrium constant K_{ATRP} by increasing the ratio $[Cu^{II}$/PMDETA]:$[Cu^{I}$/PMDETA].

In the same way, low solubility of Cu^{I}/HMTETA allows to increase the reactivity and lower the reaction temperature to 70 °C. No RDA and no gel formation were observed at this temperature.

The furan used to protect the maleimide moieties had to be removed after polymerization. RDA reaction at temperatures above 120 °C liberated the volatile furan molecule in just a few minutes. A milder method is the deprotection in boiling toluene. Therefore P(BMA-co-pMiMA) was dissolved in toluene and heated for several hrs to 110 °C. Air cooling was used to avoid condensation of furan. FTIR and DSC measurements showed complete RDA reaction and the mass loss from 90 to 200 °C could be used to calculate the maleimide content.

Self-healing inorganic/organic materials were prepared by mixing the previously dispersed core-shell silica nanoparticles with a deprotected P(BMA-co-MiMA) polymer matrix in solution. After removal of the solvent, the nanocomposite could be molded and cured at 70 °C. During the curing phase DA reaction between FMA and MiMA fragments took place. FTIR, rheology and UV-Vis spectroscopy was used to follow the reaction. Maximum conversion was achieved after approximately 12 hrs. The reversibility of the cross-linking could be demonstrated by UV-Vis spectroscopy over several DA/RDA cycles. Additionally, DSC measurements indicated an endothermic reaction at high temperatures. Relatively low mobility within the polymer matrix hampered fast reconnection during cooling. Cooling could only reform a small part of the initial DA bonds. Annealing for 12 hrs above glass transition temperature was essential to ensure maximum DA connectivity.

Scratch healing experiments were performed and investigated by light microscopy. Complete closure of scratches was observed after heat treatment. RDA dissociates the cross-links allowing thermoplastic flow and closure of the scratch interface by newly formed entanglements.

The results have been published in a special edition of *Polymer International* dedicated to Krzysztof Matyjaszewski:

T. Engel, G. Kickelbick, Self-healing nanocomposites from silica–polymer core–shell nanoparticles, *Polym. Int.* **2014**, *63*, 915-923. © 2013 Society of Chemical Industry
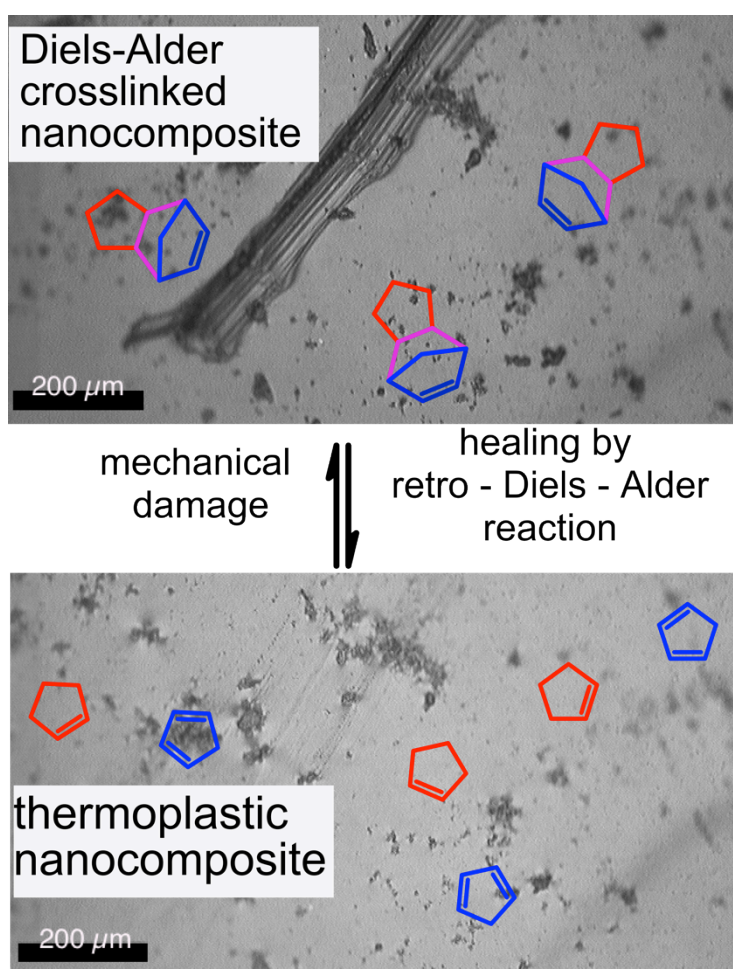
FIGURE 10: *TABLE OF CONTENT*: HEALING OF MECHANICAL DAMAGE (SURFACE SCRATCH) TRIGGERED BY A HEAT TREATMENT AND SCHEMATIC REPRESENTATION OF RETRO-DIELS-ALTER REACTION INVOLVED IN THE HEALING MECHANISM.

Research Article

SCI

Self-healing nanocomposites from silica — polymer core — shell nanoparticles

Tom Engel and Guido Kickelbick*

Abstract

A copolymer containing butyl methacrylate in a 10-fold excess and furan-protected maleimidopropyl methacrylate was synthesized via atom transfer radical polymerization (ATRP). Maleimide functionalities served as dienophiles for reversible crosslinking by Diels — Alder (DA) reactions. As counterpart to the linear polymer, silica — polymer core — shell nanoparticles with grafted furfuryl groups were prepared by surface-initiated ATRP. Rheological measurements during the DA reaction at 80 °C showed an increase in storage modulus due to crosslinking within the nanocomposite. DSC allowed the detection of the endothermic retro-DA reaction above 120 °C, which provided the possibility to self-heal scratches. Repeated curing/de-crosslinking was detected using UV−visible spectroscopy and revealed the reproducibility of the thermoreversible crosslinking reaction, which is a prerequisite for the self-healing mechanism. Finally, the scratch-healing abilities of the material were verified on composite films.
© 2013 Society of Chemical Industry

Supporting information may be found in the online version of this article.

Keywords: ATRP; core — shell nanoparticles; thermoreversible crosslinking; self-healing; Diels — Alder

INTRODUCTION

Since the introduction of atom transfer radical polymerization (ATRP),[1] considerable effort has been devoted to applying 'living' radical polymerization techniques to the design of nanostructured materials.[2] One of the major applications of controlled radical polymerization is the preparation of polymer structures, such as brushes, on surfaces.[3−7] ATRP is an effective strategy to build tailored interfaces between inorganic surfaces and polymeric materials, allowing the control of chain length, molecular weight distribution and surface coverage.[8]

Planar surfaces of various chemical compositions, e.g. silicon, silica or gold, have been functionalized via ATRP.[8−13] However, the main focus lies in the preparation of inorganic–organic core–shell particles. These composite particles are utilized in the areas of coatings, electronics, catalysis, separations, and diagnostics.[14,15]

The core may be composed of a metal, such as gold,[16−18] or oxides, such as silica, titania, iron oxide, zinc oxide, or zirconia.[19−22] The polymeric shell is usually prepared by the attachment of an ATRP initiator and a grafting-from polymerization. The composition of the polymers, which is determined by the choice of monomers or mixtures of monomers, allows the surface properties of the particles to be changed, which leads for example to an increase in the stability of a particle suspension[23] or a change in the biocompatibility[24] of the particles. Stimuli-responsive polymer shells can be used for biomedical applications such as drug delivery.[25]

In materials chemistry self-healing polymers attracted some attention in recent years. Diels — Alder (DA) chemistry between maleimide and furan moieties has been widely used to synthesize self-healing materials.[26−32] One of the most relevant aspects of the DA reaction for re-mendable polymers is its thermal reversibility,

known as the retro-DA (rDA) reaction.[33] Wudl *et al.* showed that materials prepared with this thermoreversible mechanism reveal mechanical properties equal to those of commercially available epoxy resins, but a thermal treatment at a temperature above 120 °C allowed un-crosslinking of the network, thereby increasing processability and reuseability.[28,29] ATRP was also used to prepare self-healing polymers. Kavitha and Singha synthesized a copolymer of methyl methacrylate and furfuryl methacrylate (FMA), which was further reacted with a bis-maleimide crosslinker.[34] Wouters *et al.* formulated a coating using butyl methacrylate (BMA) and FMA as monomers. BMA lowers the glass transition temperature T_g of the resulting polymer, thereby increasing mobility of the macromolecules at low temperatures and facilitating the DA reaction.[26]

In a previous study we showed that silica nanoparticles grafted with molecular maleimido-silane coupling agents inhibit DA reactivity of the dienophile groups due to steric effects near the particle surface.[35] One solution to this problem is to increase the distance between the particle surface and the functional groups by a grafting-from polymerization of a copolymer containing DA reactive moieties. Such a strategy also allows tailoring the number of reactive groups by choosing the ratio between reactive and unreactive monomers. In this study we show the preparation of a self-healing nanocomposite using ATRP, surface ATRP and DA crosslinking techniques.

* Correspondence to: Guido Kickelbick, Inorganic Solid State Chemistry, Saarland University, Am Markt Zeile 3, 66125 Saarbrücken, Germany. E-mail: guido.kickelbick@uni-saarland.de

Inorganic Solid State Chemistry, Saarland University, Am Markt Zeile 3, 66125, Saarbrücken, Germany

EXPERIMENTAL

Materials

Tetraethyl orthosilicate was provided by Wacker Silicones (Burghausen, Germany). Isobutyl methyl ketone (IBMK), dry toluene, dry dichloromethane, furan, methacryloyl chloride, 2-bromopropionyl bromide, 10-undec-1-ol, furfuryl alcohol, Karstedt catalyst, ethyl 2-bromoisobutyrate, N,N,N′,N′,N′′-pentamethyldiethylenetriamine (PMDETA) and 1,1,4,7,10,10-hexamethyltriethylenetetramine (HMTETA) were purchased from Sigma-Aldrich (Steinheim, Germany). Dimethylethoxysilane was purchased from ABCR (Karlsruhe, Germany). Triethylamine was purchased from Acros Organics (Geel, Belgium). All chemicals were used as received or purified applying standard procedures.

Methods

Fourier transform infrared (FTIR) spectroscopy measurements were performed on a Bruker Vertex 70 spectrometer under ambient air (40 scans at a resolution of 4 cm^{-1}) in attenuated total reflectance mode. TGA was performed on a Netzsch Iris TG 209 C in an alumina crucible heating from room temperature to 700 °C under nitrogen followed by heating to 800 °C under oxygen with a rate of 5 °C min^{-1}. DSC measurements were carried out on a Netzsch DSC 204 F1 Phoenix calorimeter in aluminium crucibles with pierced lids, heating under nitrogen with a rate of 15 °C min^{-1}. Liquid state NMR spectra were recorded on a Bruker AC 200 F spectrometer (^{1}H at 200.13 MHz, ^{13}C at 50.32 MHz). Liquid state ^{29}Si NMR spectra were recorded on a Bruker Avance 300 spectrometer at 59.63 MHz. Transmission electron microscopy (TEM) was carried out using a JEOL JEM-2010 microscope. The samples were attached to Plano S160-3 copper grids by dispersing them in ethanol using an ultrasound cleaning bath, adding one drop (30 μL) on the copper grid and evaporating the solvent. Dynamic light scattering (DLS) measurements were carried out by non-invasive backscattering on an ALV/CGS-3 compact goniometer system with an ALV/LSE-5003 correlator at a wavelength of 632.8 nm (He − Ne laser) and a 90° goniometer angle. The dispersing media were purified before use with a syringe filter (200 nm mesh). The determination of the particle radius was carried out by analysis of the correlation function via the $g2(t)$ method followed by a linearized number-weighting of the distribution function. Nitrogen sorption measurements were performed at 77 K on a Sorptomatic 1900 instrument from Fisons Instruments. The samples were degassed under vacuum at 60 °C for at least 2 h prior to measurement. The surface area was calculated according to the Brunauer, Emmett and Teller (BET) method.

Microscope images were recorded under polarized light using an Olympus BX60 microscope equipped with a Sony CCD-Iris color camera. The polymer films were obtained by drop-casting a 10 mg mL^{-1} dispersion onto glass slides. Scratches were created with a diamond scratching pen.

Rheological measurements of the polymer melts were carried on an Anton Paar Physica MCR 301 rheometer equipped with a CTD 450 convection oven. The prepressed samples were measured in oscillation mode using the PP25 measuring system with 25 mm plate diameter and a plate-to-plate distance of 1 mm. UV − visible spectra were recorded on a Perkin Elmer Lambda 25 UV − visible spectrometer in transmission mode on 1 mm quartz slides. The samples were prepared by dip coating. SEC measurements in tetrahydrofuran (THF) were performed with a PSS system, which included a Viscotek VE1121 pump, a Shodex refractive index detector, a PSS SLD 7000 multi-angel light scattering detector and styrene-divinylbenzene copolymer columns (PSS SDV) at a rate of 1 mL min^{-1}.

Synthesis of the protected maleimide monomer pMiMA – 3-(3,5-dioxo-10-oxa-4-azatricyclo[5.2.1.0^{2,6}]dec-8-en-4-yl)-propyl 2-methylprop-2-enoate (3)

A 500 mL three-necked round-bottom flask equipped with a dropping funnel was charged with 25 g (0.112 mol) protected (3-hydroxypropyl)maleimide (2), 200 mL dry dichloromethane and 13.6 g (0.134 mol) triethylamine under an argon atmosphere. The solution was stirred at 0 °C for 10 min and then, maintaining the same temperature, 12.29 g (0.118 mol) methacryloyl chloride was added dropwise. The reaction mixture was stirred overnight at room temperature. Then 600 mL dichloromethane was added and the solution was washed twice with 50 mL of saturated NaHCO$_3$ solution and twice with water. After drying with sodium sulfate the organic layer was concentrated under vacuum and the crude product was purified by flash chromatography (ethyl acetate/CH$_2$Cl$_2$ 1:1). Yield: 25.6 g (0.087 mol; 78.5%).

^{1}H NMR (CDCl$_3$, 25 °C) δ ppm: 1.91 (s, 3H), 2.01 (s, 2H), 2.87 (s, 2H), 3.82 (t, $J = 6.00$ Hz, 2H), 4.29 (t, $J = 6.00$ Hz, 2H), 5.27 (s, 2H), 5.56 (s, 1H), 6.08 (s, 2H), 6.52 (s, 2H). ^{13}C NMR (CDCl$_3$, 25 °C) δ ppm: 18.23 (CH$_3$), 26.70 (CH$_2$), 35.76 (CH$_2$ − N), 47.37 (CH), 61.51 (CH$_2$ − O), 80.92 (CHO), 114.06 (C = C), 125.52 (=CH$_2$), 136.49 (=C<), 167.18 (O − C = O), 176.06 (N − C = O). IR (cm^{-1}): 3450 (sym C = O + asym C = O), 3087 (=C − H), 3015 (=C − H), 2967 (C − H), 2930 (C − H), 1777 (sym C = O), 1693 (asym C = O), 1401, 1317, 1173, 875. Elemental analysis (%): calculated for C$_{15}$H$_{17}$O$_5$N, C 61.85, H 5.88, N 4.81; found C 60.61, H 6.09, N 4.61.

Synthesis of furfuryl methacrylate (4)

The reaction was carried out under an argon atmosphere. In a 1 L round-bottom flask, 37.53 g (0.383 mol) furfuryl alcohol, 160 mL dry dichloromethane and 58.08 g (0.574 mol) triethylamine were mixed while stirring vigorously for 10 min in an ice-water bath. Afterwards 40.0 g (0.2826 mol) methacryloyl chloride was added dropwise at 0 °C. After the addition, the reaction mixture was stirred at room temperature overnight. The white triethylammonium chloride was removed by filtration and the yellow turbid solution was concentrated under vacuum. Finally, the crude product was purified by distillation under vacuum (70 °C at 4 mbar). Yield: 36.53 g (0.219 mol; 57.5%).

^{1}H NMR (CDCl$_3$, 25 °C) δ ppm: 1.91 (s, 3H), 5.11 (s, 2H), 5.53 (s, 1H), 6.10 (s, 1H), 6.31 − 6.40 (m, 2H), 7.38 (s, 1H). ^{13}C NMR (CDCl$_3$, 25 °C) δ ppm: 18.01 (CH$_3$), 58.04 (CH$_2$ − O), 110.33 (=CH − CH=), 125.68 (=CH$_2$), 135.89 (=C<), 142.97 (=CH − O), 149.51 (=C − O), 166.71 (C = O). IR (cm^{-1}): 3124 (=C − H), 2959 (C − H), 1716 (C = O), 1314, 1292, 1153, 1144, 1010, 918, 813, 742. Elemental analysis (%): calculated for C$_9$H$_{10}$O$_3$, C 65.05, H 6.07, N 0.00; found C 63.49, H 5.96, N 0.00.

Poly[(butyl methacrylate)-co-(protected maleimidopropyl methacrylate)] – P(BMA-co-pMiMA)

In a typical experiment, HMTETA (0.02 eq) and freshly prepared CuBr (0.02 eq) were added to a solution of butyl methacrylate (1 eq) and the comonomer pMiMA (0.1 eq) in dry toluene (four times the volume of monomers) in a 100 mL Schlenk tube. Afterwards, the mixture was degassed by three freeze − pump − thaw cycles. The polymerization was started by adding ethyl α-bromoisobutyrate (0.01 eq) and was carried out at 70 °C. After 3 h opening of the

Schlenk tube to the atmosphere stopped the reaction. The reaction mixture was diluted with THF and the catalyst was removed over activated alumina. After solvent removal the polymer was precipitated from acetone with methanol while cooling in liquid nitrogen. Yield: 36%; degree of substitution (DS) 0.1 (NMR).

^{1}H NMR (CDCl$_3$, 25 °C) δ ppm: 0.95 (m, 71H), 1.26 − 1.91 (m, 78H), 2.87 (bs, 2H), 3.58 (m, 2H), 3.94 (bs, 28H), 5.27 (s, 2H), 6.53 (s, 2H). ^{13}C NMR (CDCl$_3$, 25 °C) δ ppm: 13.68, 19.31, 29.26, 30.20, 30.87, 44.74, 47.42, 53.83, 64.70, 80.95 (CHO), 136.55 (C = C), 175.93 (N − C = O), 177.50 (C = O), 177.83 (C = O). SEC (THF, LS): $M_n = 33\,000$ g mol^{-1}; polydispersity index (PDI) = 1.22. IR (cm^{-1}): 2957 (C − H), 2873 (C − H), 1721 (C = O), 1703 (C = O mal), 1447, 1400, 1264, 1239, 1144, 1063, 878, 748.

Synthesis of monoethoxysilane initiator[21]
Synthesis of undec-10-en-1-yl 2-bromopropanoate
In a 250 mL three-necked round-bottom flask, a solution of 10.00 g (0.0587 mol) 10-undec-1-ol and 5.97 g (0.0590 mol) triethylamine in 100 mL dichloromethane was stirred at 0 °C for 10 min. 12.95 g (0.06 mol) 2-bromopropionyl bromide was added dropwise at 0 °C and the mixture was stirred overnight at room temperature. The organic phase was washed three times with 40 mL of a saturated NaHCO$_3$ solution and three times with water. The organic layer was dried over sodium sulfate and concentrated under vacuum. Yield: quantitative.

^{1}H NMR (CDCl$_3$, 25 °C) δ ppm: 1.31 (m, 12H), 1.67 (m, 2H), 1.85 (d, $J = 8$ Hz, 3H), 2.06 (m, 2H), 4.17 (t, $J = 6$ Hz, 2H), 4.39 (q, $J = 6$ Hz, 1H), 4.96 (t, $J = 10$ Hz, 2H), 5.84 (m, 1H). ^{13}C NMR (CDCl$_3$, 25 °C) δ ppm: 21.30 (**C**H$_3$ − CHBr), 25.45 (CH$_2$), 28.10 (CH$_2$), 28.63 (CH$_2$), 28.79 (CH$_2$), 29.08 (CH$_2$), 29.14 (CH$_2$), 32.43 (CH$_2$), 33.51 (CH$_2$), 39.77 (CHBr), 65.69 (CH$_2$ − O), 113.82 (C = C), 138.69 (C = C), 169.95 (C = O). IR (cm^{-1}): 3077 (=C − H), 2976 (C − H), 2924 (C − H), 2854 (C − H), 1739 (C = O), 1640 (C = C), 1058, 992, 908.

Synthesis of 10-dimethylethoxysilyl-undec-1-yl 2-bromopropanoate
In a 1 L round-bottom flask with reflux condenser and drying tube, 30.1 g (0.099 mol) undec-10-en-1-yl 2-bromopropanoate was dissolved in 100 mL of dichloromethane. 10.28 g (0.099 mol) dimethylethoxysilane was added and the mixture was heated to 50 °C. Karstedt catalyst (100 μL) was added and the reaction was allowed to stir under dry air for 3 days at 50 °C. NMR of the reaction mixture showed complete conversion. The catalyst was removed by passing the solution over 2 g of alumina. The solvent was removed under vacuum and colorless oil was used without further purification. Yield: 37 g (0.090 mol; 91.5%).

^{1}H NMR (200 MHz, CDCl$_3$) δ ppm: 0.07 (s, 6H), 0.54 (m, 2H), 1.26 (m, 20H), 1.62 (m, 3H), 1.81 (d, $J = 8$ Hz, 3H), 3.70 (m, 2H), 4.15 (m, 2H), 4.35 (q, $J = 6$ Hz, 1H). ^{13}C NMR (CDCl$_3$, 25 °C) δ ppm: −2.12 (**C**H$_3$ − Si), 16.35 (CH$_2$ − Si), 18.51 (SiOCH$_2$ − **C**H$_3$), 21.62 (**C**H$_3$ − CHBr), 23.13 (CH$_2$), 25.69 (CH$_2$), 28.34 (CH$_2$), 29.11 (CH$_2$), 29.26 (CH$_2$), 29.45 (CH$_2$), 33.37 (CH$_2$), 40.14 (CHBr), 58.09 (Si − O − CH$_2$−), 66.00 (CH$_2$ − O), 170.17 (C = O). ^{29}Si NMR (CDCl$_3$, 25 °C) δ ppm 16.82. IR (cm^{-1}): 2924 (C − H), 2854 (C − H), 1739 (C = O), 1446 (C − H), 1389 (C − H), 1250 (C − H), 1158, 1106, 1074, 837, 783, 722, 679.

Surface modification with ATRP initiator[21]
In a 250 mL round-bottom flask mounted with a reflux condenser, 10 g of silica particles, prepared by a modified Stöber synthesis,[21,36] were dispersed in 150 mL IBMK using ultra

sonication. 20 g of the ATRP initiator 10-dimethylethoxysilyl-undec-1-yl 2-bromopropanoate was added and the mixture was stirred at 115 °C for 24 h. After cooling, the particles were collected by centrifugation at 13 000 rpm for 20 min, washed three times with acetone and dried under vacuum (residual pressure *ca* 0.01 mbar). Yield: 6.72 g.

Grafting-from polymerization of poly[(butyl methacrylate)-*co*-(furfuryl methacrylate)] – P(BMA-*co*-FMA)@SiO$_2$ [21]
1 g initiator functionalized nanoparticles, 15 g (0.105 mol) BMA, 1.75 g (105 mmol) FMA, 300 mg (1.3 mmol) HMTETA and 20 mL toluene were placed in a Schlenk tube. The flask was sealed and the contents were degassed by three freeze − pump − thaw cycles. The Schlenk tube was charged with argon and 140 mg (1 mmol) CuBr was subsequently added. The reaction occured for 6 h at 70 °C and was quenched by exposing it to air. The sample was centrifuged at 13 000 rpm for 20 min and resuspended in acetone to wash out free polymer and excess monomer. Yields: 4 g.

Etching of silica particles for SEC of graft polymer
In order to characterize the polymer chains grafted from the silica nanoparticles, they have to be detached from the surface. Therefore, prior to gel permeation chromatography analysis, the silica nanoparticles were dissolved with hydrofluoric acid (HF) to obtain free PBMA-*co*-FMA polymer. The etching procedure consisted in adding 250 mg of the PBMA-*co*-FMA@silica particles to a plastic vial, followed by 10 mL toluene, 75 mg phase transfer catalyst Aliquot 336 and 15 mL of a 2% aqueous solution of HF. The vial was sealed and the content was stirred vigorously for several hours. At the end of the etching process, the aqueous and organic phases were allowed to separate and the organic phase was removed from the top. After washing the latter with a saturated sodium bicarbonate solution to neutralize residual HF, the solvent was removed in order to precipitate the polymer from acetone into cold methanol. Yield: 100 mg.

^{1}H NMR (THF-d$_8$, 25 °C) δ ppm: 0.87 (m, 76H), 1.30 − 1.82 (m, 87H), 3.83 (bs, 25H), 4.86 (s, 2H), 6.26 − 6.33 (m, 2H), 7.40 (s, 1H). ^{13}C NMR (CDCl$_3$, 25 °C) δ ppm: 16.48, 18.71, 44.53, 44.87, 51.72, 54.17, 58.30, 110.45 (C = C), 143.19 (C = C), 148.86 (C = C), 176.91 (C = O), 177.73 (C = O). SEC (THF, LS): $M_n = 150\,000$ g mol^{-1}; PDI = 3.3. IR (cm^{-1}): 2958 (C − H), 2934 (C − H), 2874 (C − H), 1722 (C = O), 1464, 1239, 1143, 1063, 964, 945, 747.

RESULTS AND DISCUSSION
Initiator synthesis and surface modification
The synthesis of the ATRP initiator attachable to the silica nanoparticles was carried out according to a modified literature procedure.[21] Esterification of 10-undecen-1-ol with 2-bromopropyonyl bromide was followed by hydrosilation with dimethylethoxysilane to yield a coupling agent capable of forming monolayers on the silica nanoparticles. The latent α-halo ester was later used to initiate the ATRP of methacrylic monomers. Formation of an initiator monolayer on silica nanoparticles was performed using the technique described by Green *et al.*[21,35] SiO$_2$ particles (Fig. S1) with a diameter of 42.1 ± 5.4 nm prepared by a modified Stöber process[36] were suspended in IBMK, a solvent with a relatively high dielectric constant, resulting in ionized silanol groups and thereby stabilizing the suspension. The initiator was added to the boiling solution with an initiator to surface site ratio
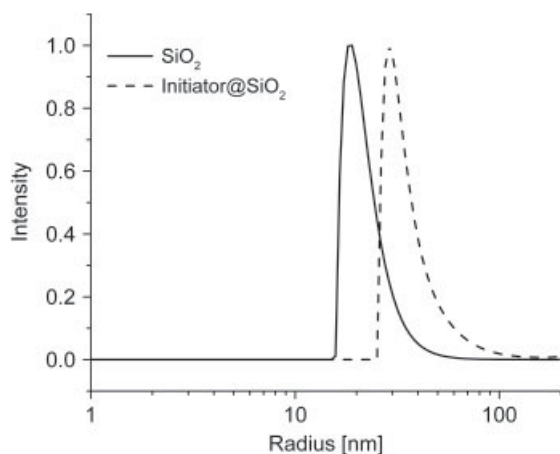
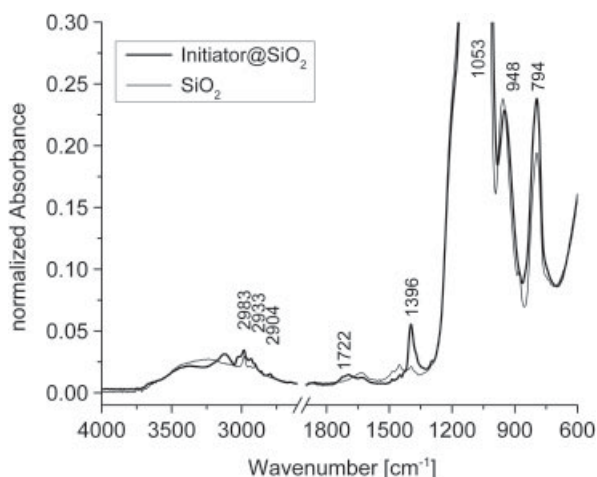**Figure 1.** DLS hydrodynamic radii of bare silica and initiator modified particles in ethanol.

Figure 2. FTIR spectra of bare silica and initiator@SiO$_2$.

[I]/[S] of 2, where [I] is the initiator concentration and [S] is the number of hydroxyl groups on the silica surface. The number of surface silanols was assumed to be 5 OH groups per nm^2.[21]

Figure 1 displays the DLS size distributions of bare silica and the initiator modified particles in ethanol. An increase of the hydrodynamic diameter from 43.8 ± 6.6 nm to 74.0 ± 9.1 nm was observed after the modification step. The radius of the pristine silica particles is consistent with TEM images. Measurements of 500 particles revealed a diameter of 42.1 ± 5.4 nm (Fig. S1).

The success of functionalization was also studied by FTIR spectroscopy (Fig. 2). The original silica particles showed multiple peaks in the 'fingerprint' region: a strong asymmetric Si–O–Si vibration at 1100 cm^{-1}, a weaker symmetric Si–O–Si vibration at 797 cm^{-1} and an asymmetric Si–OH vibration at 957 cm^{-1}.[35] Furthermore, the presence of molecular water was detected through scissor bending vibration at 1630 cm^{-1}. The broad signal from 3700 to 3300 cm^{-1} originates from a superposition of H-bonded molecular water and surface silanols. CH$_2$ and CH$_3$ vibrational modes (3000–2900 cm^{-1}) and bending modes (1500–1400 cm^{-1}) could be assigned to remaining ethoxy groups on the surface of the silica particles.

The FTIR spectrum of initiator modified particles (initiator@SiO$_2$) showed a decrease of OH vibrations and an increase of the CH$_2$ and

CH$_3$ vibrational and bending modes (Fig. 2). Furthermore, a broad carbonyl signal was observed at 1722 cm^{-1}. TGA revealed a mass loss of 22.1%. In a nitrogen atmosphere the initiator molecules decompose above 200 °C in two steps. This result was confirmed by elemental analysis, presenting 11.2% carbon and 2.5% hydrogen. The remaining 8% were assigned to the presence of oxygen and bromine.

The initiator graft density σ_1 was determined using the following equation

$$\sigma_1 = \frac{m\%}{A_{Silica}} \frac{N_A}{MW} 0,01 \tag{1}$$

where N_A is the Avogadro number, A_{silica} is the surface area of the silica particles in m^2 g^{-1}, $m\%$ is the mass loss from TGA assigned to the initiator and MW is the molecular weight of the initiator in g mol^{-1}, by taking into account that the anchoring Si — O bond of the surface immobilized coupling agent is not cleaved during heating. The surface area of the bare silica was determined using the BET method.[37]

This calculation yields a graft density σ_1 of 1.3 initiator molecules per square nanometer. The number of initiator groups per surface area is comparable to the value achieved by Green et al.[21] Higher graft densities were not realized because high excess of coupling agent results in high loss of unreacted initiator.
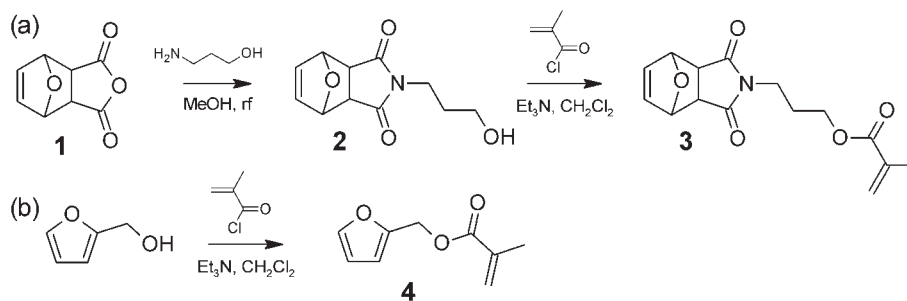
Monomer synthesis

The maleimide methacrylic ester was synthesized according to a modified literature procedure.[38] In order to avoid radical polymerization at the maleimide double bond or any electrophilic attack through Michael addition, it is preferable to protect maleic anhydride with furan by a DA reaction in toluene at room temperature. The resulting double bond of the 10-oxa-4-azatricyclo[5.2.1.0^{2,6}]dec-8-ene-3,5-dione (Scheme 1(a)) shows very low reactivity compared with the conjugated maleimide double bond. A longer reaction time of 3 days allowed the yield of the protection by the DA reaction to be increased to 89%. The imidization reaction between 3-aminopropan-1-ol and the protected anhydride was carried out in methanol. In the last step the protected 3-hydroxypropylmaleimide was reacted with methacryloyl chloride to form the maleimide-containing monomer as a waxy slightly yellow solid (Scheme 1(a)).

Furfuryl methacrylate was synthesized using the commercially available furfuryl alcohol and methacryloyl chloride. Purification by distillation is necessary and the colorless liquid product was obtained in 57.5% yield (Scheme 1(b)).

ATRP of P(BMA-*co*-pMiMA)

The copolymerization of butyl methacrylate with protected maleimidopropyl methacrylate in a 10:1 ratio by ATRP using PMDETA resulted either in a highly crosslinked product or in no polymerization at all, depending on the amount of solvent used in the reaction. The relatively high reaction temperature of 90 °C shifted the DA equilibrium towards the rDA reaction leading to partially deprotected maleimides by liberation of furan. The resulting highly reactive double bond reacted readily under radical conditions to form a crosslinked polymer (Scheme 2). In order to avoid deprotection of maleimido double bonds at 90 °C, the reaction temperature had to be decreased which resulted in a change of the copper complex applied. Using HMTETA as the chelating agent, the reaction could be carried out at 70 °C, at which temperature no rDA occurred and only the methacrylic

Scheme 1. Monomer synthesis.
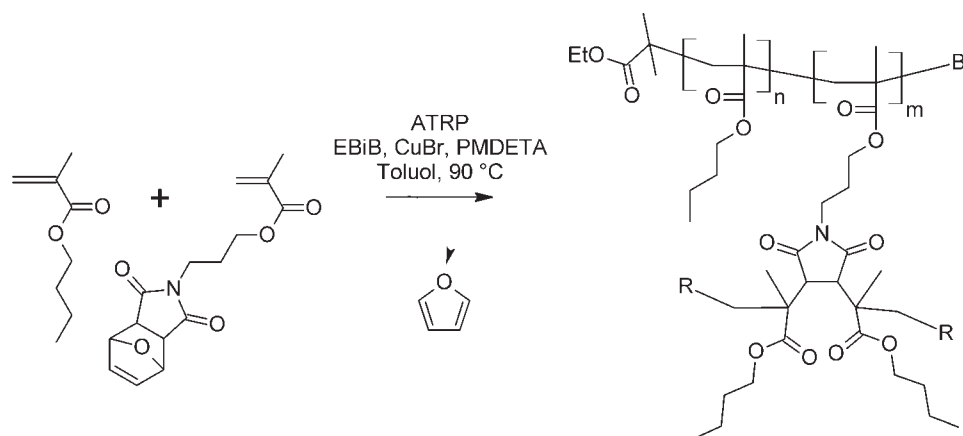
Scheme 2. Schematic representation of undesired branching/gelation after deprotection of maleimide moieties.

double bonds were polymerized. Furthermore, the reaction time was decreased to 3 h in order to prevent side reactions.

These optimized reaction conditions allowed the synthesis of a linear, non-crosslinked copolymer of BMA and pMiMA. The maleimido monomer showed a slightly lower reactivity yielding a DS of 0.09. ^{1}H NMR spectroscopy of the P(BMA-co-pMiMA) revealed a signal at 6.52 ppm, which can be assigned to the double bond in the protected maleimide group (Fig. 3(a)). The signals at 5.26 and 2.86 ppm were assigned to the other protons of the protection group. The second ^{1}H NMR spectrum (Fig. 3(b)) was recorded after deprotection of the maleimide moieties within the polymer. Deprotection was achieved by heating the sample to 140 °C for 1 h and could be proved by NMR through disappearance of all the signals assigned to the protection group. Furan was released by rDA reaction during heating, giving rise to a maleimide signal at 6.71 ppm.

DSC of the same sample before deprotection showed a strong endothermic signal at 154 °C with an onset temperature of 124 °C, originating from the rDA reaction followed by endothermic evaporation of the released furan (Fig. 4). The second heating cycle permitted the glass transition temperature T_g of the copolymer P(BMA-co-MiMA) to be determined as 28 °C.

FTIR spectroscopy was also used to detect the rDA deprotection reaction. After the heat treatment, furan was released by the rDA reaction resulting in the appearance of a signal at 696 cm^{-1}, which arises from a maleimide ring deformation (Fig. 5, inset). Aside from this maleimide signal, the deprotection could be detected by the blueshift of the maleimide carbonyl signal from 1696 cm^{-1} to higher wavenumbers. The protected sample showed two distinct carbonyl signals, for the maleimide ring and the methacrylic esters. After the rDA reaction the two signals merged together.
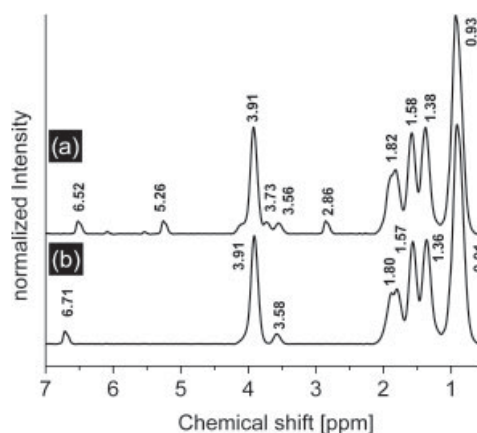
Figure 3. ^{1}H NMR spectrum of P(BMA-co-pMiMA) before (a) and after (b) deprotection by rDA reaction.

P(BMA-co-FMA)@SiO$_2$ by grafting-from ATRP

Silica − polymer core − shell particles with pendant furfuryl groups were prepared via surface-initiated ATRP as counterpart for the linear maleimido copolymer. In order to increase the distance between the particle surface and the functional groups as well as the number of reacting groups, grafting-from polymerization of a copolymer containing reactive moieties was envisioned.

Atom transfer radical grafting-from polymerization in toluene with PMDETA as chelating agent was used for the preparation of the particles. This procedure did not change the size distribution and the resulting particles also revealed no strong tendency to agglomerate in TEM (Fig. S2). However, the composite particles dispersed in THF revealed an increase of the hydrodynamic
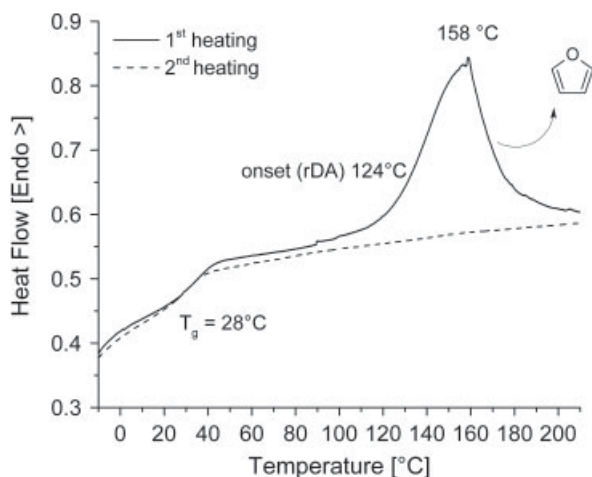
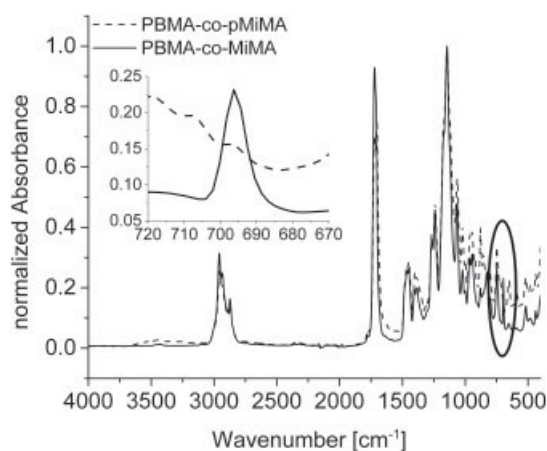**Figure 4.** DSC curves of the first two heating cycles of P(BMA-*co*-pMiMA) (15 °C min^{-1}).

Figure 5. FTIR spectra of P(BMA-*co*-pMiMA) before and after deprotection via rDA reaction at 140 °C.
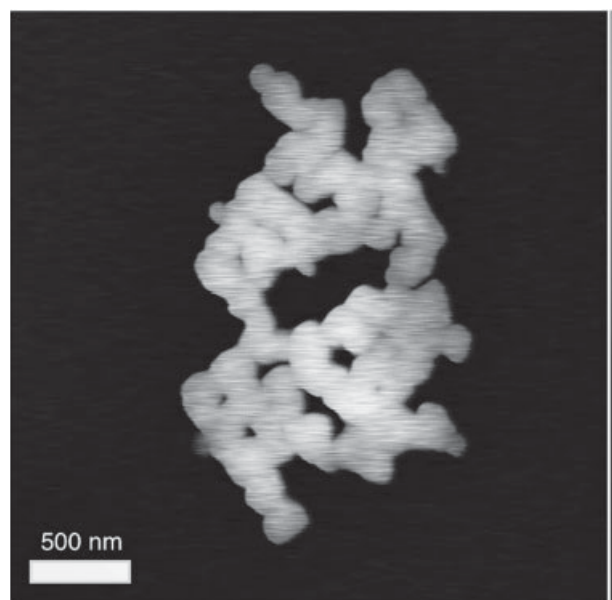

Figure 6. AFM image of core − shell particles.
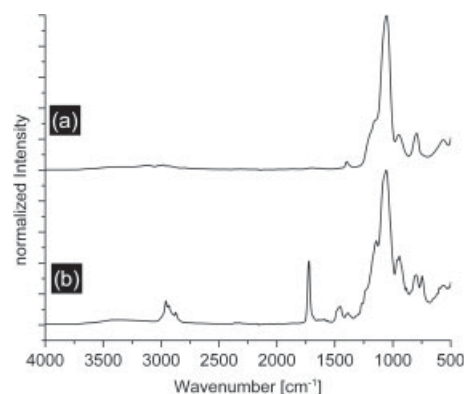
Figure 7. FTIR spectra of (a) initiator modified particles and (b) polymer core − shell particles.

diameter of roughly 200% compared with the bare silica particles, as demonstrated by DLS (Fig. S3). The diameter of 132.0 ± 19.9 nm results from a polymeric layer surrounding the silica particles with approximately the same thickness as the core itself. As TEM was not appropriate to visualize the polymeric shell, AFM analysis (Fig. 6) of the core − shell particles was performed after spin coating from suspension on mica slides. AFM showed strongly agglomerated particles with an approximate height of 80 nm and a mean width of 216 ± 34 nm.

ATR-IR spectra (Fig. 7) allowed a comparison of initiator modified particles and copolymer modified particles. In the spectrum of P(BMA-*co*-FMA)@SiO$_2$, a strong carbonyl stretching signal at 1724 cm^{-1} was observed which originates from the carbonyls in the methacrylate chains.

TGA measurements of the core − shell particles showed a first decomposition step below 200 °C, originating from trapped solvent or monomer molecules (Fig. 8). The polymer chains begin to decompose at 250 °C. During two decomposition steps the sample lost 91% of its original mass. Thereby, 68.9% of the original mass is assigned to the grafted copolymer.

In order to determine the molecular weight and the polydispersity of the graft polymer chains, the silica core had to be etched with hydrofluoric acid. SEC of the liberated copolymer resulted in a molecular weight M_n of 150 000 g mol^{-1} and a PDI of 3.3. ^{1}H NMR of the previously grafted polymer provided a DS of 0.11 furfuryl groups.

The calculation of the graft density using Eqn 1 for the copolymer with a molecular weight of 150 000 g mol^{-1} indicated 0.01 polymer chains per square nanometer.

The relatively low graft density compared with the results of Green *et al.*, who prepared poly(methyl methacrylate) grafted particles with 0.18 polymer chains per square nanometer,[21] can be explained by the lower reactivity of BMA as well as steric effects caused by bulkier monomers. The higher PDI compared with the surface polymerization of methyl methacrylate (2.2)[34] is attributed to the high molecular weight of the chains and because copolymerization tends to increase the PDI through differences in reactivity between the monomers.

Diels − Alder curing and proof of self-healing ability

DA curing was conducted on a small scale. Thus the linear P(BMA-*co*-MiMA) was mixed with a suspension of P(BMA-*co*-FMA)@SiO$_2$ in THF and the solvent was removed. Afterwards, the as-prepared nanocomposite was heated to 80 °C for 24 h in order to allow
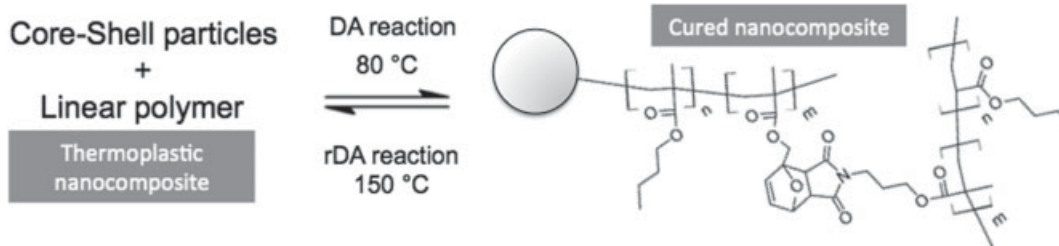
Scheme 3. Schematic representation of the self-healing mechanism.

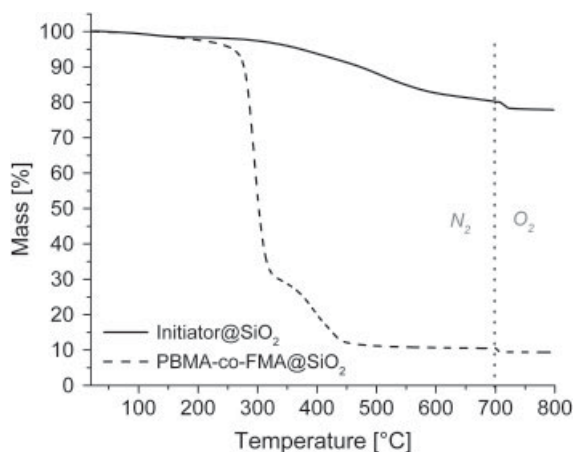**Figure 8.** TGA measurements of initiator modified particles and core — shell particles.

Figure 9. DSC curves of crosslinked PBMA-*co*-MiMA and PBMA-*co*-FMA@SiO₂.

curing by the DA reaction. Scheme 3 shows the curing principle of the self-healing material.

During the first heating cycle of DSC measurements, the cured sample showed a broad endothermic rDA signal above 115 °C, with an enthalpy of reaction of 5.3 J g^{-1} (Fig. 9). During cooling no DA reaction could be observed because the curing reaction is too slow and does not give rise to a detectable signal at a cooling rate of 15 °C min^{-1}. During the second heating cycle, only a very small endothermic peak with an enthalpy of reaction of 1.3 J g^{-1} could be detected at 150 °C, meaning that curing only took place to a small extent during cooling. Furthermore, curing increased the glass transition temperature to 39 °C.

Melt rheology was used to illustrate the increase of the storage modulus during curing of the nanocomposite by DA reaction. Therefore a 1:1 mixture of P(BMA-*co*-MiMA) and P(BMA-*co*-FMA)@SiO₂ was pressed into a disc with a diameter of 25 mm and a thickness of 1 mm. Then the storage modulus of the sample disc was measured in oscillation mode at 80 °C over several hours. Figure 10 shows the evolution of the storage modulus. At first, starting at 0.25 MPa, a rapid increase was observed during the first 4 h. At the end of the experiment the curing rate decreases, yielding a maximum storage modulus of slightly above 0.46 MPa. In order to decrease the curing time from 24 h or several days to an acceptable period for self-healing applications, a curing degree of 80% was chosen as a target. This percentage was calculated by normalizing both time and storage modulus and taking the first derivative of the curve. At a curing degree of 80%, the curing rate drastically decreases and at this point the first derivative of the normalized curve is equal to 1.

The free maleimide moiety has a UV light absorption maximum at approximately 300 nm. A thin film of the nanocomposite
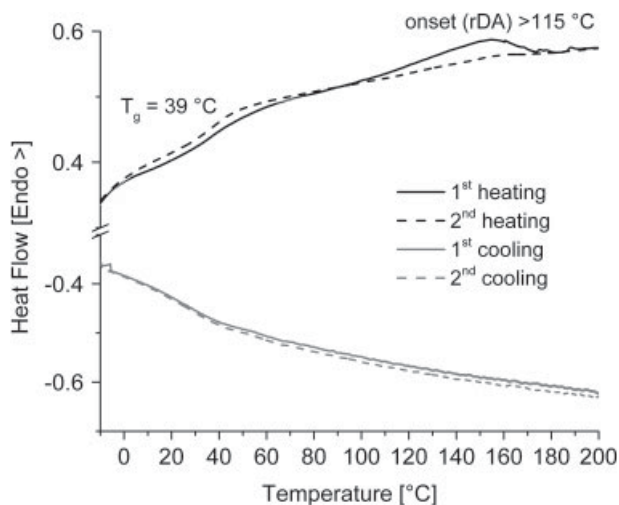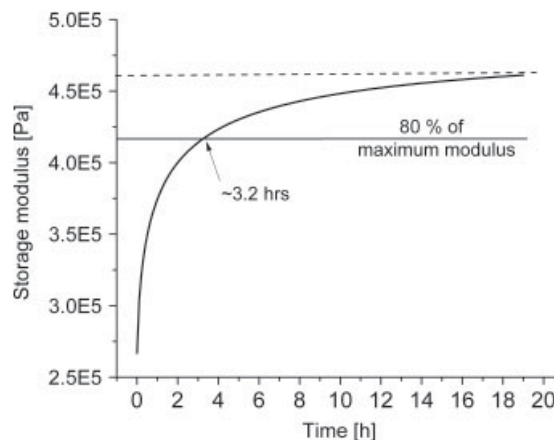

Figure 10. Storage modulus over time measured by melt rheology; 80% of the maximum storage modulus was reached after approximately 3.2 h.

material was dip coated onto a quartz substrate and the evolution of the maleimide UV absorption was followed over time. This gave rise to a conversion over time plot very similar to the rheological measurements (Fig. 11). At the beginning of the experiment, the maleimide absorption dropped rapidly and the conversion rate decreased drastically after 4 h. Similar to the rheological data, 80% of the maximum curing was achieved after approximately 3.2 h.

The greatest advantage of self-healing materials using thermoreversible reactions as a healing mechanism over capsule based healing is the idealized endless repeatability of the healing
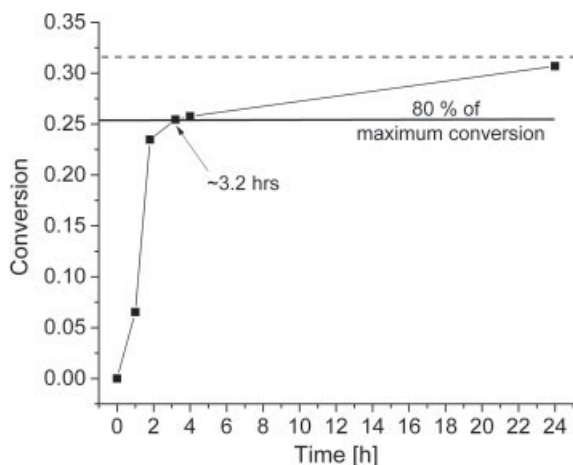
Figure 11. Conversion over time of the curing reaction measured by UV−visible spectroscopy; 80% of maximum conversion is reached after approximately 3.2 h.
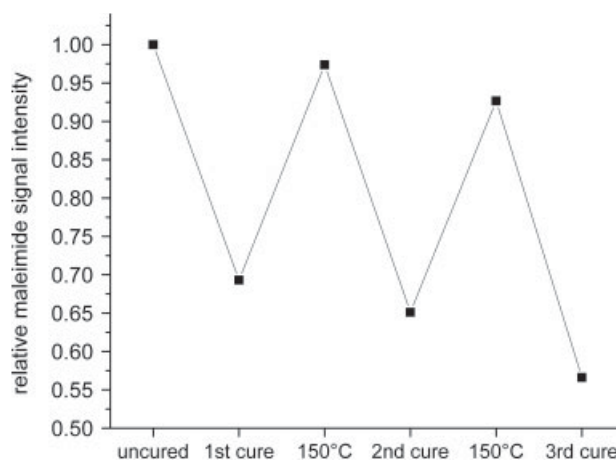

Figure 12. Relative maleimide UV signal over multiple DA curing/rDA cycles.

mechanism. There are no reservoirs with liquid curing agents that deplete after one or two healing cycles. Nevertheless, the high temperatures during the rDA reaction may result in thermal decomposition of functional groups. Even photochemical irreversible 2 + 2 cycloadditions between maleimides could cause a decrease of healing capacities. Therefore it is important to test the curing and de-curing over multiple cycles, to show that the healing process is not limited to just a few cycles.

UV − visible spectroscopy was used to investigate the curing efficiency over multiple DA/rDA cycles. Figure 12 shows the relative maleimide signal intensity over three DA/rDA cycles. The study reveals that the healing efficiency does not decrease over the first three cycles, but a systematic decrease in maleimide signal strength in both the cured and de-crosslinked state was observed. This can be explained by a change in film thickness over time

by flow of the de-crosslinked system at high temperatures. If this decrease were caused by irreversible maleimide crosslinks, only the signal in the de-crosslinked state would decrease over time.

Scratch-healing tests were performed on drop cast composite films using an optical microscope with polarization filter. After curing of the nanocomposite films, a diamond scratching pen was used to produce scratches on the film surface. Figure 13 shows such a scratch magnified 200 times. The section of the scratch visible in the first picture is approximately 1 mm long and 80 μm wide. First the self-healing film was treated at 80 °C for 1 h, leading to a smoothing of the scratch profile. The deep region of the scratch, produced by the sharp tip of the diamond cutter, did not disappear. The less deep regions of the scratch were only plastic displacement of material caused by etches of the cutting tool. Here the polymer chains were intact and did not have to heal. The
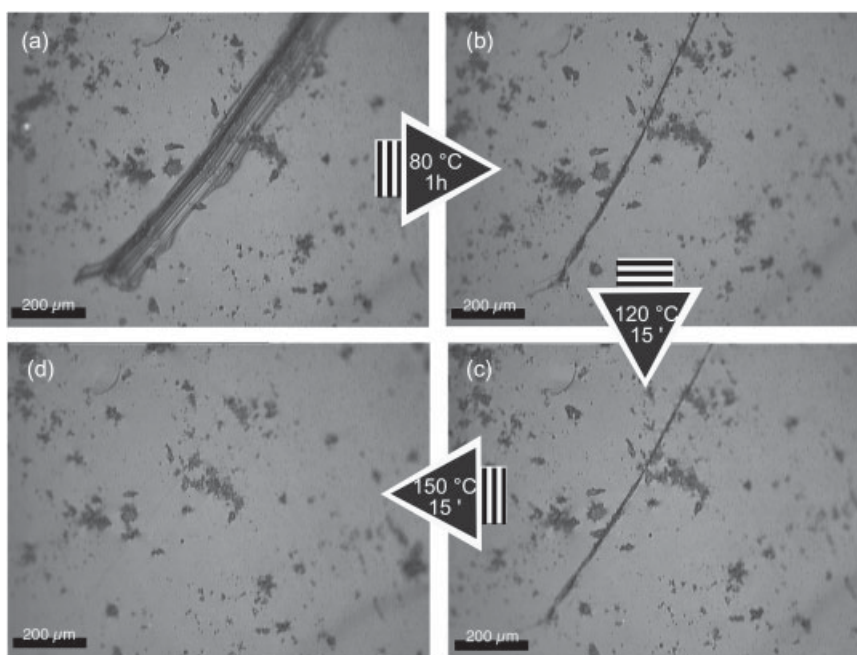

Figure 13. Microscope images of a scratch in a nanocomposite film on glass (a) before healing, (b) after heating for 1 h to 80 °C, (c) after heating for 15 min at 120 °C and (d) after healing for 15 min at 150 °C.

material only becomes smoother by evening out the produced roughness.

The actual cut in the film surface is only 10–20 µm wide and could not heal at 80 °C because the polymer chains were unable to cross the scratch interface in the cured state. A second heating step at 120 °C was chosen to prove that no healing occurred at high temperatures without rDA reaction. At a temperature of 120 °C, the material is at its maximum mobility but it stays crosslinked. Figure 13(c) shows that the scratch morphology did not change after heating to 120 °C for 15 min. Finally, the healing step at 150 °C (Fig. 13(d)) closed the scratch interface along the entire length. This proves that the rDA reaction took place very quickly, breaking up the network and enabling flow of polymer chains across the scratch. Because the material glass transition temperature is only slightly above room temperature, the macromolecules are very mobile at 150 °C and can quickly re-entangle and close the scratch.

SUMMARY

An intrinsically self-healing nanocomposite was synthesized using DA and rDA reactions as the healing mechanisms. Linear butyl methacrylate based copolymer bearing propylmaleimide side groups was synthesized by ATRP. Deprotection of the maleimide functional group by rDA reaction could be observed by DSC, NMR and IR spectroscopy. The counterparts for DA curing, silica − polymer core − shell particles, were prepared using surface-initiated ATRP with furfuryl methacrylate and butyl methacrylate as comonomers. A graft density of 0.01 polymer chains per square nanometer was achieved with a molecular weight of 150 000 and a PDI of 3.3.

Mixing the linear polymer with the core − shell particles in suspension and removing the solvent led to a nanocomposite. DA curing was verified using rheological and UV − visible measurements. DSC thermograms of the cured samples showed an endothermic rDA signal at 150 °C. Scratch-healing properties of the composite films on glass surfaces were tested using microscopy. Thermal treatment at temperatures above the rDA temperature broke up the network, allowing thermoplastic flow to close the scratch in the composite film.

ACKNOWLEDGEMENTS

SUPPORTING INFORMATION

Supporting information may be found in the online version of this article.

REFERENCES

1 Greszta D, Mardare D and Matyjaszewski K, *Macromolecules* **27**: 638–644 (1994).
2 Matyjaszewski K, *Macromolecules* **45**: 4015–4039 (2012).
3 Pyun J, Matyjaszewski K, Kowalewski T, Savin D, Patterson G, Kickelbick G, *et al*, *J Am Chem Soc* **123**: 9445–9446 (2001).
4 Ivanovici S, Peterlik H, Feldgitscher C, Puchberger M and Kickelbick G, *Macromolecules* **41**: 1131–1139 (2008).
5 Holzinger D, Liz-Marzan LM and Kickelbick G, *J Nanosci Nanotechnol* **6**: 445–452 (2006).
6 Kickelbick G and Holzinger D, *Polym Prepr* **46**: 442–443 (2005).
7 Holzinger D and Kickelbick G, *J Polym Sci A Polym Chem* **40**: 3858–3872 (2002).
8 Ejaz M, Yamamoto S, Ohno K, Tsujii Y and Fukuda T, *Macromolecules* **31**: 5934–5936 (1998).
9 Retsch M, Walther A, Loos K and Muller AHE, *Langmuir* **24**: 9421–9429 (2008).
10 Prucker O and Ruehe J, *Langmuir* **14**: 6893–6898 (1998).
11 Zhang Z, Morse AJ, Armes SP, Lewis AL, Geoghegan M and Leggett GJ, *Langmuir* **27**: 2514–2521 (2011).
12 Edmondson S, Nguyen NT, Lewis AL and Armes SP, *Langmuir* **26**: 7216–7226 (2010).
13 Matyjaszewski K, Miller PJ, Shukla N, Immaraporn B, Gelman A, Luokala BB, *et al*, *Macromolecules* **32**: 8716–8724 (1999).
14 Caruso F, *Adv Mater* **13**: 11–22 (2001).
15 Shenhar R, Norsten TB and Rotello VM, *Adv Mater* **17**: 657–669 (2005).
16 Bach LG, Islam MR, Jeong YT, Gal YS and Lim KT, *Appl Surf Sci* **258**: 2816–2822 (2012).
17 Liu Y and Cheng Q, *Anal Chem* **84**: 3179–3186 (2012).
18 Strozyk MS, Chanana M, Pastoriza-Santos I, Perez-Juste J and Liz-Marzan LM, *Adv Funct Mater* **22**: 1436–1444 (2012).
19 Holzinger D and Kickelbick G, *Chem Mater* **15**: 4944–4948 (2003).
20 Holzinger D and Kickelbick G, *J Mater Chem* **14**: 2017–2023 (2004).
21 Huang C, Tassone T, Woodberry K, Sunday D and Green DL, *Langmuir* **25**: 13351–13360 (2009).
22 Kickelbick G, Holzinger D, Brick C, Trimmel G and Moons E, *Chem Mater* **14**: 4382–4389 (2002).
23 Zhang J, Jiang L, Pan K, Yi Z and Dan Y, *Polym Int* doi: 10.1002/pi.4514 (2013).
24 Hu F, Neoh KG, Cen L and Kang E-T, *Biomacromolecules* **7**: 809–816 (2006).
25 Yu F, Tang X and Pei M, *Microporous Mesoporous Mater* **173**: 64–69 (2013).
26 Wouters M, Craenmehr E, Tempelaars K, Fischer H, Stroeks N and van Zanten J, *Prog Org Coat* **64**: 156–162 (2009).
27 Wudl F and Chen X, Thermally re-mendable crosslinked polymers, monomers, their manufacture, and thermally mending. Application: US Patent 2002–194332 20040014933 (2004).
28 Chen X, Wudl F, Mal AK, Shen H and Nutt SR, *Macromolecules* **36**: 1802–1807 (2003).
29 Chen X, Dam MA, Ono K, Mal A, Shen H, Nut SR, *et al*, *Science* **295**: 1698–1702 (2002).
30 Engel T and Kickelbick G, Thermally remendable polymers, in *Self-Healing Polymers: From Principles to Applications*, ed. by Binder W. Wiley-VCH, Weinheim, p. 153 (2013).
31 Stevens MP and Jenkins AD, *J Polym Sci Polym Chem Ed* **17**: 3675–3685 (1979).
32 Canary SA and Stevens MP, *J Polym Sci A Polym Chem* **30**: 1755–1760 (1992).
33 Diels O and Alder K, *Justus Liebigs Ann Chem* **460**: 98–122 (1928).
34 Kavitha AA and Singha NK, *Macromol Chem Phys* **208**: 2569–2577 (2007).
35 Engel T and Kickelbick G, *Chem Mater* **25**: 149–157 (2013).
36 Stoeber W, Fink A and Bohn E, *J Colloid Interface Sci* **26**: 62–69 (1968).
37 Brunauer S, Emmett PH and Teller E, *J Am Chem Soc* **60**: 309–319 (1938).
38 Dispinar T, Sanyal R and Sanyal A, *J Polym Sci A Polym Chem* **45**: 4545–4551 (2007).

© 2013 Society of Chemical Industry
wileyonlinelibrary.com/journal/pi

3.3 Furan-Modified Spherosilicates as Building Blocks for Self-Healing Materials

In this work, a nano-sized cage-like spherosilicate was synthesized as building block for the design of self-healing hybrid materials. The octaanion $[^-OSiO_{1,5}]_8$ was reacted with dimethylchlorsilane HMe_2SiCl to get the precursor (octahydridodimethylsiloxy)silsesquioxane ($Q_8M_8^H$). The attachment of maleimide functionalities was not successful, because of secondary reactions. Hydrosilation of allylmaleimide led to a mixture of products. The double bonds of maleimides or even protected maleimides react with the silane. The result was a cross-linked insoluble product.

As the maleimide-modified spherosilicate could not be synthesized successfully, the preparation of a furfuryl-derivative was inquired. Therefore, allyl bromide was reacted with furfuryl alcohol in the presence of KOH, to give a furfuryl allyl ether (FAE). The aromatic character of the furfuryl prevented hydrosilation at both sides of the ether.

A full functionalization of the spherosilicate could be achieved, as demonstrated by FTIR, ^1H NMR, ^{29}Si NMR and mass spectroscopy. The product $Q_8M_8FAE_8$ could be detected by DLS, giving an average hydrodynamic diameter of 3.2 ± 0.6 nm, which corresponds to the calculated diameter of 3.2 nm. Furthermore, two molecular cross-linkers were used to prepare self-healing composites. A short and stiff bismaleimide with a diphenylmethylene backbone (BMI) and an oligomeric flexible PDMS bismaleimide (M_2-PDMS) were mixed in equimolar ratios with the dienic spherosilicate (Scheme 13). Both products had completely different mechanical properties and self-healing behaviour.
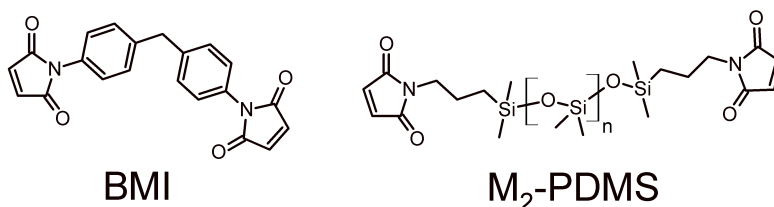
SCHEME 13: DIENOPHILIC CROSS-LINKERS USED IN COMBINATION WITH THE DIENIC SPHEROSILICATES.

FTIR measurements were used to investigate DA reaction. It could be demonstrated that both cross-linkers formed covalent bonds between the furan and maleimide

moieties. $Q_8M_8FAE_8$/BMI is a hard and glassy material, whereas $Q_8M_8FAE_8$/M_2-PDMS is flexible and rubber-like. In both cases, DSC measurements showed endothermic RDA reaction above 90 °C. The kinetics of DA reaction during cooling is dominated by molecular diffusion as shown by the fast and complete curing in the case of BMI. DA reaction is slowed down by the long siloxane backbone in the case of M_2-PDMS. Simple diffusion laws cannot describe the movement of oligomeric molecules. De Gennes et al. developed the reptation model to describe the movement of polymer chains.[53] The increased distance between cross-linking points makes entanglements possible. Once the oligomeric chains are caught up in this entangled state, movement is slowed down, thereby slowing down overall DA reaction.

The results have been published together with a cover profile in the *European Journal of Inorganic Chemistry* in a special cluster issue on *Hybrid Materials – Next Generation:*

T. Engel, G. Kickelbick, Furan-Modified Spherosilicates as Building Blocks for Self-Healing Materials, *Eur. J. Inorg. Chem*. **2015**, *7*, 1226–1232. © 2015 Wiley-VCH Verlag GmbH & Co. KGaA, Weinheim
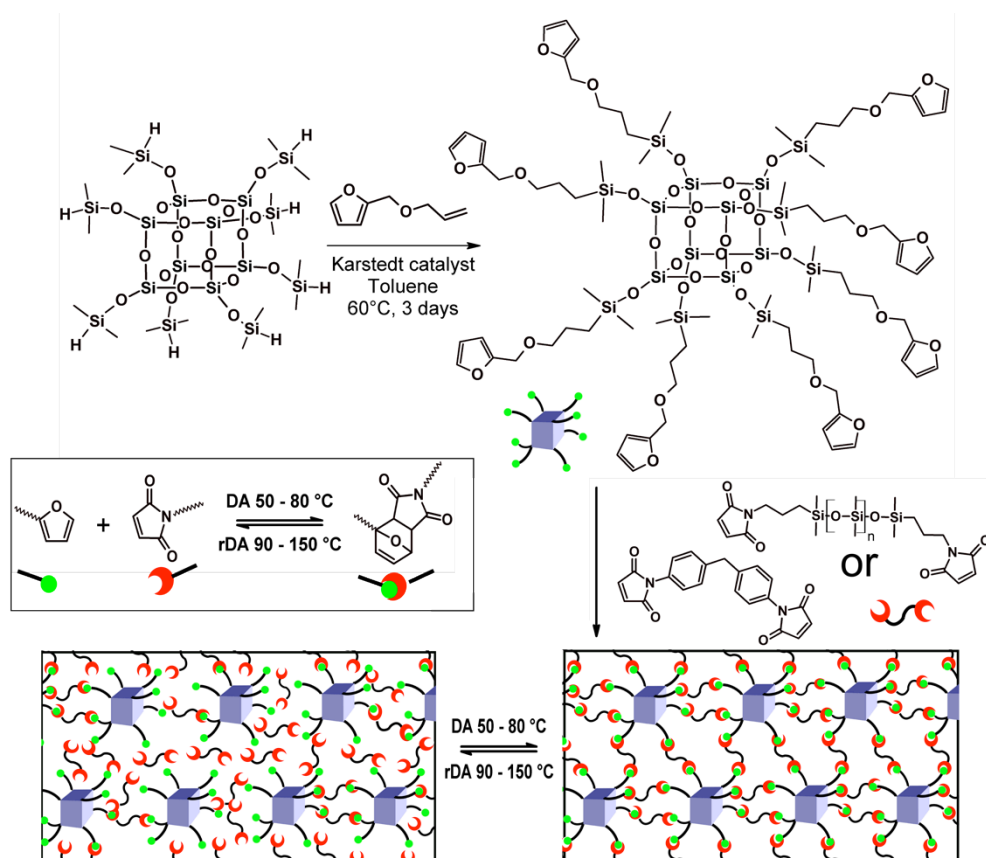
FIGURE 11: *TABLE OF CONTENT*: SYNTHETIC ROUTE FOR THE PREPARATION OF $Q_8M_8FAE_8$. THE CAGE WAS REACTED WITH TWO DIFFERENT CROSS-LINKERS, RESULTING IN SELF-HEALING HYBRID MATERIALS WITH MISCELLANEOUS MECHANICAL PROPERTIES.

CLUSTER ISSUE
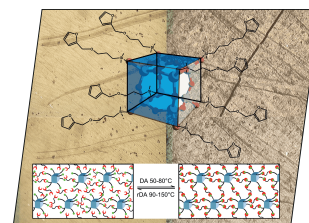
FRONT COVER

Furan-Modified Spherosilicates as Building Blocks for Self-Healing Materials

Tom Engel[a] and Guido Kickelbick*[a,b]

Dedicated to Professor Kaspar Hegetschweiler on the occasion of his 60th birthday

Octafunctional spherosilicates were used to prepare self-healing hybrid materials. The hydrosilation of the octakis-(hydridodimethylsiloxy)-substituted spherosilicate with furfuryl allyl ether generates an inorganic nano-building-block that is used to formulate various self-healing hybrid materials based on a reversible Diels–Alder reaction. Curing with a molecular bismaleimide results in a hard, glassy but reversibly cross-linkable hybrid material. The reversibility of the curing mechanism allows the preparation of films with a heated press, which also opens the possibility to process the materials by injection molding. Substitution of the molecular cross-linker with an oligomeric poly(dimethylsiloxane) bismaleimide results in an elastomeric material. The kinetics of the Diels–Alder reaction upon cooling after a retro-Diels–Alder reaction are mainly controlled by the mobility of the cross-linker within the system.

Introduction

Degradation, damage, and failure are natural consequences of material applications.[1] Intrinsic healing systems allow the repair of damage through latent functionalities. Various external triggers such as light or heat can be used for this approach.[2] Thermally remendable materials based on the Diels–Alder/retro-Diels–Alder (DA/rDA) mechanism are probably the most well-known type of self-healing material.

Polymers with a self-healing ability are mainly based on furfuryl and maleimide groups, which act as dienes and dienophiles in the reversible curing by a Diels–Alder (DA) reaction.[3] The self-healing ability strongly depends on the mobility of the functional groups and the ratio of maleimide to furan.[4] A nonstoichiometric ratio increases the probability that new cross-links will form. In previous work, we designed self-healing nanocomposites based on silica–polymer core–shell nanoparticles.[5] After curing, these materials could be healed at temperatures above the rDA temperature within minutes. The only drawback was the slow formation of new DA bonds upon cooling. Typically, annealing at 70 °C for 12 h was required for high healing efficiency. In conventional thermally remendable polymers, which do not contain inorganic components, hetero-DA reactions of dithioesters and cyclopentadiene can accelerate the cross-linking reaction dramatically.[6] In hybrid materials or nanocomposites, it is not only the DA/rDA velocity itself but also the diffusion and mobility of the inorganic components in the material that determines the speed of the cross-linking; thus, a decrease of the size of the building blocks should increase the reaction rates.

Compared to silica nanoparticles, which we have already used as cross-linkers in self-healing nanocomposites, spherosilicates are quite small. Spherosilicates and particularly polyhedral oligomeric silsesquioxanes (POSS) have shown their ability to improve polymer properties. Monofunctional molecules can be used as comonomers,[7] and multifunctional starlike POSS molecules were employed as cross-linkers or as macroinitiators.[8] The first approaches to use POSS cages in self-healing coatings were presented recently by Lin et al.[9]

In this work, we present a new synthetic strategy for the preparation of multifunctional spherosilicates with diene moieties that can be employed in thermally remendable self-healing hybrids. We investigated the influence of the size of the inorganic building blocks as well as the type of organic cross-linker on the healing properties of the final materials.

[a] Inorganic Solid State Chemistry, Saarland University, Am Markt, Zeile 3, 66125 Saarbrücken, Germany
[b] INM – Leibniz-Institut für Neue Materialien GmbH, Campus D2₂, 66123 Saarbrücken, Germany
E-mail: guido.kickelbick@uni-saarland.de
http://www.uni-saarland.de/lehrstuhl/kickelbick.html
Supporting information for this article is available on the WWW under http://dx.doi.org/10.1002/ejic.201402551.

Results and Discussion

Synthesis of Octa-Furfuryl-Modified Spherosilicate

The hydrosilation of 2-[(prop-2-en-1-yloxy)methyl]furan (furfuryl allyl ether, FAE) with octakis(hydridodimethylsiloxy)-substituted spherosilicate ($Q_8M_8^H$) was performed to synthesize a cagelike polyhedral spherosilicate with eight diene functional groups. The octahydridospherosilicate was prepared according to a modified literature procedure.[10] Compared to the synthesis of silsesquioxanes, the spherosilicate production requires shorter reaction times and results in higher yields of the target material. In a first step, the controlled hydrolysis and condensation of tetraethoxysilane (TEOS) with tetramethylammonium hydroxide resulted in a solution of the octaanion,[10a] which was reacted with dimethylchlorosilane to afford $Q_8M_8^H$ in 69 % yield. Characterization by infrared spectroscopy showed a distinctive Si–H vibration at $\tilde{\nu} = 2141$ cm^{-1} and a strong asymmetric Si–O–Si stretching signal at $\tilde{\nu} = 1067$ cm^{-1} (Figure 1). As $Q_8M_8^H$ is readily soluble in many organic solvents, we analyzed the product by solution-state NMR spectroscopy. ^{1}H NMR spectroscopy disclosed a heptet at $\delta = 4.74$ ppm, which is assigned to the 8 Si–H protons (Figure S1). The multiplet at $\delta = 0.26$ ppm was assigned to the 48 protons of the dimethylsilyl groups (Figure S2).

The ^{29}Si NMR spectrum of $Q_8M_8^H$ in CDCl$_3$ showed a signal at $\delta = -109.03$ ppm for the Q^4 species of the SiO$_2$ cube and a signal at $\delta = -1.88$ ppm assigned to the silicon atoms bearing the hydrogen atoms (Figure S3).

By applying a modified literature procedure,[11] FAE was obtained in 81 % yield by a substitution reaction of furfuryl alcohol and allyl bromide. The hydrosilation of FAE with $Q_8M_8^H$ in the presence of the Karstedt catalyst was successfully employed to functionalize all eight corners of the cubic structure with Diels–Alder (DA) reactive groups (Scheme 1). The product was obtained quantitatively as a viscous liquid. The aromatic nature of the furfuryl ring prevents hydrosilation across the diene as a side reaction.

A comparison of the FTIR spectra of $Q_8M_8FAE_8$ and $Q_8M_8^H$ showed the complete disappearance of the Si–H stretching vibration, which demonstrates that all eight corners have reacted. Additionally, specific signals for the furfuryl moieties emerged at $\tilde{\nu} = 3129$, 1503, 1438, and 1411 cm^{-1} (Figure 1).

NMR spectroscopy also demonstrated the complete conversion of $Q_8M_8^H$ (Figures 2 and 3). No allylic protons could be detected, and a signal at $\delta = 0.60$ ppm for the newly formed CH$_2$–Si species was observed. ^{29}Si NMR spectroscopy also confirmed that all Si–H bonds had

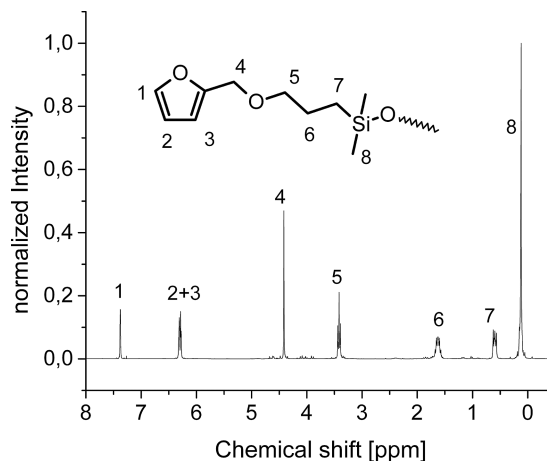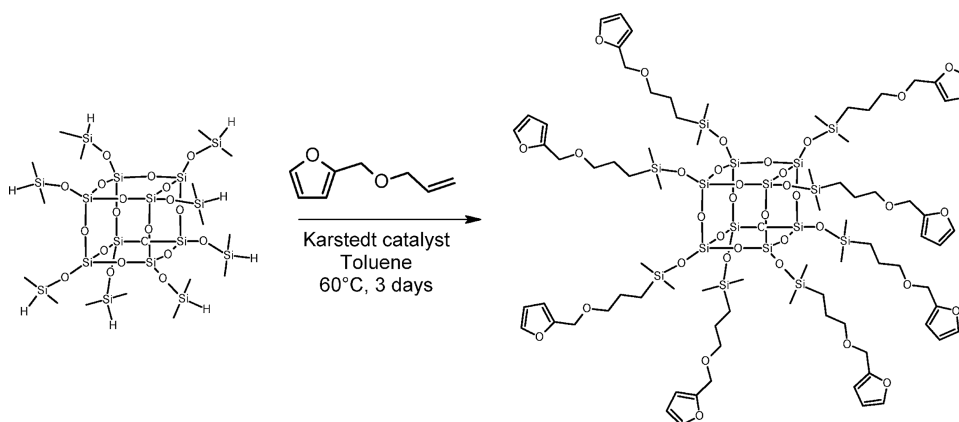Figure 1. FTIR spectra of $Q_8M_8^H$ and $Q_8M_8FAE_8$.

Figure 2. ^{1}H NMR spectrum of $Q_8M_8FAE_8$.

Scheme 1. Functionalization of $Q_8M_8^H$ with FAE.

reacted, and the newly formed Si–C bonds gave rise to a signal at δ = 12.90 ppm.
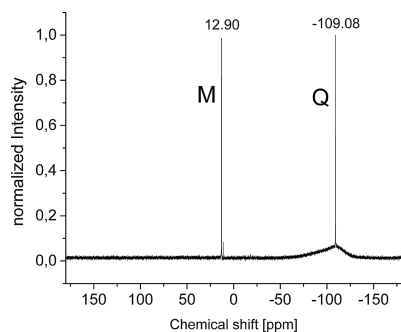

Figure 3. ^{29}Si NMR spectrum of $Q_8M_8FAE_8$.

Dynamic light scattering (DLS) measurements of the as-prepared functional cages revealed a hydrodynamic diameter of (3.16 ± 0.64) nm in acetone, which was in good agreement with the calculated diameter of ca. 3.2 nm from the standard bond lengths (Figure 4).
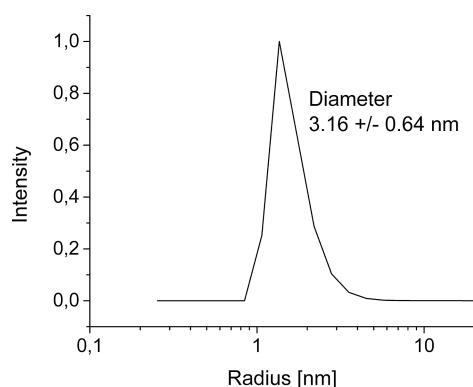

Figure 4. DLS size distribution of $Q_8M_8FAE_8$ in acetone.

Furthermore, in the ESI Fourier transform ion cyclotron resonance (ESI-FTICR) MS spectrum of the product, several peaks corresponded to $[M + K]^+$, $[M + NH_4]^+$, and $[M + 2H]^{2+}$ at m/z = 2162.52, 2140.57, and 1062.26, respectively (Figures S7 and S8). Isolation followed by fragmentation of the $[M + 2H]^{2+}$ species revealed fragmentation steps through which the FAE pendant groups are replaced by sodium ions (Figure S9).

Synthesis of Bismaleimido–Polymethylsiloxane Cross-Linker (M_2-PDMS)

The commercially available 1,1′-(methylenedi-4,1-phenylene)bismaleimide (BMI) was used as a molecular cross-linker for the newly prepared $Q_8M_8FAE_8$. To obtain a more-flexible cross-linker for the preparation of elastomeric materials, α,ω-diaminopropyl-terminated oligo-polydimethylsiloxane (PDMS) was treated with maleic anhydride followed by ring closure with zinc chloride and hexamethyldisilazane to form the α,ω-bismaleimidopropyl-PDMS (M_2-PDMS, Scheme 2).[12] The commercially available precursor had a mean degree of polymerization (DP) of eight dimeth-

ylsiloxy units as determined by ^{1}H NMR spectroscopy. M_2-PDMS was characterized by NMR spectroscopy. All aminopropyl end groups reacted with maleic anhydride, and ring closure occurred in a yield of 89% to form maleimidopropyl end groups.
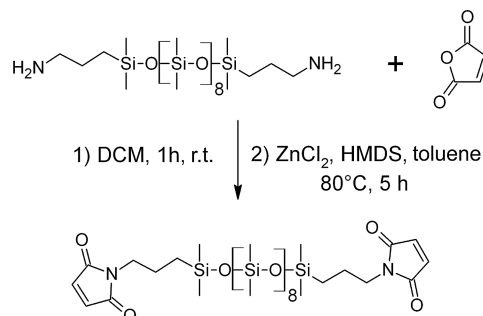
Scheme 2. Synthesis of the cross-linker M_2-PDMS.

DA Curing with Both Cross-Linkers

DA reactions between $Q_8M_8FAE_8$ and the two different cross-linkers, BMI and the oligomeric M_2-PDMS, were investigated (Scheme 3). For BMI, both starting materials were dissolved in $CDCl_3$ to enable in situ monitoring of the DA reaction by ^{1}H NMR spectroscopy at room temperature (Figure 5). The signals for the DA adduct emerged gradually at δ = 5.3 and 6.4 ppm. At room temperature in dilute concentration, the reaction is relatively slow. The integrated product signal at δ = 5.3 ppm follows a linear trend up to a reaction time of 18 h (Figure 6).
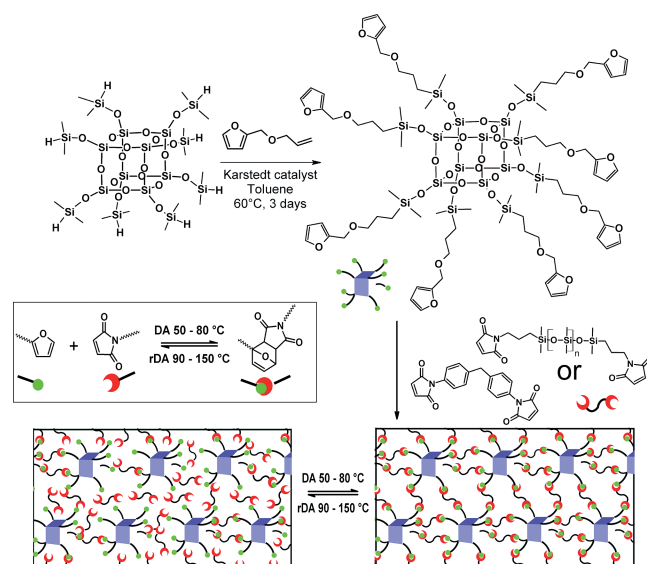
Scheme 3. Schematic representation of the self-healing hybrid material.

The low intensity of the product signals is due to the low solubility of the highly cross-linked products, which precipitate from the reaction solution. The bulk reaction at 70 °C afforded a hard, glassy, orange material as reported by Lin and co-workers.[9]
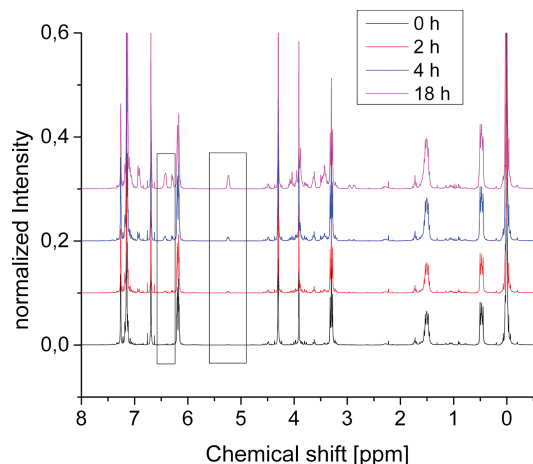
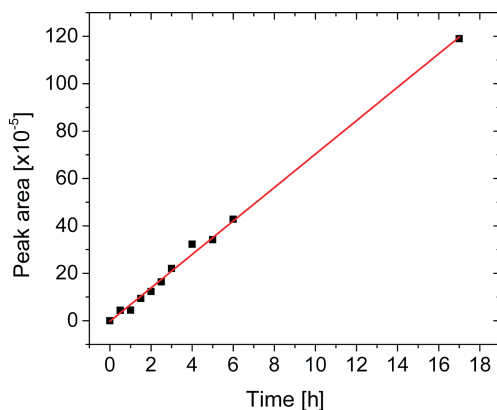Figure 5. ^{1}H NMR spectra of the DA reaction between $Q_8M_8FAE_8$ and BMI.

Figure 6. DA adduct peak area over time during in situ ^{1}H NMR spectroscopy.

Figure 7. FTIR spectra of (a) BMI, $Q_8M_8FAE_8$, and their DA adduct and (b) M_2-PDMS, $Q_8M_8FAE_8$, and their DA adduct.

For M_2-PDMS, no solvent was required for mixing as both monomers were liquids. An elastomeric hybrid material was produced by simply mixing $Q_8M_8FAE_8$ with M_2-PDMS, followed by 10 min of vigorous shaking and a DA reaction at 70 °C within a mould.

The DA reactions of both materials were also confirmed by FTIR spectroscopy measurements. In comparison with that of the uncured BMI, the carbonyl stretch of the cured composite showed a blueshift from $\tilde{\nu}$ = 1702 to 1707 cm^{-1}. Furthermore, the maleimide ring-deformation signal at $\tilde{\nu}$ = 686 cm^{-1} disappeared (Figure 7, a). The elastomeric material showed a redshift of the carbonyl stretching mode from $\tilde{\nu}$ = 1710 cm^{-1} for the free M_2-PDMS to 1701 cm^{-1} for the DA adduct. The disappearance of the maleimide ring-deformation signal at $\tilde{\nu}$ = 696 cm^{-1} was also observed (Figure 7, b). These differences in the positions of the signals are due to the difference in the electronic structures emerging from the conjugation of a phenyl ring to the maleimide ring.

Differential scanning calorimetry (DSC) measurements were used to visualize the retro-DA reaction within a previously cross-linked material. At temperatures as high as 180 °C, exothermic polymerization of maleimides and decomposition leads to mass loss and undesired irreversibly
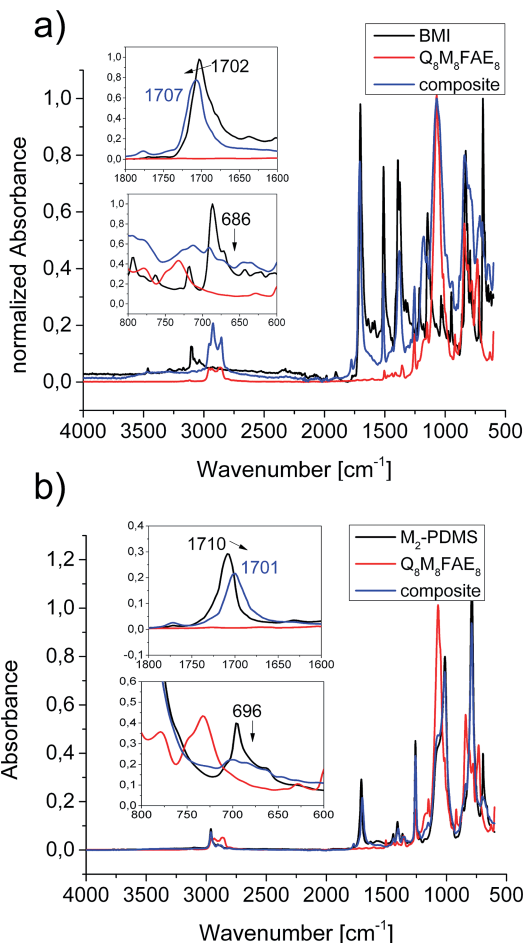
cross-linked species. Therefore, a maximum temperature of 155 °C was chosen for the DSC measurements. For the BMI-cross-linked material, the first heating cycle showed a broad endothermic signal above 90 °C of 25.5 J/g, which is related to the retro-DA reaction of the previously reacted furfuryl and maleimide moieties (Figure 8).
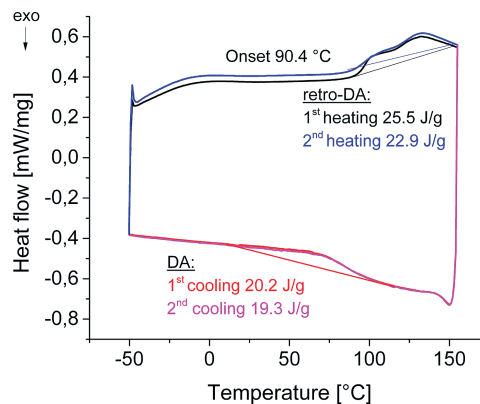

Figure 8. DSC curve of $Q_8M_8FAE_8$ previously cured with BMI.

During the following cooling, a rapid recuring was observed and was accompanied by a broad endothermic DA reaction signal over a range of 100 °C. Nearly the same

amount of energy was consumed during this step as during the retro-DA reaction. The breaking and recombination could be repeated in the next heating and cooling cycle. This result was unexpected, because previous work on self-healing nanocomposites with polymer-grafted silica nanoparticles reacted on a completely different time scale. In these systems, only very little DA reaction was detected during cooling, because the mobility of the reactive furfuryl and maleimide groups was directly linked to the mobility of the polymeric chains, which is often described by the reptation model of polymer chains.[13] In this new material, both reaction partners are molecular species, which can move by simple molecular diffusion at the border of the forming cross-linked solid. The small difference in the extent of the cross-linking, observed by a drop of 25.5 to 22.9 J/g could be explained by trapped unreacted bismaleimide molecules or dangling unreacted maleimides.

The DSC curve of the elastomeric, M_2-PDMS-cross-linked material, showed the same behavior during the first heating cycle. Only the amount of energy needed for the retro-DA reaction was inferior (Figure 9). Secondly, it was observed that the DA reaction during cooling was relatively slow. During the second heating step, only a third of the original cross-linking density was obtained. This can be explained by the relatively high molecular weight of the M_2-PDMS cross-linker and the accompanying lower mobility of the pendant maleimide groups. Furthermore, in previous work, it was shown that the conjugated phenyl rings increase the reaction rate of the DA reaction by a factor of two.[14]
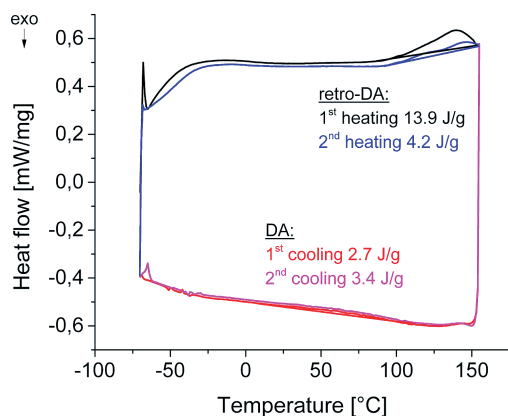

Figure 9. DSC curve of $Q_8M_8FAE_8$ previously cured with M_2-PDMS.

Damage Healing by Thermal Treatment

For the BMI-cured spherosilicates, scratch-healing experiments were performed on pressed films of 100 µm thickness. For that, a sample of 100 mg was heated to 135 °C between two silicon wafers of a heated film-maker press. After 15 min at this temperature, a transparent 100 µm thick film was prepared by using a pressure of 2 tons (Figure 10). As the film preparation is possible, the use of injec-

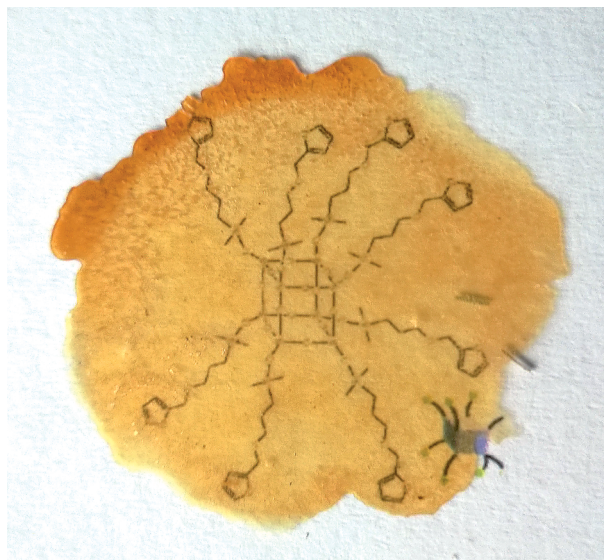tion-molding techniques for the preparation of specimens would also be possible.

Figure 10. 100 µm film prepared with a heatable press.

For the M_2-PDMS-cured spherosilicates, a disclike specimen was prepared in a glass recipient. The specimen was then broken and reshaped by thermal treatment at 135 °C followed by several hours at 70 °C within a rectangular mold (Figure 11).

Figure 11. Rectangular specimen molded by healing and reshaping of M_2-PDMS-cured $Q_8M_8FAE_8$.

The scratch-healing test was monitored by conventional transmission light microscopy. Two scratches on the surface of the BMI-cured spherosilicate before and after heat-treatment at 110 °C are shown in Figure 12 (a). A rapid smoothing of the film surface was observed, and the two scratches disappeared almost entirely after a few minutes. Complete liquefaction above 150 °C would lead to complete disappearance of the surface damage but would be accompanied by the loss of the original shape of the specimen. The healing of a crack within the rectangular specimen of M_2-PDMS-cured spherosilicate is shown in Figure 12 (b). Within 10 min at 100 °C, the crack closed completely. The elastomeric nature of the PDMS-based composite is favorable for crack-healing behavior.
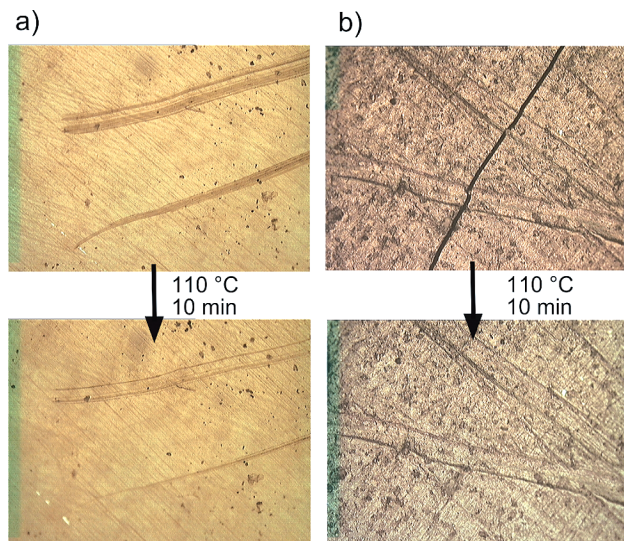
Figure 12. Damage healing at 110 °C of (a) a BMI-cured $Q_8M_8FAE_8$ film and (b) a M_2-PDMS-cured $Q_8M_8FAE_8$ specimen.

Conclusions

A new synthetic strategy for the preparation of dienic spherosilicates was presented. The modification of a $Q_8M_8^H$ cage was obtained by a hydrosilation approach. The full modification of all eight corners with furfuryl allyl ether was achieved by applying this procedure. A DA reaction between furfuryl ether modified spherosilicates ($Q_8M_8FAE_8$) with two different maleimide cross-linkers led to bulk hybrid materials. Depending on the nature of the cross-linker, two self-healing composites with different mechanical properties and healing abilities were obtained. Curing with molecular, stiff BMI led to a hard, glassy solid. The application of oligomeric M_2-PDMS resulted in an elastomeric material. NMR spectroscopy could be used to monitor the DA reaction. DSC measurements showed a broad retro-DA reaction signal above 90 °C. Differences in the DA reaction rate during cooling were observed. The mobility of the molecular bismaleimide in the melt was superior and, thereby, enabled nearly complete reconnection upon cooling. The kinetics of the oligomeric system is lower because the mobility of the functional dienophilic groups is governed by the typical diffusion mechanism of polymeric chains.

Finally, scratch-healing experiments were followed by light microscopy. Within minutes, fast repair of the damage could by visualized.

Experimental Section

Materials: Tetraethoxysilane was kindly provided by Wacker Silicones. Chlorodimethylsilane, aminopropyl-terminated poly(dimethylsiloxane) and Karstedt catalyst were purchased from ABCR. Tetramethylammonium hydroxide pentahydrate, furfuryl alcohol, allyl bromide, maleic anhydride and 1,1′-(methylenedi-4,1-phenylene)bismaleimide were purchased from Sigma–Aldrich. All chemicals were used as received or purified by standard procedures.

Methods: Fourier transform infrared (FTIR) spectroscopy measurements were performed with a Bruker Vertex 70 Spectrometer under ambient air (40 scans at a resolution of 4 cm^{-1}) in attenuated total reflectance (ATR) mode. Differential scanning calorimetry (DSC) measurements were performed with a Netzsch DSC 204 F1 Phoenix calorimeter with samples in aluminum crucibles with pierced lids and heated under nitrogen at a rate of 10 K/min. Solution NMR spectra were recorded with a Bruker Avance 300 spectrometer at 25 °C (^{1}H at 300.13 MHz, ^{13}C at 75.48 MHz, ^{29}Si at 59.63 MHz). Elemental analysis was performed with a Leco 900 CHN analyzer. Dynamic light scattering (DLS) measurements were performed by noninvasive backscattering with an ALV/CGS-3 compact goniometer system with an ALV/LSE-5003 correlator and multiple tau correlator at a wavelength of 632.8 nm (He–Ne Laser) and at a 90° goniometer angle. The dispersing media were purified before use with a syringe filter (200 nm mesh). The determination of the particle radius was carried out by the analysis of the correlation function by the $g2(t)$ method followed by a linearized number-weighting (n.w.) of the distribution function. High-resolution mass spectroscopy (HRMS) was performed with a solariX 7 Tesla FTICR mass spectrometer (Bruker Daltonik, Bremen, Germany). All samples were ionized by electrospray ionization (ESI). In MS/MS mode, precursor ions were isolated first in the quadrupole and externally accumulated in the hexapole for 0.1 s. For collision-induced dissociation (CID), a collision voltage of 2–10 V was applied.

Octakis(hydridodimethylsiloxy)octasilsesquioxane ($Q_8M_8^H$): Octakis(hydridodimethylsiloxy)octasilsesquioxane was prepared by a modified literature procedure.[10] In a 250 mL three-necked round-bottom flask with a magnetic stir bar, tetramethylammonium hydroxide (17.73 g, 0.1 mol) was dissolved in methanol (53 mL) and water (13 mL). The flask was cooled in an ice bath, and tetraethoxysilane (19.15 mL, 18.00 g, 0.086 mol) was added. The solution was stirred overnight at room temperature to give the octaanion solution. At the second stage, the solution was slowly added through a dropping funnel to a solution of dimethylchlorosilane (32.44 g, 0.34 mol) in pentane (300 mL) at 0 °C. Afterwards, the mixture was kept at room temperature for 3 h. The organic layer was separated, and the solvent was removed by rotary evaporation. The resulting white solid was washed several times with methanol and dried in vacuo, yield 7.5 g (7.37 mmol, 69%). ^{1}H NMR (CDCl$_3$, 25 °C): δ = 0.26 (td, 48 H, Si(CH$_3$)$_2$), 4.74 (hp, 8 H, SiH) ppm. ^{13}C NMR (CDCl$_3$, 25 °C): δ = 0.06 [Si(CH$_3$)$_2$] ppm. ^{29}Si (CDCl$_3$, 25 °C): δ = –1.88 (SiH), –109.03 (SiOSi) ppm. IR: $\tilde{\nu}$ = 2962 (CH), 2141 (SiH), 1253, 1067 (asym SiOSi), 896, 835, 753 (sym SiOSi) cm^{-1}.

2-[(Prop-2-en-1-yloxy)methyl] furan (FAE): In a 100 mL round-bottom flask with a magnetic stir bar, furfuryl alcohol (10 g, 0.102 mol) and KOH (22.88 g, 0.408 mol) were added and stirred at 0 °C for 10 min. Afterwards, allyl bromide (18.51 g, 0.153 mol) was added slowly at 0 °C. The reaction mixture was stirred at 60 °C overnight. Dichloromethane (DCM, 100 mL) was added, and the excess KOH was extracted three times with water. The organic phase was dried with anhydrous sodium sulfate, and the solvent, excess allyl bromide, and allyl alcohol were removed by rotary evaporation. Finally, the slightly yellow product was purified by vacuum distillation, yield 11.50 g (0.083 mol, 81.6%). ^{1}H NMR (CDCl$_3$, 25 °C): δ = 4.00 (dt, ^3J = 5.7 Hz, ^4J = 1.4 Hz, 2 H, CH$_2$ allyl), 4.46 (s, 2 H, CH$_2$ furfuryl), 5.20 (dm, ^2J = 9.0 Hz, 1 H, C=CH$_2$), 5.30 (dq, ^2J = 17.3 Hz, ^3J = 1.6 Hz, ^4J = 1.6 Hz, 1 H, C=CH$_2$), 5.92 (m, 1 H, CH$_2$CH=C), 6.31–6.35 (m, 2 H, HC=CH), 7.40 (dd, ^3J = 1.8 Hz, ^4J = 0.9 Hz, 1 H, OHC=C) ppm. ^{13}C NMR (CDCl$_3$, 25 °C): δ = 63.70 (CH$_2$ allyl), 70.79 (CH$_2$ furfuryl), 109.11 (C=C

furan), 110.11 (C=C furan), 117.29 (C=C allyl), 134.32 (C=C allyl), 142.61 (C=C furan), 151.68 (C=C furan) ppm. IR: $\tilde{\nu}$ = 3148 (HC=C), 3119 (HC=C), 3080 (HC=C), 2979 (C–H), 2905 (C–H), 2854 (C–H), 1646 (C=C), 1503 (C=C), 1354, 1225, 1154, 1072, 1003, 917, 734 cm^{-1}.

Octakis[(furfuryl propyl ether)dimethylsiloxy]octasilsesquioxane (Q$_8$M$_8$FAE$_8$): In a 25 mL Schlenk flask with a magnetic stir bar under an argon atmosphere, octakis(hydridodimethylsiloxy)octasilsesquioxane (1 g, 0.98 mmol) and FAE (1.11 g, 8.0 mmol) were dissolved in dry toluene (10 mL). A solution of Karstedt catalyst in xylene (25 µL) was added, and the reaction mixture was stirred at 60 °C for 3 d. Finally, the toluene and excess FAE were removed in vacuo to yield a slightly yellow viscous liquid that was analytically pure, yield quantitative. ^{1}H NMR (CDCl$_3$, 25 °C): δ = 0.12 (s, 7 H, CH$_3$Si), 0.60 (m, 2 H, CH$_2$Si), 1.63 (m, 2 H, CH$_2$CH$_2$CH$_2$), 3.42 (t, ^3J = 6.8 Hz, 2 H, OCH$_2$CH$_2$), 4.42 (s, 2 H, CH$_2$ furfuryl), 6.28–6.32 (m, 2 H, HC=CH), 7.38 (dd, ^3J = 1.7 Hz, ^4J = 0.8 Hz, 1 H, OHC=C) ppm. ^{13}C NMR (CDCl$_3$, 25 °C): δ = –0.01 (CH$_3$Si), 14.12 (CH$_2$Si), 23.55 (CH$_2$CH$_2$CH$_2$), 65.06 (OCH$_2$CH$_2$), 73.26 (CH$_2$ furfuryl), 109.33 (C=C), 110.61 (C=C), 142.96 (C=C), 152.57 (C=C) ppm. ^{29}Si (CDCl$_3$, 25 °C): δ = –109.08, 12.90 ppm. IR: $\tilde{\nu}$ = 3129 (HC=C), 2950 (C–H), 2853 (C–H), 1503 (C=C), 1438 (C=C), 1411 (C=C), 1356, 1151, 1071, 839, 730 cm^{-1}. C$_{80}$H$_{136}$O$_{36}$Si$_{16}$ (2123.31): calcd. C 45.25, H 6.46; found C 42.85, H 6.21. HRMS (ESI-FTICR): calcd for C$_{80}$H$_{136}$O$_{36}$Si$_{16}$K [M + K]$^+$ 2162.4100; found 2162.5210; calcd. for C$_{80}$H$_{140}$O$_{36}$Si$_{16}$N [M + NH$_4$]$^+$ 2141.1467; found 2140.5704; calcd. for C$_{80}$H$_{138}$O$_{36}$Si$_{16}$ [M + 2H]$^{2+}$ 1062.5622; found 1062.2615.

Bis(maleimidopropyl)-Terminated Polydimethylsiloxane (M$_2$-PDMS): In a 100 mL round-bottomed flask, maleic anhydride (2.33 g, 0.024 mol) was dissolved in DCM (50 mL). A solution of aminopropyl-terminated PDMS (10 g, 0.012 mol) in DCM (20 mL) was added dropwise through a dropping funnel to the stirred maleic anhydride solution. The resulting solution was stirred for 1 h. Afterwards, the solvent was removed by rotary evaporation. The resulting viscous liquid was dissolved in anhydrous toluene (50 mL), and ZnCl$_2$ (3.27 g, 0.024 mol) was added as the mixture was heated to 80 °C. After the addition of hexamethyldisilazane (3.87 g, 0.024 mol), the reaction was continued for 5 h. First, the solid was removed by filtration, and then the solvent was removed by rotary evaporation followed by drying under high vacuum, yield 11.23 g (0.011 mol; 91.7%). ^{1}H NMR (CDCl$_3$, 25 °C): δ = 0.00–0.13 (m, 77 H, CH$_3$Si), 0.49 (m, 4 H, CH$_2$Si), 1.60 (m, 4 H, CH$_2$CH$_2$CH$_2$), 3.49 (t, J = 3.5 Hz, 4 H, NCH$_2$), 6.68 (s, 4 H, HC=CH) ppm. ^{13}C NMR (CDCl$_3$, 25 °C): δ = 0.03 (CH$_3$Si), 1.00 (CH$_3$Si), 1.74 (CH$_3$Si), 15.21 (CH$_2$Si), 22.50 (CH$_2$CH$_2$CH$_2$), 40.71 (NCH$_2$), 133.98 (C=C), 170.84 (C=O) ppm. ^{29}Si (CDCl$_3$, 25 °C): δ = –21.96, –21.22, 7.06 ppm. IR: $\tilde{\nu}$ = 3103 (HC=C), 2963 (C–H), 1710 (C=O), 1443 (C=C), 1406 (C=C), 1257 (C–H), 1011 (Si–O–Si), 790 (Si–O–Si) cm^{-1}.

Supporting Information (see footnote on the first page of this article): Additional NMR spectroscopic data of Q$_8$M$_8$^{H} and M$_2$-PDMS and HRMS spectroscopic data of Q$_8$M$_8$FAE$_8$.

[1] B. J. Blaiszik, S. L. B. Kramer, S. C. Olugebefola, J. S. Moore, N. R. Sottos, S. R. White, *Annu. Rev. Mater. Res.* **2010**, *40*, 179–211.

[2] T. Engel, G. Kickelbick, in: *Self-Healing Polymers: From Principles to Applications* (Ed.: W. H. Binder), Wiley-VCH, Weinheim, Germany, **2013**, p. 153–171.

[3] a) X. Chen, M. A. Dam, K. Ono, A. Mal, H. Shen, S. R. Nut, K. Sheran, F. Wudl, *Science* **2002**, *295*, 1698–1702; b) X. Chen, F. Wudl, A. K. Mal, H. Shen, S. R. Nutt, *Macromolecules* **2003**, *36*, 1802–1807; c) T. Dispinar, R. Sanyal, A. Sanyal, *J. Polym. Sci., Part A Polym. Chem.* **2007**, *45*, 4545–4551; d) A. A. Kavitha, N. K. Singha, *Macromol. Chem. Phys.* **2007**, *208*, 2569–2577.

[4] C. Zeng, H. Seino, J. Ren, K. Hatanaka, N. Yoshie, *Polymer* **2013**, *54*, 5351–5357.

[5] T. Engel, G. Kickelbick, *Polym. Int.* **2014**, *63*, 915–923.

[6] a) A. J. Inglis, L. Nebhani, O. Altintas, F. G. Schmidt, C. Barner-Kowollik, *Macromolecules* **2010**, *43*, 5515–5520; b) A. J. Inglis, S. Sinnwell, M. H. Stenzel, C. Barner-Kowollik, *Angew. Chem. Int. Ed.* **2009**, *48*, 2411–2414; c) K. K. Oehlenschlaeger, J. O. Mueller, J. Brandt, S. Hilf, A. Lederer, M. Wilhelm, R. Graf, M. L. Coote, F. G. Schmidt, C. Barner-Kowollik, *Adv. Mater.* **2014**, *26*, 3561–3566.

[7] a) J. Choi, J. Harcup, A. F. Yee, Q. Zhu, R. M. Laine, *J. Am. Chem. Soc.* **2001**, *123*, 11420–11430; b) J. D. Lichtenhan, Y. A. Otonari, M. J. Carr, *Macromolecules* **1995**, *28*, 8435–8437; c) J. Pyun, K. Matyjaszewski, *Chem. Mater.* **2001**, *13*, 3436–3448.

[8] a) S. Klapdohr, N. Moszner, G. Kickelbick, R.-P. Krueger, *Monatsh. Chem.* **2006**, *137*, 667–679; b) J. Pyun, K. Matyjaszewski, T. Kowalewski, D. Savin, G. Patterson, G. Kickelbick, N. Huesing, *J. Am. Chem. Soc.* **2001**, *123*, 9445–9446; c) D. Holzinger, G. Kickelbick, *J. Polym. Sci., Part A Polym. Chem.* **2002**, *40*, 3858–3872.

[9] Z. Xu, Y. Zhao, X. Wang, T. Lin, *Chem. Commun.* **2013**, *49*, 6755–6757.

[10] a) I. Hasegawa, S. Motojima, *J. Organomet. Chem.* **1992**, *441*, 373–380; b) M. Dutkiewicz, H. Maciejewski, B. Marciniec, J. Karasiewicz, *Organometallics* **2011**, *30*, 2149–2153.

[11] I. Pitsch, D. Hoebbel, H. Jancke, W. Hiller, *Z. Anorg. Allg. Chem.* **1991**, *596*, 63–72.

[12] M. Proupin-Perez, R. Cosstick, L. M. Liz-Marzan, V. Salgueirino-Maceira, M. Brust, *Nucleosides Nucleotides Nucleic Acids* **2005**, *24*, 1075–1079.

[13] P. G. de Gennes, *J. Chem. Phys.* **1971**, *55*, 572–579.

[14] T. Engel, G. Kickelbick, *Chem. Mater.* **2013**, *25*, 149–157.

3.4 Supplementary results

3.4.1 Nano-structured Hybrid Material

BMI and octafunctional spherosilicate $Q_8M_8FAE_8$ were both dissolved in chloroform prior to curing by DA reaction. Chloroform was then removed by rotary evaporation, and the mixture was cured at 70 °C. Subsequent TGA-FTIR measurements revealed that not all chloroform could be removed, because some molecules were incorporated within the forming network. The trapped chloroform molecules were only liberated after the RDA took place at temperatures as high as 140 °C. This could be substantiated by FTIR measurements of the decomposition gases. Chloroform has two very specific strongly infrared-active signals at 1219 and 769 cm^{-1}. They are assigned to the C-H deformation and the C-Cl stretching, respectively. Figure 12 shows the infrared spectrum of the liberated chloroform at 140 °C.
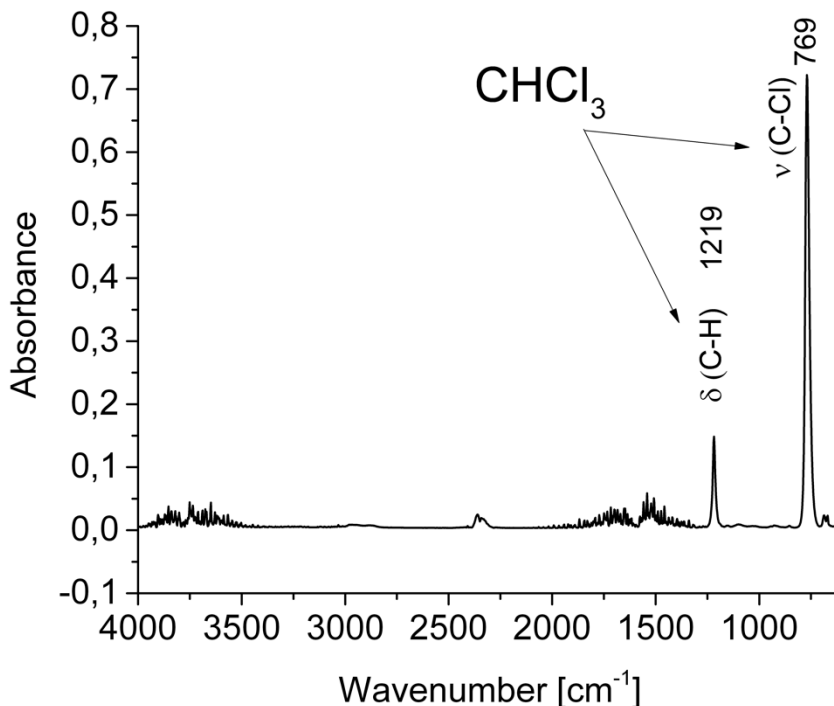

FIGURE 12: GAS-PHASE FT-IR SPECTRUM OF CHLOROFORM RELEASED FROM HYBRID $Q_8M_8FAE_8$/BMI UPON HEATING TO RETRO-DIELS-ALDER TEMPERATURE.

The 3-dimensional TG-FTIR chromatogram in figure 13 shows that chloroform is liberated in two steps in the range of 100 to 200 °C. The two steps may be explained

by the difference in RDA temperature of *endo-* and *exo*-DA-products. During curing the kinetically favoured *endo*-adduct is preferentially formed, but also small amounts of the thermodynamically favoured *exo*-adduct is generated. First RDA of the *endo*-adduct occurred, liberating most of the chloroform at 140 °C. RDA of the *exo*-adducts released the rest of the chloroform at 160 °C.
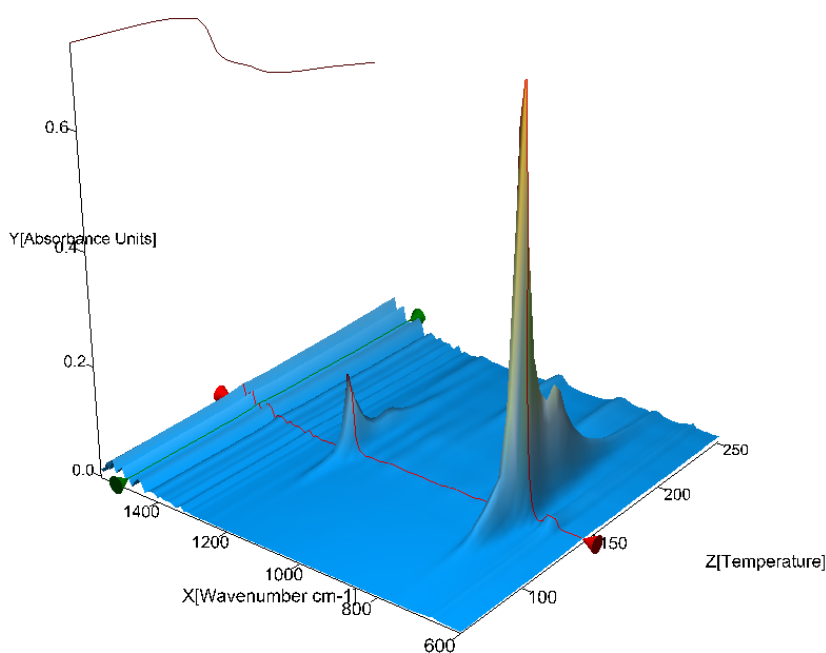

FIGURE 13: THREE-DIMENSIONAL FTIR CHROMATOGRAM OF DECOMPOSITION GASES RELEASED FROM $Q_8M_8FAE_8$/BMI DURING TGA EXPERIMENT.

On the other hand, the TGA curve allows quantifying the amount of solvent incorporated within the inorganic-organic hybrid network. It could be shown that 11.8 % of the initial mass was lost in the temperature range of the RDA reaction between 100 and 200 °C (Figure 14). This amounts to 1 mmol of chloroform per gram of network. By burning all organic parts of the material 22 % of pure SiO_2 remains at the end of the TGA experiment. A total number of 4 solvent molecules per spherosilicate molecule could be calculated.

The incorporation of solvent into the cross-linked hybrid material, together with TGA-FTIR measurements, delivered an indirect insight within the nano-structure of the material. The regular arrangement of the cubic spherosilicates provides ordered voids big enough to trap single chloroform molecules.
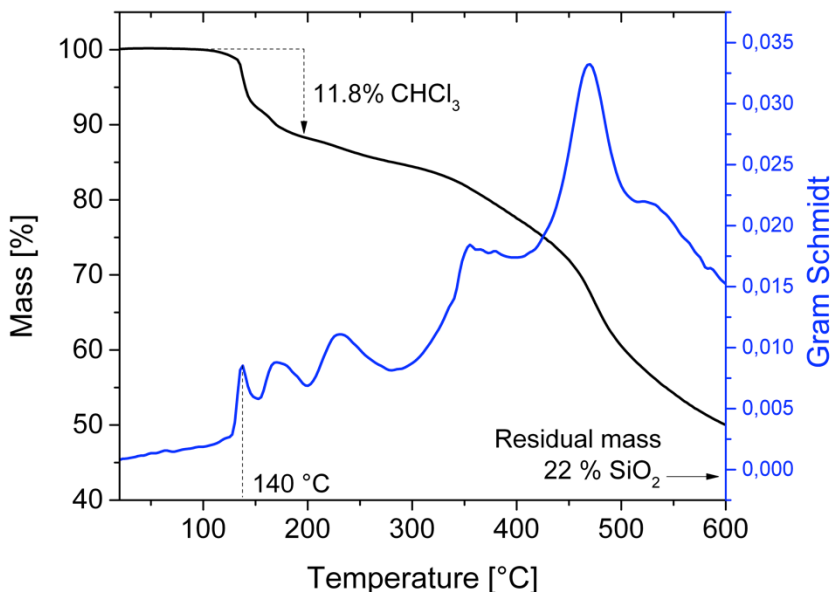
FIGURE 14: TGA EXPERIMENT SHOWING THE MASS LOSS OF THE HYBRID MATERIAL $Q_8M_8FAE_8$/BMI UPON HEATING AND THE CORRESPONDING GRAM SCHMIDT CURVE, REFLECTING THE SUM OF FTIR SIGNALS GENERATED BY ANALYSING THE DECOMPOSITION GASES.

3.4.2 Comparative investigation of the influence of cross-linkers on the self-healing behaviour

An investigation of the influence on DA reactivity, cross-linking density and self-healing ability of the different cross-linking agents synthesized in course of this work was conducted.

Different experiments were performed on different furfuryl cross-linkers within a poly(butyl methacrylate-co-maleimidopropyl methacrylate) [P(BMA-co-MiMA$_{0.1}$)] matrix. The goal was to understand the influence of molecular weight, molecular diffusion and nanoparticle content on the velocity of the DA reaction, the cross-linking density, the mechanical properties and the self-healing ability. Therefore P(BMA-co-MiMA$_{0.1}$) was mixed with poly(butyl methacrylate-co-furfuryl methacrylate) [P(BMA-co-FMA$_{0.1}$)], a bifunctional furanyl cross-linker ethane-1,2-diyl difuran-2-carboxylate (BF), the octafunctional cage-like spherosilicate (Q$_8$M$_8$FAE), furfuryl modified silica nanoparticles (FUPTES@SiO$_2$) and P(BMA-co-FMA) grafted from SiO$_2$ nanoparticles. The influence of the length of the grafted

polymeric chains and the ratio of FMA to BMA was also investigated. Figure 15 displays TGA results of three core-shell samples. A mass ratio of 10:1 of monomers to nanoparticles gave a core-shell ratio of 20:80, whereas a ratio of 2:1 resulted in a core-shell ratio of 50:50.
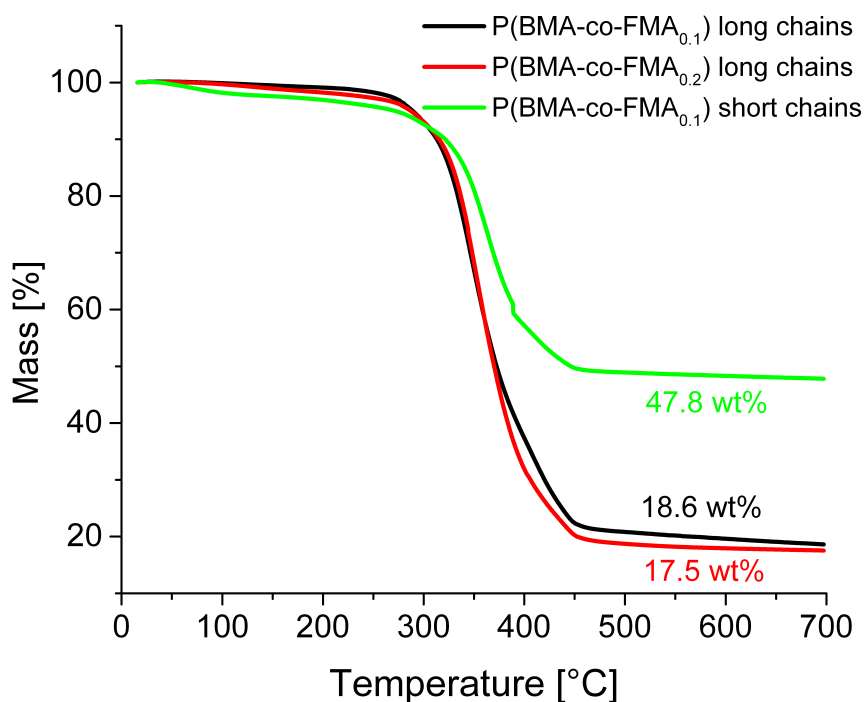

FIGURE 15: TGA RESULTS OF THREE CORE-SHELL NANOPARTICLE SAMPLES WITH VARIOUS CHAIN LENGTHS AND DIFFERENT MONOMER RATIOS.

BF was synthesized by reacting 2-furoyl chloride with ethylene glycol (Scheme 14). FUPTES@SiO_2 was obtained by functionalization of silica nanoparticles with a dienic triethoxysilane previously prepared by reacting furfuryl amine with (3-isocyanatopropyl)triethoxysilane (Scheme 15).
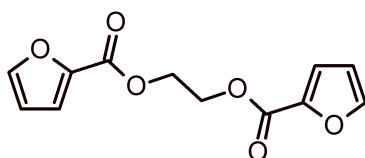
SCHEME 14: BIFUNCTIONAL FURANYL CROSS-LINKER ETHANE-1,2-DIYL DIFURAN-2-CARBOXYLATE (BF).
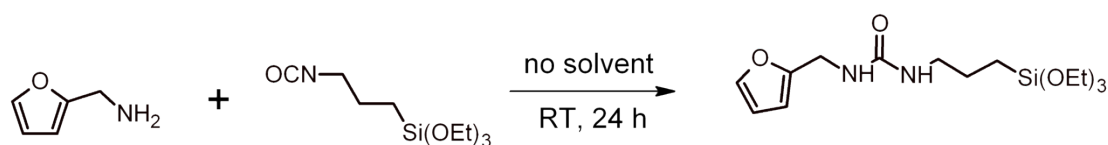
SCHEME 15: SYNTHESIS OF 1-(FURAN-2-YLMETHYL)-3-(TRIETHOXYSILYL)UREA (FUPTES).

In order to facilitate comparison between self-healing materials, a stoichiometric ratio of maleimide to furan was chosen in every case. Table 1 resumes the relative compositions of the different mixtures.

TABLE 3: COMPOSITIONS OF VARIOUS SELF-HEALING MATERIALS CHOSEN FOR COMPARATIVE REASONS, AS WELL AS THE RESULTING PARTICLE CONTENT.

Maleimide component	Weight %	Furan component	Weight %	Particle content (wt%)
P(BMA-co-MiMA$_{0.1}$)	50.0	P(BMA-co-FMA$_{0.1}$)	50.0	0
P(BMA-co-MiMA$_{0.1}$)	87.7	Q$_8$M$_8$FAE$_8$	12.3	3.1
P(BMA-co-MiMA$_{0.1}$)	94.5	BF	5.5	0
P(BMA-co-MiMA$_{0.1}$)	66.7	FUPTES@SiO$_2$	33.3	26
P(BMA-co-MiMA$_{0.1}$)	50.0	P(BMA-co-FMA$_{0.1}$)@SiO$_2$ (long)	50.0	5
P(BMA-co-MiMA$_{0.1}$)	66.7	P(BMA-co-FMA$_{0.2}$)@SiO$_2$ (long)	33.3	3
P(BMA-co-MiMA$_{0.1}$)	24.8	P(BMA-co-FMA$_{0.1}$)@SiO$_2$ (short)	75.2	31

3.4.2.1 UV-Vis experiments

The DA reaction follows second order kinetics in the case of a stoichiometric ratio of furan and maleimide. The conversion of the DA reaction in thin films at 70 °C was followed by UV-Vis studies. The maleimide signal of the polymer matrix could be followed over time. No second order reaction kinetics were observed because the reaction is increasingly slowed down as the cross-linking density increases and the mobility of polymer segments decreases (Figure 16). It could be shown that the reaction was fastest and conversion was highest in the case of the molecular BF and Q$_8$M$_8$FAE$_8$. The SiO$_2$ nanoparticles modified with a short furfuryl-silane did not react because of steric effects and the reaction was stopped after 2 hrs. The polymer-functionalized nanoparticles with high molecular weight polymer chains reacted as

fast as the linear non-grafted polymer. Increase of FMA content within the polymer-grafted nanoparticles slowed the reaction down.
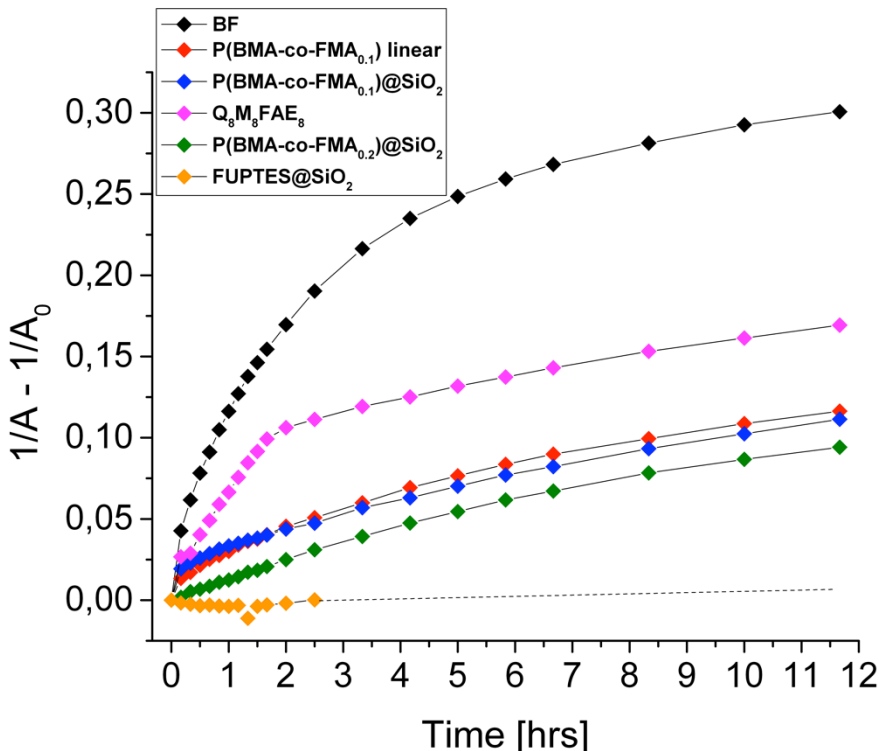

FIGURE 16: UV-VIS EXPERIMENT DISPLAYING THE KINETICS AND EXTENT OF DA REACTION WITHIN MALEIMIDE-MODIFIED POLYMER MATRIX WITH VARIOUS FURAN-CROSS-LINKERS.

These results could only be used to estimate the reaction kinetics and the conversion of the DA reaction, but no conclusion upon the cross-linking density was possible. In the case of the molecular cross-linkers, DA reaction does not automatically form a cross-linked material. If some cross-linkers only react once, only the molecular weight of the polymer chains increases without forming a cross-link. The easiest way to investigate the cross-link density, is to investigate the swelling behaviour of the reaction products after 12 hrs at 70 °C.

3.4.2.2 Swelling behaviour

Swelling of the cross-linked networks in toluene was performed to estimate the cross-linking density. The results are resumed in Table 4. Higher cross-linking density decreases the uptake of solvent within the network. First of all, it could be demonstrated that no network was formed in the case of FUPTES@SiO$_2$, which did also show no DA reaction in the UV-Vis experiment. Interestingly, the reaction with

the bisfunctional furanyl cross-linker BF did also lead to no visible network formation. Apparently, the cross-linker rapidly reacts at one end, leaving the second end unreacted even after 12 hrs at 70 °C. The use of $Q_8M_8FAE_8$ resulted in a highly cured material. Comparison between linear polymers and grafted polymers showed an increase of the apparent cross-linking density with particle content, because the nanoparticles themselves act as additional cross-linking points. The increase of the furfuryl content also increases the cross-linking density, because the polymer segments between two dienes decrease in length.

The Flory-Rehner theory was used to calculate the apparent molecular weight between two cross-links.[107] The theory was established to describe cross-linked polymeric materials but the influence of nanoparticles is not taken into account.

TABLE 4: RESULTS OF SWELLING EXPERIMENTS USING P(BMA-CO-MIMA$_{0.1}$) MATRIX AND VARIOUS CROSS-LINKERS. M_C IS THE APPARENT AVERAGE MOLECULAR WEIGHT BETWEEN CROSS-LINKS, CALCULATED USING THE FLORY-REHNER THEORY.[107]

CROSS-LINKER	SiO$_2$ content (wt%)	SWELLING (%)	M_C (g/mol)
P(BMA-co-FMA$_{0.1}$) linear	0	387	13620
P(BMA-co-FMA$_{0.1}$)@SiO$_2$ long chains	5	356	12190
P(BMA-co-FMA$_{0.2}$)@SiO$_2$ long chains	3	326	8520
P(BMA-co-FMA$_{0.1}$)@SiO$_2$ short chains	30	159	1030
FUPTES@SiO$_2$	25	/	/
BF	0	/	/
Q$_8$M$_8$FAE$_8$	3	260	3470

3.4.2.3   Rheological measurements

Rheological measurements of disc shaped specimens were used to investigate the change of mechanical properties during the DA reaction in previously uncured material. The cured material was then heated from room temperature to 160 °C to see if a change could be observed during RDA reaction. Table 5 resumes the storage and loss moduli obtained after 12 hrs at 70 °C. The polymer matrix P(BMA-co-MiMA$_{0.1}$) is very soft at 70 °C because the glass transition temperature is exceeded by 40 °C. The highest value of the storage modulus was obtained by curing the matrix with linear P(BMA-co-FMA$_{0.1}$), followed by the spherosilicate. Curing with polymer grafted silica nanoparticles yielded different moduli that strongly depended of the amount of FMA within the polymer chains. Lower diene content increases the mechanical properties.

TABLE 5: STORAGE MODULI AND LOSS MODULI OF PURE POLYMER MATRIX AND VARIOUS MIXTURES AFTER DA CURING AT 70 °C FOR 12 HRS.

Material composition	Storage modulus [Pa]	Loss modulus [Pa]
P(BMA-co-MiMA$_{0.1}$)	2,500	5,700
P(BMA-co-MiMA$_{0.1}$) + P(BMA-co-FMA$_{0.1}$)	650,000	900,000
P(BMA-co-MiMA$_{0.1}$) + P(BMA-co-FMA$_{0.1}$)@SiO$_2$	100,000	125,000
P(BMA-co-MiMA$_{0.1}$) P(BMA-co-FMA$_{0.2}$)@SiO$_2$	34,000	39,000
P(BMA-co-MiMA$_{0.1}$) + Q$_8$M$_8$FAE$_8$	110,000	105,000
P(BMA-co-MiMA$_{0.1}$) + FUPTES@SiO$_2$	6,000	5,000
P(BMA-co-MiMA$_{0.1}$) + BF	21,000	18,000
Q$_8$M$_8$FAE$_8$ + Bismaleimide	$> 10^7$	$> 10^6$

P(BMA-co-FMA$_{0.1}$)@SiO$_2$ did allow more DA cross-links than P(BMA-co-FMA$_{0.2}$)@SiO$_2$ by increasing the flexibility of the polymeric chains between two cross-linking points. Low storage modulus of 6000 Pa was measured for the composite containing FUPTES@SiO$_2$, confirming that no DA reaction occurred. The slightly higher modulus compared to pure polymer matrix arose from high particle content of 26 wt%. As mentioned before, the reaction with BF did not result in a cross-linked material as demonstrated by lack of swelling in toluene. Rheology on the other hand, showed an increase of the storage modulus compared to uncured P(BMA-co-MiMA$_{0.1}$). The only explanation would be the experimental circumstances. Apparently the oscillating rotation of the rheometer plates favored cross-linking. Increased movement of the macromolecules increased the probability of a second DA reaction leading to a network formation. Even if curing occurred, the extent of the cross-links were minimal as demonstrated by relatively low storage modulus of 21000 Pa. In addition to the materials based on polymer matrix, the

$Q_8M_8FAE_8$/bismaleimide composite was investigated. The material was first molten at 160 °C to improve contact with the plates. Afterwards, it was slowly cooled down and the storage modulus was recorded. Even at 100 °C the storage modulus had increased drastically up to 10 MPa. Curing was extremely fast and the glassy composite is very tough.

All other materials were investigated a second time after the DA curing. DMA was performed by heating the samples from 40 °C to 160 °C accompanied by recording of the storage modulus. After the initial softening with increasing temperature, a plateau of the storage modulus was reached. Contrary to the uncured samples, all cross-linked materials showed a second softening point arising from RDA reaction. Figure 17 shows the DMA of the P(BMA-co-MiMA$_{0.1}$)/$Q_8M_8FAE_8$ sample. The second softening point was estimated by the intersection of two tangents applied to the curve. All softening points were located in a temperature range between 130 and 140 °C, which fits perfectly with previous findings concerning RDA temperature. Figure 18 shows the DMA of FUPTES@SiO$_2$ cured polymer. No plateau of the storage modulus and no RDA softening point could be observed, which is consistent with low cross-linking density.
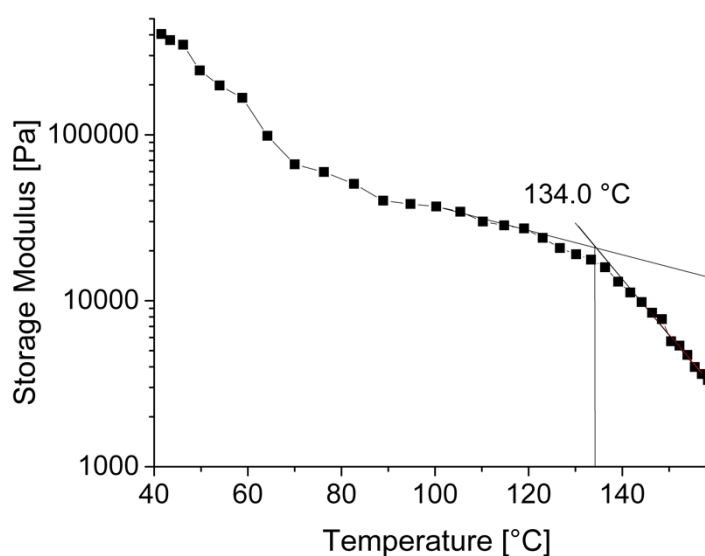
FIGURE 17: DMA EXPERIMENT OF THE P(BMA-CO-MIMA$_{0.1}$)/Q$_8$M$_8$FAE$_8$ SAMPLE. SOFTENING AT 134 °C REVEALS RETRO-DIELS-ALDER REACTION.
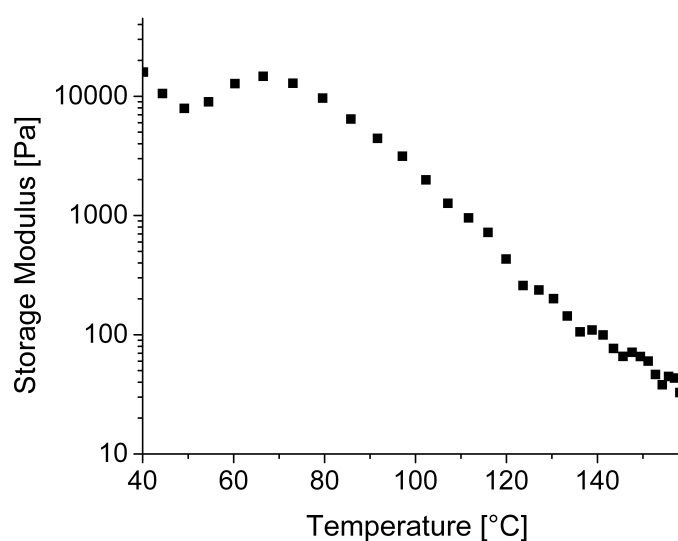

FIGURE 18: DMA EXPERIMENT OF THE P(BMA-CO-MIMA$_{0.1}$)/FUPTES@SIO$_2$ SAMPLE. NO RETRO-DIELS-ALDER REACTION COULD BE OBSERVED.

3.4.2.4 Scratch-healing behavior

In order to investigate the influence of the cross-linking agent on self-healing behavior of the DA cured materials, scratch-healing tests were performed on thin foil samples prepared with a heated press. The scratches were obtained by linear abrasion using constant load. Microscopic images were taken before and after heating to

different temperatures (Figure 19). The heating occurred from both sides of the sample without pressure to avoid flattening by deformation of the sample.
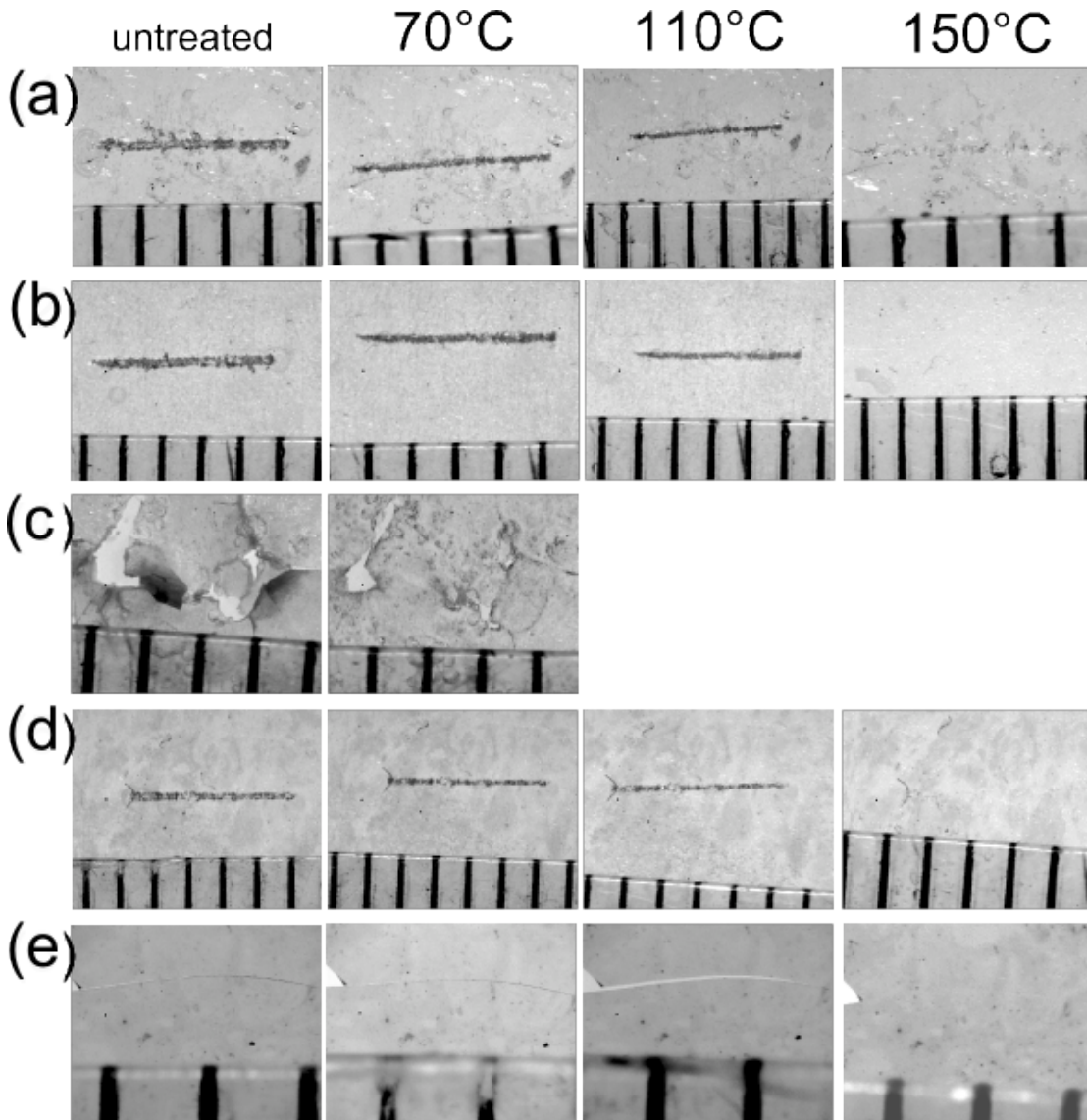

FIGURE 19: SCRATCH-HEALING TEST AT DIFFERENT TEMPERATURES OF (A) P(BMA-CO-MIMA$_{0.1}$)/P(BMA-COFMA$_{0.1}$), (B) P(BMA-CO-MIMA$_{0.1}$)/Q$_8$M$_8$FAE$_8$, (C) P(BMA-CO-MIMA$_{0.1}$)/FUPTES@SIO$_2$, (D) P(BMA-CO-MIMA$_{0.1}$)/P(BMA-COFMA$_{0.1}$)@SIO$_2$ AND (E) Q$_8$M$_8$FAE$_8$/BISMALEIMIDE. THE DISTANCE BETWEEN TWO LINES OF RULER IS EQUAL TO 1 MM.

The sample composed of P(BMA-co-MiMA$_{0.1}$)/P(BMA-co-FMA$_{0.1}$) (a) revealed no change in the shape of the scratch up to a temperature of 110 °C. The scratch disappeared only after the RDA reaction occurred at 150 °C. The same behavior could be observed for (b) P(BMA-co-MiMA$_{0.1}$)/Q$_8$M$_8$FAE$_8$, (d) P(BMA-co-MiMA$_{0.1}$)/P(BMA-co-FMA$_{0.1}$)@SiO$_2$ and (e) Q$_8$M$_8$FAE$_8$/BMI. During abrasion of the latter, the sample cracked, but even the crack could be healed. P(BMA-co-

MiMA$_{0.1}$)/FUPTES@SiO$_2$ ruptured during abrasion because of the brittleness arising from the high particle content. Even at low temperature of 70 °C, closure of a major part of the holes in the surface was observed. This thermoplastic behavior arises from the lack of cross-links within this sample. Again, it could be established that FUPTES@SiO$_2$ is not a suitable cross-linking agent for self-healing materials.

3.5   Conclusion

The preparation of inorganic building blocks suitable for DA based self-healing nanocomposites was successful. Different techniques were investigated and a comparative study was conducted.

Nanoparticles modified with short maleimide- or furan-coupling agents showed characteristic low conversion due to steric surface effects. Approach and overlap of dienes and dienophiles are hindered even in solution. Lower mobility within a polymer matrix further decreases conversion.

Short molecular cross-linker BF showed high reaction rate but no DA curing was observed. Reaction only took place at one end of the cross-linker.

As self-healing polymers based on furan/maleimide interaction have been reported in literature, a nanoparticle-polymer core-shell approach was examined. It could be demonstrated that both a high molecular weight of grafted polymer chains and a low furan content were favorable for high cross-linking density. The reaction rate was comparable to that of non-grafted linear polymers. Swelling experiments in toluene indicated that the nanoparticle cores acted as additional cross-linking points. Rheology showed that the increase of storage modulus is highest with a linear polymer followed by the core-shell nanoparticles with the same BMA/FMA ratio. Increase of furan content decreases cross-linking density as the mobility of chain segments is lowered.

Best suited for the synthesis of a hybrid self-healing nanocomposite is the spherosilicate Q$_8$M$_8$FAE$_8$. DA-curing of maleimide-containing polymer matrix with the cage-like compound was fastest and the obtained cross-linking density was relatively high. The storage modulus reached values higher then in the case of core-shell nanoparticles and the self-healing ability was satisfactory. Furthermore the possibility to use Q$_8$M$_8$FAE$_8$ in combination with low molecular weight cross-linkers

is very interesting. High diffusion rates of both the inorganic compound and the cross-linker resulted in highest DA reaction rate and highest mechanical properties of all combinations tested within this work.

3.6   Experimental Section

3.6.1   Methods

3.6.1.1   Infrared spectroscopy

Fourier transform infrared spectroscopy (FTIR) measurements were performed on a Bruker Vertex 70 spectrometer under ambient air (40 scans at a resolution of 4 cm^{-1}) in attenuated total reflectance (ATR) mode.

3.6.1.2   Thermogravimetric analysis

Thermogravimetric analysis (TGA) were performed on a Netzsch Iris TG 209 C in an alumina crucible heating from room temperature to 700 °C under nitrogen followed by heating to 800 °C under oxygen with a rate of 20 K min^{-1}.

The infrared investigation of the decomposition gases released during TGA experiments was performed on a Bruker Vertex 70 spectometer equipped with a TGIR gas cell with liquid nitrogen cooled MCT (HgCdTe) detector. The gases are carried by 40 mL·s^{-1} nitrogen through a heated transfer line and measured at a resolution of 4 cm^{-1} at 32 scans per spectrum.

3.6.1.3   Specimen preparation

Disc-like specimens for UV-Vis, rheology and scratch-healing experiments were produced with a Specac Atlas manual hydraulic press equipped with a high temperature film maker kit. Films were pressed to a thickness of 50 μm to 250 μm depending on the experiment at 135 °C with a maximum load of 2 tons between two silicon wafers.

3.6.1.4   UV-Vis spectroscopy

UV/Vis spectra were recorded on a Perkin Elmer Lambda 25 UV/Vis spectrometer in transmission mode on a 10 mm quartz flow-through cuvette heated by distilled water to 70 °C. The specimens previously pressed at 135 °C were quenched at room temperature to avoid DA reaction prior to the experiment.

3.6.1.5   Rheology

Rheological measurements of the polymer and composite disc-like specimens were recorded on an Anton Paar Physica MCR 301 rheometer equipped with a CTD 450

convection oven. The prepressed samples were measured in oscillation mode with a frequency of 1 Hz and a displacement of 0.01 % using the PP25 measuring system with 25 mm plate diameter and a plate to plate distance of 0.25 mm.

3.6.1.6 Microscopy

Microscopic images were recorded under polarized light using an Olympus BX60 microscope equipped with a Sony CCD-Iris color camera. The scratches were made by linear abrasion.

3.6.1.7 Linear abrasion

The scratches were made by linear abrasion of the sample films with a Taber Linear Abraser equipped with a conical tungsten carbide tip. The scratch was generated by a single movement at a velocity of 15 cycles per minute under a load of 250 g.

3.6.2 Synthetic procedures

3.6.2.1 Synthesis of 1-(furan-2-ylmethyl)-3-(triethoxysilyl)urea (FUPTES)

A 25 mL Schlenk flask with reflux condenser was dried under vacuum and purged with argon, then 8.93 g (36 mmol) of freshly distilled (3-isocyanatopropyl)-triethoxysilane and 10 mL of dry dichloromethane was added. The mixture was heated to reflux and 4.21 g (43 mmol) of freshly distilled furfurylamine was added drop-wise into the solution and stirred over night. The solvent and excess furfurylamine was removed by vacuum distillation. Yield: 11.71 g (34 mmol, 94.4 %) ^{1}H NMR (CDCl$_3$, 25 °C) δ(ppm) = 0.37 (bt, 2H, C**H$_2$**-Si), 0.97 (t, 9H; EtOSi), 1.35 (m, 2H, CH$_2$-C**H$_2$**-CH$_2$), 2.87 (m, 2H, N-C**H$_2$**), 3.56 (q, 6H, EtOSi), 4.03 (m, 2H, CH$_2$-N), 5.88 (bs, 1H, NH), 6.01 (m, 2H, HC=CH), 6.29 (bs, 1H, NH), 7.05 (bs, 1H, OCH). ^{13}C NMR (CDCl$_3$, 25 °C) δ(ppm) = 7.00 (CH$_2$-Si), 17.54 (EtOSi), 23.15 (CH$_2$-CH$_2$- CH$_2$), 36.44 (N-CH$_2$), 42.12 (CH2-N), 57.57 (EtOSi), 105.45 (C=C), 109.52 (C=C), 140.88(C=C), 152.70 (C=CO), 158.68 (C=O). ^{29}Si (CDCl$_3$, 25°C) δ(ppm) = -45.72. IR (cm^{-1}): 3337 (NH), 3124 (C=C-H), 2974 (CH), 2924 (CH), 2883 (CH), 1680 (C=O), 1630 (C=O), 1568 (NH), 1506 (CN), 1441(C=C), 1389 (C=C), 1166 (Si-OEt), 1101 (Si-OEt), 1074 (Si-OEt), 1010 (Si-C), 954 (Si-C).

3.6.3 Functionalization of silica nanoparticles with FUPTES

A 50 mL glass with air tight lid was filled with 1 g of silica nanoparticles and purged with argon. 20 mL of IBMK was added with a syringe. After heating to 115 °C, 2 g (5.8 mmol) FUPTES was added and the dispersion was stirred for 24 hrs. Afterwards the suspension was cooled to room temperature, and half of the solvent was removed by rotary evaporation. The particles were isolated by centrifugation at 13000 rpm for 10 min. They were washed three times with acetone and dried overnight in a vacuum oven ($\approx$50 mbar) at 80 °C. Yield: 0.95 g. IR (cm^{-1}): 2979 (CH), 2930 (CH), 1685 (C=O), 1640 (C=O), 1446 (C=C), 1369 (C=C), 1055 (SiOSi), 955 (SiOH), 788(SiOSi).

3.6.4 Synthesis of ethane-1,2-diyl difuran-2-carboxylate (BF)

In a dried 100 mL round-bottom Schlenk-flask purged with argon, 3.1 g (0.05 mol) ethylene glycol were mixed with 25.85 g (0.2 mol) diisopropylethylamine. While stirring at 0 °C, 13.05 g (0.1 mol) of 2-furoyl chloride were added slowly. After the addition, the reaction mixture was heated to 50 °C for 2 hrs. The white solid that formed was filtered of and the liquid phase was dissolved in 100 mL of diethylether. The organic phase was washed thrice with a NaHCO$_3$ solution and thrice with water. After drying with MgSO$_4$ the solvent was removed by rotary evaporation until a solid formed. The crude product was purified by washing with propan-2-ol and drying in vacuum. Yield: 5.19 g (0.021 mol; 41.5 %) ^{1}H NMR (CDCl$_3$, 25 °C) δ(ppm) = 4.62 (s, 4H, C**H$_2$**-C**H$_2$**), 6.52 (dd, 2H; C=C), 7.22 (dd, 2H, C=C), 7.60 (dd, 2H, C=C). ^{13}C NMR (CDCl$_3$, 25 °C) δ(ppm) = 62.46 (CH$_2$-CH$_2$), 111.90 (C=C), 118.49 (C=C), 144.20 (C=C), 146.60 (C=C), 158.35 (C=O).

3.6.5 Grafting-from polymerization of poly[(butyl methacrylate)-co-(furfuryl methacrylate)] by ARGET ATRP.

Activators regenerated by electron transfer (ARGET) ATRP was used to generate silica-polymer core-shell nanoparticles with different polymer chain lengths and monomer compositions. Initiator functionalized nanoparticles with 17 wt% initiator content (TGA) were used. BMA, FMA, 50 µL HMTETA, initiator-particles and 5 mL toluene were placed in a Schlenk tube. The contents were degassed by bubbling argon

through the liquid for 10 min. The Schlenk tube was charged with argon and 10 mg (0.05 mmol) $CuBr_2$ was subsequently added. The reaction was started by heating the mixture to 80 °C and adding 100 µL of hydrazine hydrate (50-60 %). Exposing the reaction to air after 3 hrs quenched the polymerization. The samples were purified by precipitating from toluene in methanol. Table 6 summarizes reagent masses used for the preparation of different chain lengths and monomer compositions.

TABLE 6: PARTICLE AND MONOMER COMPOSITION OF REACTION MIXTURE DURING ARGET ATRP.

	Initiator NP	BMA	FMA
P(BMA-co-FMA$_{0.1}$) *long chains*	0.3 g	3 g	0.3 g
P(BMA-co-FMA$_{0.1}$) *short chains*	0.3 mg	0.73 g	0.073 g
P(BMA-co-FMA$_{0.2}$) *long chains*	0.3 mg	3 g	0.6 g

4   SUMMARY

Different strategies for the preparation of self-healing hybrid materials were investigated. DA reaction involving furan and maleimide derivatives was chosen as self-healing mechanism. Surface functionalized silica nanoparticles as well as cage-like spherosilicates were employed as cross-linking agents within a thermoplastic matrix. The goal was to react originally thermoplastic nanocomposites using DA reaction between dienic and dienophilic functional groups, to obtain thermosetting nanocomposites with increased mechanical properties. Typically, thermosetting materials are irreversibly cured and cannot be recycled or reshaped. Additionally, they are prone to suffer under long-term mechanical stresses, because of their increased brittleness. The reversibility of the DA curing process at elevated temperatures, allows breaking up the cross-links by RDA reaction. These DA and RDA cycles provide a reusable, recyclable and self-healing nanocomposite.

In order to investigate the use of inorganic nano-building blocks as cross-linking agents in self-healing materials, silica nanoparticles were chosen as model because of the well-established synthetic procedures.

The Stöber process is a simple sol-gel method to synthesize silica nanoparticles of uniform size and shape. Furthermore, the surface chemistry of SiO_2 nanoparticles is well known and offers many possibilities to apply the desired surface functionalities.

The first step towards self-healing hybrid materials was the synthesis of maleimide coupling agents for the modification of nanosized SiO_2 with a diameter of less than 5 nm. Triethoxysilane was used as anchor group, because of its relatively high stability. APTES, a commercially available precursor was used for the preparation of two different coupling agents. The first, N-((3-triethoxysilyl)propyl)maleimide **1**, was obtained by reacting maleic anhydride with APTES, followed by maleimide formation by catalyzed ring closure. 2-(2,5-dioxo-2,5-dihydro-1H-pyrrol-1-yl)ethyl(3-(triethoxysilyl)propyl)carbamate **2** was formed by reacting DA-protected 2-hydroxethylmaleimide with 3-isocyanato-propyltriethoxysilane. The third coupling agent 1-(4-{[4-(2,5-dioxo-3-{[3-(triethoxysilyl)-propyl]amino}-pyrrolidin-1-yl)-phenyl]methyl}phenyl)-2,5-di-hydro-1H-pyrrole-2,5-dione **3** was prepared by Michael addition of 1,1′-(methylendi-4,1-phenylene)bismaleimide with APTES.

All three coupling agents were used for nanoparticle modification in IBMK as solvent. High dielectric constant of IBMK increases the stability of the particle suspension, while the high boiling point favors surface modification.

The modified particles were characterized by DLS, FTIR spectroscopy and TGA coupled with FTIR. Additionally, elemental analysis was used to calculate surface coverage. $1@SiO_2$, $2@SiO_2$ and $3@SiO_2$ presented surface coverages of 1.2, 0.3 and 1.0 molecules per nm^3, respectively.

The influence of the spacer group between the maleimide and the triethoxysilane on the DA kinetics was investigated by model reactions in solution. Therefore, similar molecules were prepared which did not present the triethoxysilane anchor group. These model maleimides were reacted with furan in excess to simulate first order kinetics. Using UV-Vis spectroscopy, the decrease of the maleimide signal around 300 nm could be detected and a trend in reactivity was observed in the order **1**, **2** and **3**. –M and –I effects of phenyl and oxygen are withdrawing electron density from the maleimide systems, thereby lowering the energy of the LUMO. DA reactivity is increased by the increase of the HOMO/LUMO interaction.

UV-Vis spectroscopy could not be used for kinetic studies on the surface of nanoparticles because of light scattering in the particle suspensions. Thus, FTIR spectroscopy was used to investigate DA reaction between $1@SiO_2$ and furan. Reaction rate constant k was in the same order of magnitude than the respective k for the model reaction in solution. No considerable slowdown was observed on the nanoparticle surface.

TGA results of DA reacted nanoparticles revealed low conversion. Steric effects between closely stacked surface functionalities prevent full conversion. The calculated conversions were 16 %, 37 % and 17 %, respectively. Remarkably, a low surface coverage resulted in a higher DA conversion, which is in agreement with steric surface effects.

As the ultimate goal was to use modified nanoparticles within a polymeric matrix, the previous investigation indicated that short molecular coupling agents were unsuitable as DA conversion was very low, even in solution. A successful DA curing in the solid state requires superior mobility of functional groups by increasing the distance to the surface.

The next logical step in order to create self-healing nanocomposites was surface-initiated ATRP. By using dienophilic and dienic monomers and initiator-modified silica, inorganic-organic core-shell nanoparticles could be confected. The use of a comonomer, allowed tuning glass transition temperature T_g and number of functional groups. BMA was selected because of its relative low T_g. A ratio of 10:1 of BMA to functional monomer was necessary to keep a low T_g and maintain mobility of polymeric chains between cross-links.

Stöber process was used to prepare 42.1 ± 5.4 nm (TEM) SiO_2 nanoparticles. They were modified with previously prepared initiator coupling agent. In order to ensure the formation of a monolayer of initiator molecules, monoethoxysilane was used as anchor group. Additionally, the use of monoethoxysilanes prevents the formation of secondary oligomeric silane networks. Dimeric condensation products remain soluble and can easily removed by washing.

Functional monomers were prepared by reacting methacryloyl chloride with furfuryl alcohol or protected hydroxypropylmaleimide. ATRP was used to prepare both the polymer matrix and the core-shell nanoparticles. $P(BMA\text{-}co\text{-}FMA_{0.1})@SiO_2$ was synthesized in toluene at 90 °C using CuBr and PMDETA. In order to prevent secondary reactions during the preparation of $P(BMA\text{-}co\text{-}pMiMA_{0.1})$ matrix, HMTETA was employed as chelating agent. Lower reaction temperature avoided RDA reaction of the protected maleimide, thereby avoiding polymerization of the maleimide double bond.

DLS, TEM, AFM, FTIR and TGA were used to characterize the core-shell nanoparticles. DLS showed an increase of the hydrodynamic diameter of roughly 200 % and TEM revealed no agglomeration. TGA experiments revealed 68.9 wt% of copolymer. Additionally, molecular weight distributions of grafted polymer chains were obtained after etching of the silica core with hydrofluoric acid. SEC of the liberated macromolecules resulted in a molecular weight of 150,000 g/mol and a PDI of 3.3. Low graft-density of 0.01 chains per nm^2 could be explained by relatively low reactivity and the use of bulky monomers.

$P(BMA\text{-}co\text{-}MiMA_{0.1})$ matrix was obtained after deprotection of the maleimide moieties at temperatures above 100 °C. DSC measurements were used to provide evidence for the RDA reaction. A strong endothermic signal with an onset temperature of 124 °C revealed liberation of furan by RDA reaction. Supporting verification was obtained by FTIR measurements.

Maleimide polymer matrix and furan core-shell nanoparticles were combined by suspension in THF followed by removal of the solvent. The resulting nanocomposite was cured by DA reaction at 80 °C for 24 hrs. During the first heating cycle of DSC measurements, an endothermic RDA peak was observed. Subsequent cooling and reheating showed only minor RDA reaction. This could be explained by slow DA reaction during cooling. Curing by DA reaction could be observed by rheology and UV-Vis spectroscopy of previously uncured composite samples. Increase of storage modulus is accompanied by a decrease of the intensity of maleimide signal at 300 nm. Reversibility of cross-linking reaction was proven by multiple cycles using UV-Vis spectroscopy.

Proof of self-healing ability was gained from scratch healing test. Microscopic images of surface scratches during heating displayed complete closure of the defects at temperatures above RDA reaction.

In the third investigation, cubic spherosilicate cores were modified with dienic functional groups by hydrosilation reaction. Spherosilicates are one of the smallest silica species known. The high solubility of these inorganic building blocks offers analytical advantages as liquid NMR spectroscopy can be used for characterization. Influence of solubility and the resulting increased diffusion rate on DA reaction was investigated.

The octaanion $[(OSiO_{1,5})_8]^{8-}$ served as precursor for the preparation of an octafunctional cross-linker. Hydrolysis followed by controlled condensation of TEOS in methanol/water was used to synthesize the inorganic anion. Tetramethylammonium hydroxide was used as base. Dimethylchlorosilane was employed for endcapping of the cubic structure in a biphasic reaction using petroleum ether as solvent for the silane. In the next step hydrosilation reaction was used to functionalize $Q_8M_8{}^H$ with furfuryl moieties using FAE, which was prepared in advance. FAE was obtained by reacting furfuryl alcohol with allyl bromide in a bulk reaction with potassium hydroxide.

Hydrosilation reaction resulted in an eight-fold modification of the cubic spherosilicate as evidenced by liquid NMR spectroscopy. In addition, FTIR spectroscopy showed no remaining Si-H signal. DLS results confirmed the calculated size of the nano building blocks. Furthermore, in the ESI-FTICR MS spectrum of the product, several peaks corresponded to $Q_8M_8FAE_8$.

As counterpart, two bifunctional maleimide cross-linkers were synthesized. A short stiff molecular cross-linker BMI and an oligomeric flexible siloxane cross-linker M_2-PDMS were prepared for comparison.

DA reaction was confirmed using NMR and FTIR spectroscopy. DSC measurements of previously cured materials revealed higher endothermic RDA reaction of the BMI sample. In addition, cooling and reheating exposed a faster reconnection of the cross-links compared to the M_2-PDMS sample. Higher diffusion rates of the molecular cross-linker were identified as the cause of this effect.

Both hybrid self-healing materials had very different mechanical properties. Curing with the small stiff BMI molecule gave a hard, resistant, glassy solid. M_2-PDMS with its relatively low glass transition temperature gave an elastomeric material.

It could be shown that both materials could be molded using a heated filmmaker press. Broken specimens could be healed and even reshaped by RDA reaction. Additional scratch-healing tests monitored by light microscopy revealed surface smoothening of the BMI-cured sample and complete closure of defects of the M_2-PDMS specimen. The elastomeric nature of the latter was favorable for self-healing abilities.

In order to complete the investigations, a comparative study of all three self-healing strategies was conducted. Spherosilicates $Q_8M_8FAE_8$, P(BMA-co-FMA)@SiO_2 silica-polymer core-shell nanoparticles and surface modified nanoparticles FUPTES@SiO_2 were mixed with P(BMA-co-MiMA$_{0.1}$) matrix in stoichiometric ratio of maleimide and furan. Core-shell nanoparticles were synthesized with two different chain lengths and various BMA to FMA ratio. A short furan coupling agent used to modify SiO_2 nanoparticles was prepared from furfuryl amine and 3-isocyanato-propyltriethoxysilane. In addition to inorganic cross-linkers both a short molecular bisfuran and the furan copolymer P(BMA-co-FMA$_{0.1}$) were prepared.

Various techniques were utilized to characterize the resulting materials. UV-Vis spectroscopy was used to follow DA curing at 70 °C. Fastest reactions were recorded with both molecular cross-linkers BF and $Q_8M_8FAE_8$, where diffusion rates are highest. Polymer and core-shell particles with the same BMA/FMA ratio displayed similar reaction rates. An increased FMA content slowed down DA reaction by decreasing mobility of the polymer chains. Nanoparticles functionalized with short

coupling agents did not perform as cross-linkers. No decrease of maleimide signal could be detected.

Swelling behavior of previously cured samples was used to assess the number of cross-links formed by DA reaction. It could be demonstrated that both BF and FUPTES@SiO$_2$ did not result in enough cross-links to form networks. BF only reacted with one of the dienic functionalities without cross-linking the matrix. Furthermore it could be shown that the highest number of cross-linking points was obtained through high nanoparticle content and by using the spherosilicate cross-linker. The nanoparticles themselves acted as secondary cross-links.

Rheological measurements were used to compare the mechanical properties of uncured polymer matrix with cured samples. The fact that FUPTES@SiO$_2$ did not serve as a cross-linker could be confirmed. Slight increase of storage modulus could be explained by high nanoparticle content. On the other hand, curing with BF resulted in an increased storage modulus. These results were not consistent with UV-Vis or swelling experiments. The oscillating movements of the plates may favor DA reaction during rheology. Furthermore, the results confirmed that lower furan content is beneficial for a high number of cross-links.

DMA from 40 to 160 °C of previously cured samples displayed a second softening domain generated by RDA reaction for all cross-linked materials. This phenomenon could be employed to distinguish the samples with self-healing abilities from the samples without self-healing abilities.

Scratch healing experiments were used for the same goal. It could be demonstrated that all cured samples allowed self-healing of surface defects by RDA reaction. P(BMA-co-MiMA$_{0.1}$)/FUPTES@SiO$_2$ could be melted at low temperatures because of the lack of cross-links.

It was concluded that Q$_8$M$_8$FAE$_8$ was best suited as inorganic cross-linking agent for self-healing nanocomposites. Due to its size, DA-curing was fast and conversion was high.

On the other hand, inorganic-organic core-shell nanoparticles represent a universal technique for the preparation of self-healing nanocomposites. The silica core could be easily be substituted for any other kind of inorganic core.

5 OUTLOOK

The different building blocks investigated in this work were more or less suitable for the preparation of self-healing nanocomposites. The various triethoxysilane coupling agents containing maleimide- and furan-functional groups did not yield usable building blocks for DA reaction because of steric hindrance near the surface of the nanoparticles. The increase of the length of the spacer group between the triethoxysilane anchor group and the DA functionalities may solve this issue. In further investigations it could be envisaged to use longer spacer groups in order to increase the reactivity of the surface functionalities.

Silica nanoparticles were chosen as a model because of the simple synthetic procedures and the uniform size and shape. An exchange of the inorganic core could be useful in order to profit from physical properties of various kinds of inorganic nanoparticles. Magnetite particles would offer the possibility to use hyperthermia as heating mechanism to trigger the DA or RDA reaction. Heat dissipation generated by placing the nanocomposite within an alternating magnetic field would facilitate the application of self-healing material. In the case of self-healing coatings, working with gold nanoparticles would allow to heal surface defect by heating the nanocomposite through light irradiation. Gold nanoparticles efficiently generate heat in the presence of electromagnetic radiation in the near infrared range.

The surface-initiated ATRP technique presented in this work could be easily transferred to many other kinds of inorganic cores, by simply changing the type of anchor group used to attach the initiator. Phosphonic acids are universally suitable for a great number of different metal oxides. Thiols may be employed in the case of many metal nanoparticles and metal sulfides, selenides or tellurides.

6 REFERENCES

[1]   A. A. Griffith, *Philosophical Transactions of the Royal Society of London, A* **1920,** *221*, 163-198.

[2]   T. Stern, *J. Res. Updates Polym. Sci.* **2014,** *3*, 57.

[3]   J. E. Pickett, M. M. Gardner, D. A. Gibson, S. T. Rice, *Polym. Degrad. Stab.* **2005,** *90*, 405.

[4]   K. T. Tan, C. C. White, D. J. Benatti, D. L. Hunston, *Polym. Degrad. Stab.* **2008,** *93*, 648.

[5]   K. T. Tan, C. C. White, D. J. Benatti, D. L. Hunston, *Polym. Degrad. Stab.* **2010,** *95*, 1551.

[6]   I. H. Kalfas, *Neurosurg Focus* **2001,** *10*, E1.

[7]   B. J. Blaiszik, S. L. B. Kramer, S. C. Olugebefola, J. S. Moore, N. R. Sottos, S. R. White, *Annu. Rev. Mater. Res.* **2010,** *40*, 179.

[8]   K. A. Williams, A. J. Boydston, C. W. Bielawski, *J. R. Soc. Interface* **2007,** *4*, 359.

[9]   B. C. K. Tee, C. Wang, R. Allen, Z. Bao, *Nat. Nanotechnol.* **2012,** *7*, 825.

[10]   Y. Li, S. Chen, M. Wu, J. Sun, *Adv. Mater.* **2012,** *24*, 4578.

[11]   X.-F. Wu, A. Rahman, Z. Zhou, D. D. Pelot, S. Sinha-Ray, B. Chen, S. Payne, A. L. Yarin, *J. Appl. Polym. Sci.* **2013,** *129*, 1383.

[12]   L. Zedler, M. D. Hager, U. S. Schubert, M. J. Harrington, M. Schmitt, J. Popp, B. Dietzek, *Mater. Today* **2014,** *17*, 57.

[13]   J. Huang, X. Wu Wear-resistant self-healable rubber-feeling plastic coating material, its production and application method. CN Patent 102146258 A, August 10, **2011**.

[14]   A. S. Rad, E. Binaeian, A. Mirabi, *Asian J. Chem.* **2012,** *24*, 1313.

[15]   B. J. Blaiszik, N. R. Sottos, S. R. White, *Compos. Sci. Technol.* **2008,** *68*, 978.

[16]   E. N. Brown, M. R. Kessler, N. R. Sottos, S. R. White, *J. Microencapsulation* **2003,** *20*, 719.

[17]   A. Bal, G. Guclu, T. B. Iyim, S. Ozgumus, *Polym.-Plast. Technol. Eng.* **2011,** *50*, 990.

REFERENCES

[18]   M. W. Keller, S. R. White, N. R. Sottos, *Adv. Funct. Mater.* **2007,** *17*, 2399.

[19]   L. Yuan, G. Liang, J. Xie, L. Li, J. Guo, *Polymer* **2006,** *47*, 5338.

[20]   S. Cosco, V. Ambrogi, P. Musto, C. Carfagna, *J. Appl. Polym. Sci.* **2007,** *105*, 1400.

[21]   Y. C. Yuan, M. Z. Rong, M. Q. Zhang, J. Chen, G. C. Yang, X. M. Li, *Macromolecules* **2008,** *41*, 5197.

[22]   Y. C. Yuan, M. Z. Rong, M. Q. Zhang, *Polymer* **2008,** *49*, 2531.

[23]   X. Liu, X. Sheng, J. K. Lee, M. R. Kessler, *Macromol. Mater. Eng.* **2009,** *294*, 389.

[24]   S. H. Cho, H. M. Andersson, S. R. White, N. R. Sottos, P. V. Braun, *Adv. Mater.* **2006,** *18*, 997.

[25]   J. D. Rule, E. N. Brown, N. R. Sottos, S. R. White, J. S. Moore, *Adv. Mater.* **2005,** *17*, 205.

[26]   S. R. White, N. R. Sottos, P. H. Geubelle, J. S. Moore, M. R. Kessler, S. R. Sriram, E. N. Brown, S. Viswanathan, *Nature* **2001,** *409*, 794.

[27]   M. Z. Rong, *Adv. Comp. Lett.* **2007,** *16*, 167.

[28]   M. W. Keller, S. R. White, N. R. Sottos, *Polymer* **2008,** *49*, 3136.

[29]   D. S. Xiao, Y. C. Yuan, M. Z. Rong, M. Q. Zhang, *Polymer* **2009,** *50*, 2967.

[30]   M. M. Caruso, B. J. Blaiszik, S. R. White, N. R. Sottos, J. S. Moore, *Adv. Funct. Mater.* **2008,** *18*, 1898.

[31]   M. M. Caruso, D. A. Delafuente, V. Ho, N. R. Sottos, J. S. Moore, S. R. White, *Macromolecules* **2007,** *40*, 8830.

[32]   L. Zhang, Y. Tian, Y. M. Ma, *Adv. Mater. Res.* **2012,** *591-593*, 1143.

[33]   S. M. Bleay, C. B. Loader, V. J. Hawyes, L. Humberstone, P. T. Curtis, *Composites Part A* **2001,** *32A*, 1767.

[34]   J. W. C. Pang, I. P. Bond, *Composites, Part A* **2004,** *36A*, 183.

[35]   J. W. C. Pang, I. P. Bond, *Compos. Sci. Technol.* **2005,** *65*, 1791.

[36]   R. S. Trask, I. P. Bond, *Smart Mater. Struct.* **2006,** *15*, 704.

[37]   G. Williams, R. Trask, I. Bond, *Composites, Part A* **2007,** *38A*, 1525.

[38]   R. S. Trask, G. J. Williams, I. P. Bond, *J. R. Soc. Interface* **2007,** *4*, 363.

[39]   H. R. Williams, R. S. Trask, I. P. Bond, *Compos. Sci. Technol.* **2008,** *68*, 3171.

[40]   K. S. Toohey, N. R. Sottos, J. A. Lewis, J. S. Moore, S. R. White, *Nat. Mater.* **2007,** *6*, 581.

[41]   K. S. Toohey, N. R. Sottos, S. R. White, *Exp. Mech.* **2009,** *49*, 707.

[42] S. Kim, S. Lorente, A. Bejan, *J. Appl. Phys.* **2006,** *100*, 063525/1.

[43] H. Zhang, S. Lorente, A. Bejan, *J. Appl. Phys.* **2007,** *101*, 094904/1.

[44] K. M. Wang, S. Lorente, A. Bejan, *J. Phys. D Appl. Phys.* **2006,** *39*, 3086.

[45] A. M. Peterson, H. Kotthapalli, M. A. M. Rahmathullah, G. R. Palmese, *Compos. Sci. Technol.* **2012,** *72*, 330.

[46] S. A. Hayes, F. R. Jones, K. Marshiya, W. Zhang, *Composites, Part A* **2007,** *38A*, 1116.

[47] X. Luo, R. Ou, D. E. Eberly, A. Singhal, W. Viratyaporn, P. T. Mather, *ACS Appl. Mater. Interfaces* **2009,** *1*, 612.

[48] X. Chen, M. A. Dam, K. Ono, A. Mal, H. Shen, S. R. Nut, K. Sheran, F. Wudl, *Science* **2002,** *295*, 1698.

[49] X. Chen, F. Wudl, A. K. Mal, H. Shen, S. R. Nutt, *Macromolecules* **2003,** *36*, 1802.

[50] S. D. Bergman, F. Wudl, *J. Mater. Chem.* **2008,** *18*, 41.

[51] D. Y. Wu, S. Meure, D. Solomon, *Progress in Polymer Science* **2008,** *33*, 479.

[52] K. Jud, H. H. Kausch, *Polym. Bull.* **1979,** *1*, 697.

[53] P. G. d. Gennes, *The Journal of Chemical Physics* **1971,** *55*, 572.

[54] M. Doi, S. F. Edwards, *J. Chem. Soc., Faraday Trans. 2* **1978,** *74*, 1789.

[55] R. P. Wool, K. M. O'Connor, *J. Appl. Phys.* **1981,** *52*, 5953.

[56] I. A. Rousseau, *Polym. Eng. Sci.* **2008,** *48*, 2075.

[57] A. Lendlein, S. Kelch, *Angew. Chem., Int. Ed.* **2002,** *41*, 2034.

[58] A. Lendlein, A. M. Schmidt, M. Schroeter, R. Langer, *J. Polym. Sci., Part A Polym. Chem.* **2005,** *43*, 1369.

[59] E. D. Rodriguez, X. Luo, P. T. Mather, *ACS Appl. Mater. Interfaces* **2011,** *3*, 152.

[60] O. Diels, K. Alder, *Justus Liebigs Ann. Chem.* **1928,** *460*, 98.

[61] M. A. Tasdelen, *Polym. Chem.* **2011,** *2*, 2133.

[62] A. J. Inglis, L. Nebhani, O. Altintas, F. G. Schmidt, C. Barner-Kowollik, *Macromolecules* **2010,** *43*, 5515.

[63] A. J. Inglis, S. Sinnwell, M. H. Stenzel, C. Barner-Kowollik, *Angew. Chem., Int. Ed.* **2009,** *48*, 2411.

[64] E. B. Murphy, E. Bolanos, C. Schaffner-Hamann, F. Wudl, S. R. Nutt, M. L. Auad, *Macromolecules* **2008,** *41*, 5203.

[65] H. Staudinger, H. A. Bruson, *Justus Liebigs Ann. Chem.* **1926,** *447*, 110.

REFERENCES

[66]   J. K. Stille, L. Plummer, *J. Org. Chem.* **1961,** *26*, 4026.

[67]   M. Miura, F. Akutsu, T. Usui, Y. Ikebukuro, K. Nagakubo, *Makromol. Chem.* **1985,** *186*, 473.

[68]   J. P. Kennedy, K. F. Castner, *J. Polym. Sci., Polym. Chem. Ed.* **1979,** *17*, 2039.

[69]   M. P. Stevens, A. D. Jenkins, *J. Polym. Sci., Polym. Chem. Ed.* **1979,** *17*, 3675.

[70]   S. A. Canary, M. P. Stevens, *J. Polym. Sci., Part A Polym. Chem.* **1992,** *30*, 1755.

[71]   F. Wudl, X. Chen, Thermally re-mendable crosslinked polymers, monomers, their manufacture, and thermally mending. US Patent 20040014933, January 22, **2004**.

[72]   M. Wouters, E. Craenmehr, K. Tempelaars, H. Fischer, N. Stroeks, J. van Zanten, *Prog. Org. Coat.* **2009,** *64*, 156.

[73]   A. A. Kavitha, N. K. Singha, *J. Polym. Sci., Part A Polym. Chem.* **2007,** *45*, 4441.

[74]   P. M. Kazmaier, K. A. Moffat, M. K. Georges, R. P. N. Veregin, G. K. Hamer, *Macromolecules* **1995,** *28*, 1841.

[75]   Y. Higaki, H. Otsuka, A. Takahara, *Macromolecules* **2006,** *39*, 2121.

[76]   F. Wang, M. Z. Rong, M. Q. Zhang, *J. Mater. Chem.* **2012,** *22*, 13076.

[77]   C. e. Yuan, M. Z. Rong, M. Q. Zhang, Z. P. Zhang, Y. C. Yuan, *Chem. Mater.* **2011,** *23*, 5076.

[78]   Y. Higaki, H. Otsuka, A. Takahara, *Macromolecules* **2004,** *37*, 1696.

[79]   H. Otsuka, K. Aotani, Y. Higaki, Y. Amamoto, A. Takahara, *Macromolecules* **2007,** *40*, 1429.

[80]   H. M. Klukovich, Z. S. Kean, S. T. Iacono, S. L. Craig, *J. Am. Chem. Soc.* **2011,** *133*, 17882.

[81]   R. E. Banks, B. E. Smart, J. C. Tatlow, Editors, *Organofluorine Chemistry: Principles and Commercial Applications*. **1994**, p 644 pp.

[82]   D. Wu, J. M. Lenhardt, A. L. Black, B. B. Akhremitchev, S. L. Craig, *J. Am. Chem. Soc.* **2010,** *132*, 15936.

[83]   A. M. Peterson, R. E. Jensen, G. R. Palmese, *Compos. Sci. Technol.* **2011,** *71*, 586.

[84]   N. Kwok, H. T. Hahn, *J. Compos. Mater.* **2007,** *41*, 1635.

[85]   B. J. Adzima, C. J. Kloxin, C. N. Bowman, *Adv. Mater.* **2010,** *22*, 2784.

[86]   Q. Tian, M. Z. Rong, M. Q. Zhang, Y. C. Yuan, *Polym. Int.* **2010,** *59*, 1339.

[87]   G. Pallares, L. Ponson, A. Grimaldi, M. George, G. Prevot, M. Ciccotti, *Int. J. Fract.* **2009,** *156*, 11.

[88]   C. Janssen, *Int. Congr. Glass, 10th,* **1974,** *10*, 23.

[89]   J. F. Brown, Jr., L. H. Vogt, Jr., A. Katchman, J. W. Eustance, K. M. Kiser, K. W. Krantz, *J. Am. Chem. Soc.* **1960,** *82*, 6194.

[90]   Y. Abe, H. Hatano, T. Gunji, *J. Polym. Sci., Part A Polym. Chem.* **1995,** *33*, 751.

[91]   N. Yamazaki, S. Nakahama, J. Goto, T. Nagawa, A. Hirao, *Contemp. Top. Polym. Sci.* **1984,** *4*, 105.

[92]   R. H. Baney, M. Itoh, A. Sakakibara, T. Suzuki, *Chem. Rev.* **1995,** *95*, 1409.

[93]   Y. Kaneko, M. Shoiriki, T. Mizumo, *J. Mater. Chem.* **2012,** *22*, 14475.

[94]   S. Lucke, K. Stoppek-Langner, *Appl. Surf. Sci.* **1999,** *144-145*, 713.

[95]   P. A. Agaskar, *Inorg. Chem.* **1991,** *30*, 2707.

[96]   A. Sellinger, R. M. Laine, *Macromolecules* **1996,** *29*, 2327.

[97]   Z. Xu, Y. Zhao, X. Wang, T. Lin, *Chem. Commun.* **2013,** *49*, 6755.

[98]   D. Hoebbel, W. Wieker, *Z. Anorg. Allg. Chem.* **1971,** *384*, 43.

[99]   M. Z. Asuncion, I. Hasegawa, J. W. Kampf, R. M. Laine, *J. Mater. Chem.* **2005,** *15*, 2114.

[100]   I. Hasegawa, S. Sakka, Y. Sugahara, K. Kuroda, C. Kato, *J. Chem. Soc., Chem. Commun.* **1989**, 208.

[101]   I. Hasegawa, S. Motojima, *J. Organomet. Chem.* **1992,** *441*, 373.

[102]   D. Holzinger, G. Kickelbick, *J. Polym. Sci., Part A Polym. Chem.* **2002,** *40*, 3858.

[103]   R. O. R. Costa, W. L. Vasconcelos, R. Tamaki, R. M. Laine, *Macromolecules* **2001,** *34*, 5398.

[104]   J. Pyun, K. Matyjaszewski, T. Kowalewski, D. Savin, G. Patterson, G. Kickelbick, N. Huesing, *J. Am. Chem. Soc.* **2001,** *123*, 9445.

[105]   T. Pintauer, U. Reinoehl, M. Feth, H. Bertagnolli, K. Matyjaszewski, *Eur. J. Inorg. Chem.* **2003**, 2082.

[106]   S. Faucher, P. Okrutny, S. Zhu, *Ind. Eng. Chem. Res.* **2007,** *46*, 2726.

[107]   N. Mignard, N. Okhay, C. Jegat, M. Taha, *J. Polym. Res.* **2013,** *20*, 1.

7 ACKNOWLEDGEMENTS

8   SUPPORTING INFORMATION

Thermoreversible Reactions on Inorganic Nanoparticle Surfaces – Diels–Alder Reactions on Sterically Crowded Surfaces

Tom Engel, Guido Kickelbick*

* Saarland University, Inorganic Solid State Chemistry, Am Markt Zeile 3, 66125 Saarbrücken
Email: kickelbick@mx.uni-saarland.de

1.   Transmission electron microscopy (TEM)
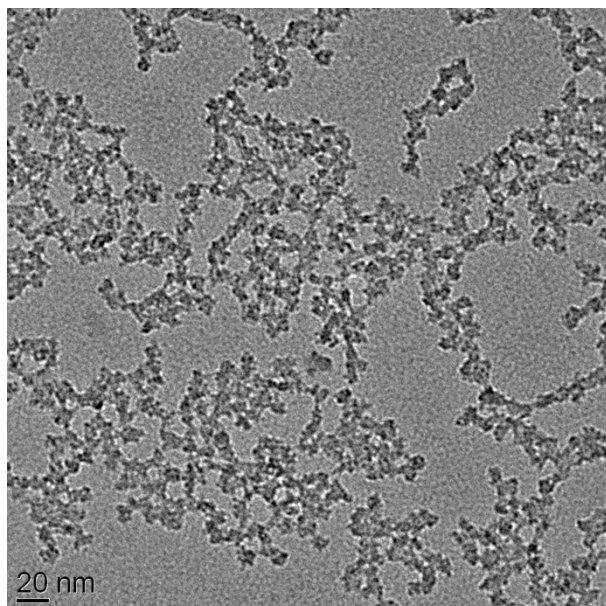
Figure S10: TEM image of prepared silica nanoparticles.
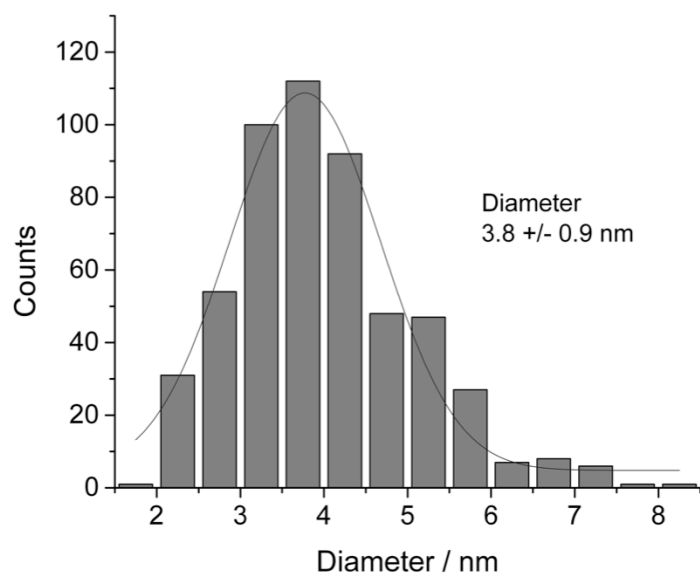
Figure S11: TEM size distribution histogram.

2. FTIR Analysis
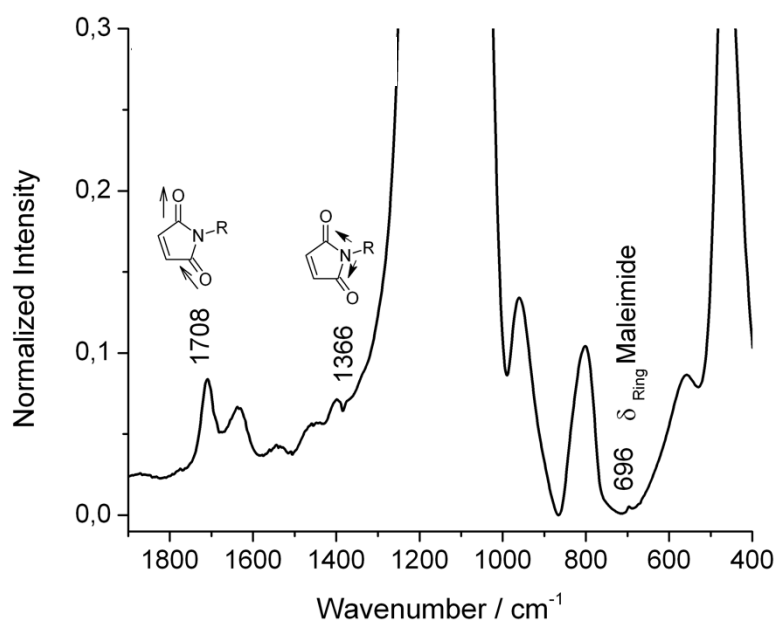
Figure S3: IR Spectrum of 2@SiO$_2$.
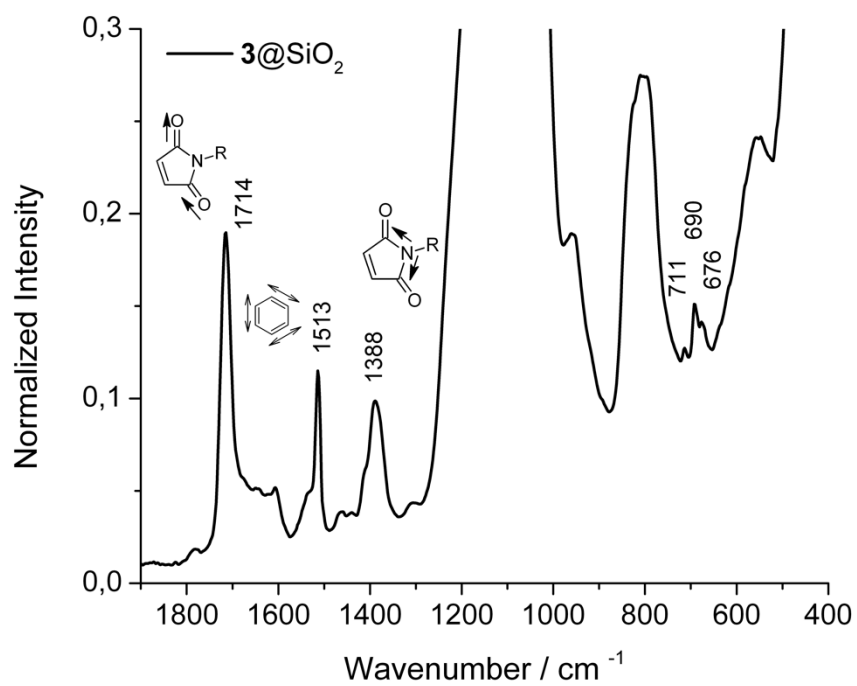
Figure S4: IR Spectrum of BMPTES@SiO$_2$.

2. TGA coupled with FTIR
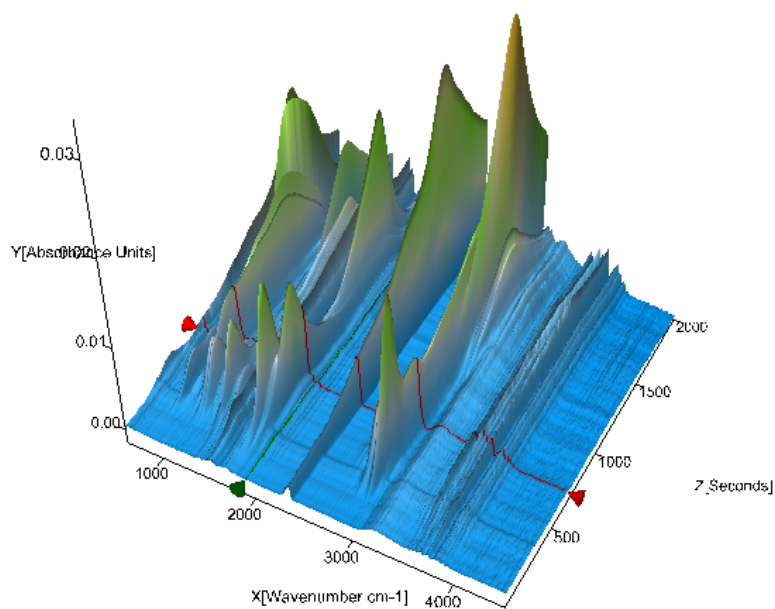
Figure S5: TGA/FTIR 3D-plot of **1**@SiO$_2$.
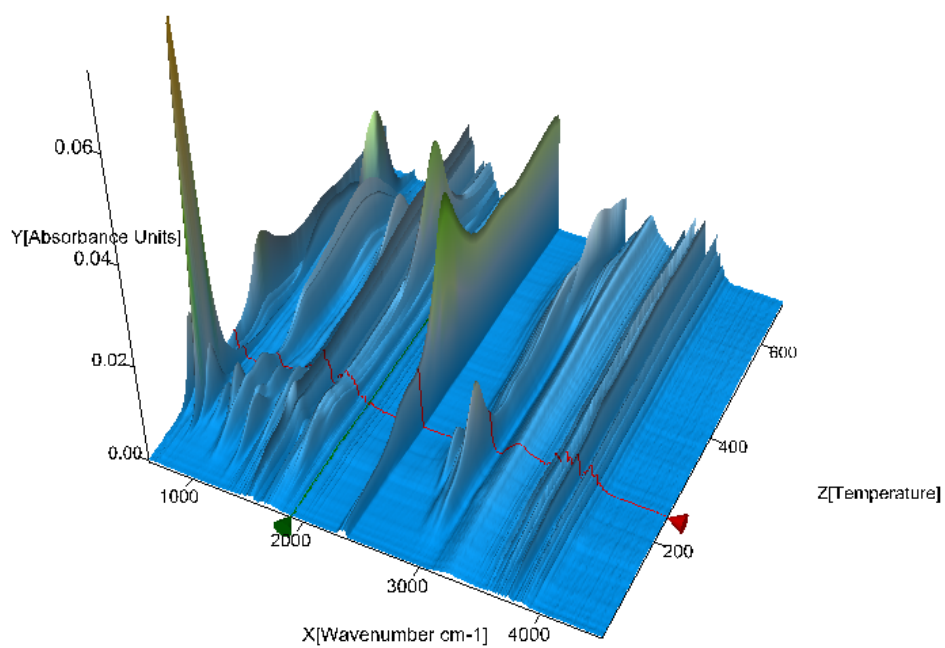
Figure S6: TGA/FTIR 3D-plot of **2**@SiO$_2$.
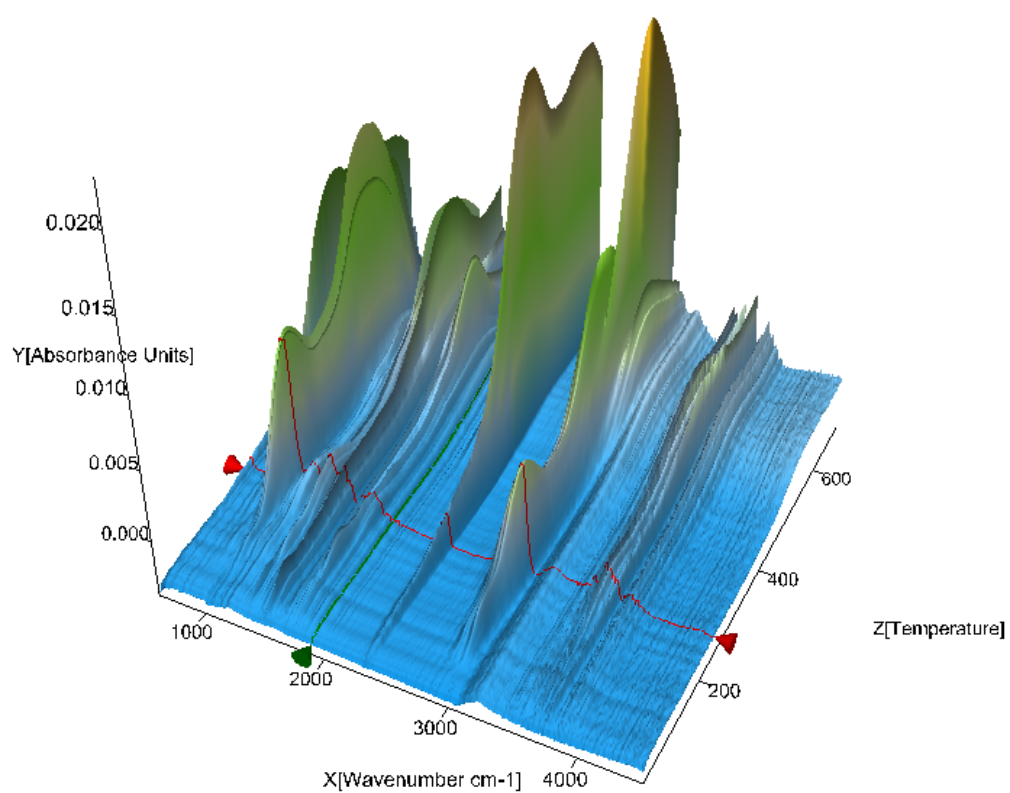
Figure S7: TGA/FTIR 3D-plot of **3**@SiO$_2$.

3. Diels-Alder Reaction on the particle surface
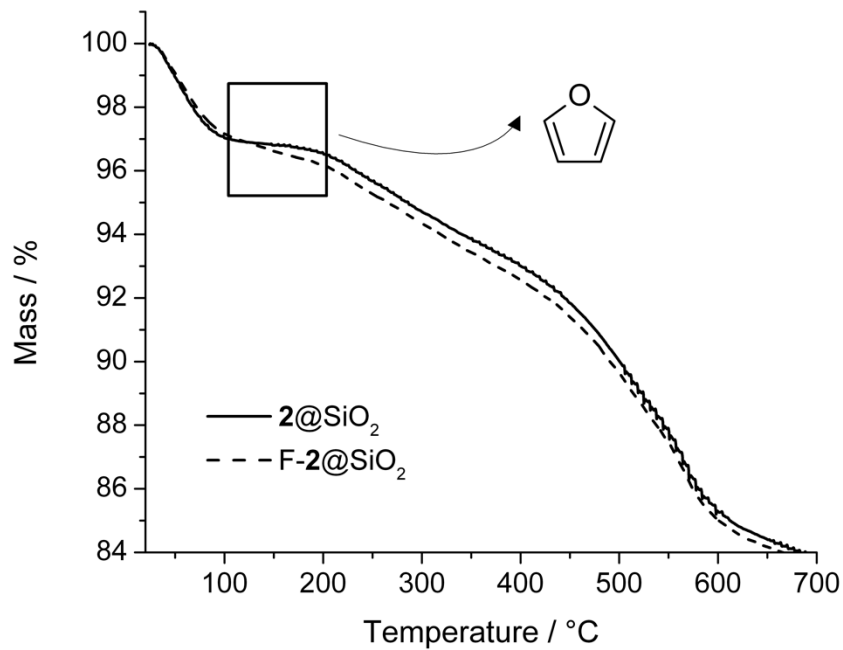
Figure S8: Comparison of TGA measurements of F-**2**@SiO$_2$ and **2**@SiO$_2$ after retro-DA reaction at 150°C.
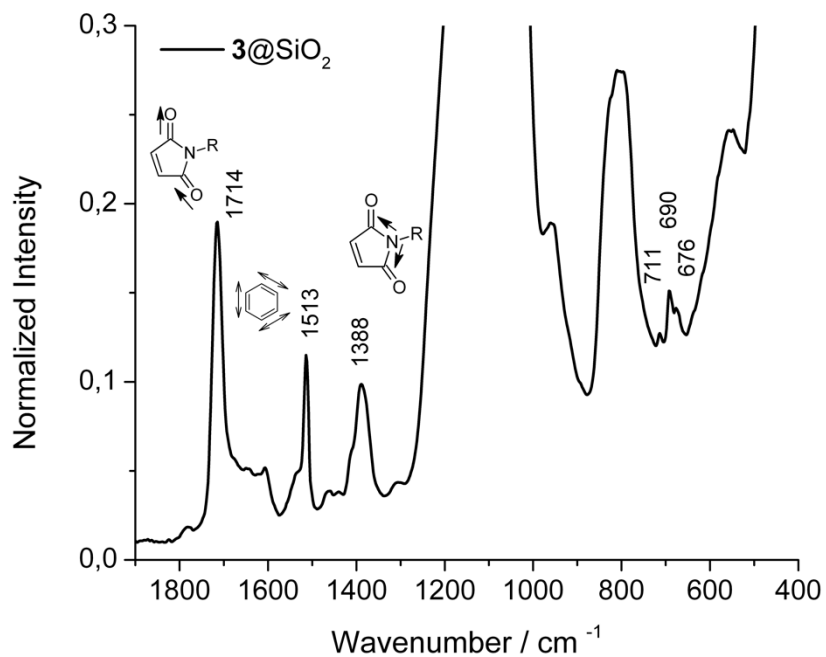
Figure S9: Comparison of TGA measurements of F-**3**@SiO$_2$ and **3**@SiO$_2$ after retro-DA reaction at 150°C.

4. Kinetic Studies of Model Compounds
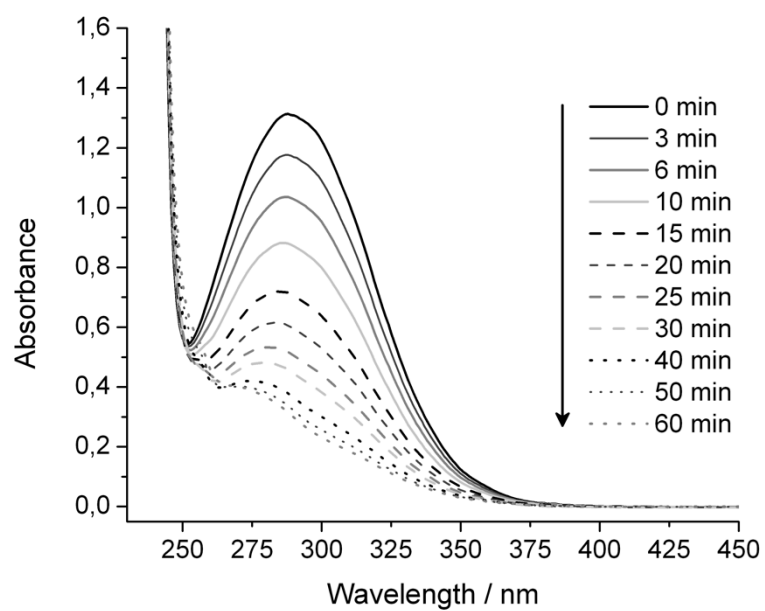
Figure S10: UV-Vis Spectra of N-Propylmaleimide **M1** at different time intervals during the DA reaction with dimethylfuran at 60°C.
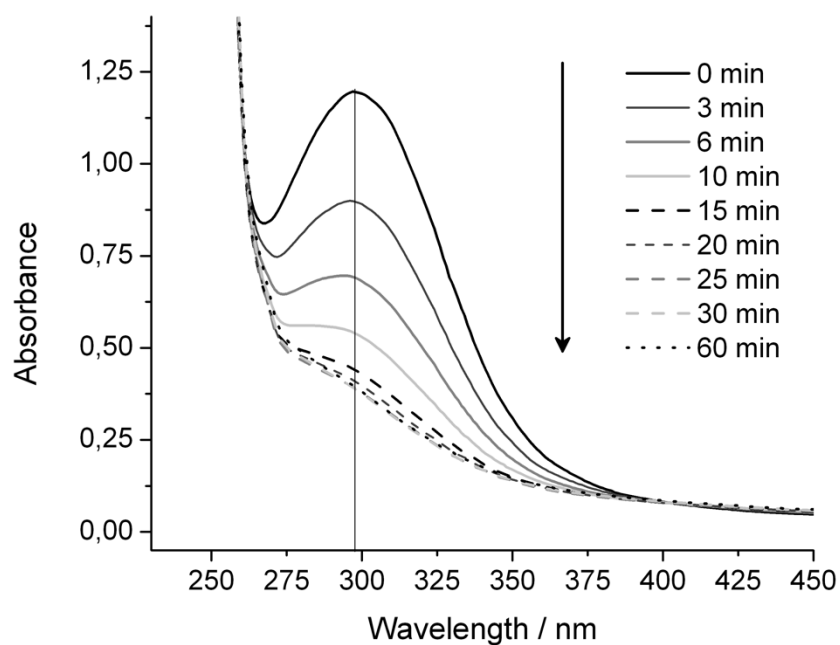
Figure S11: UV-Vis Spectra of N-ethyl(N-propylcarbamato)maleimide **M2** at different time intervals during the DA reaction with dimethylfuran at 60°C.
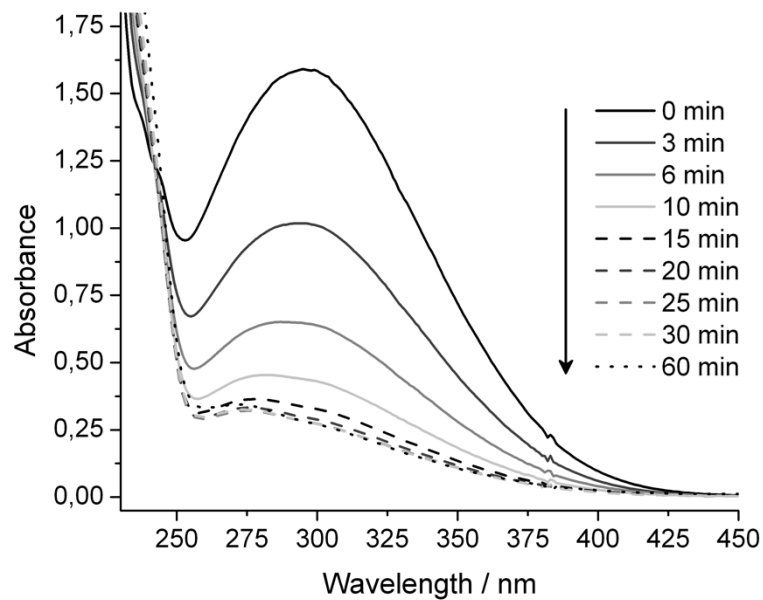
Figure S12: UV-Vis Spectra of N-Phenylmaleimide **M3** at different time intervals during the DA reaction with dimethylfuran at 60°C.
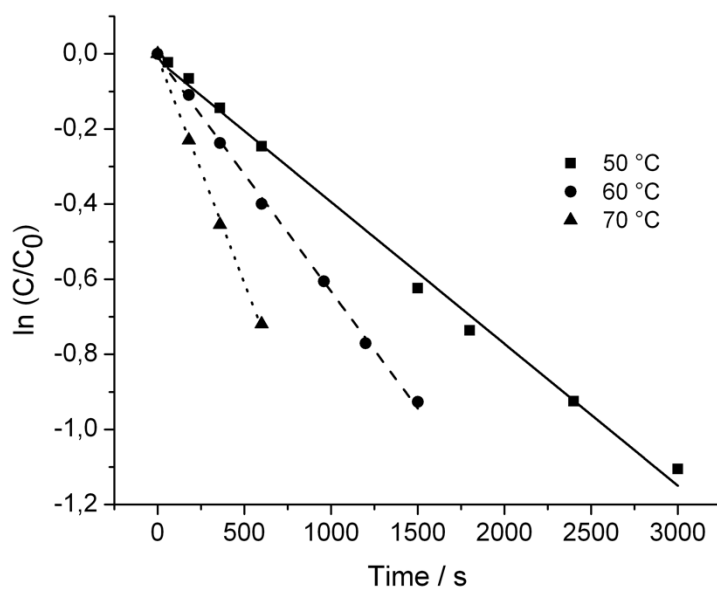
Figure S13: Logarithm of conversion over time of N-Propylmaleimide **M1** at different temperatures.
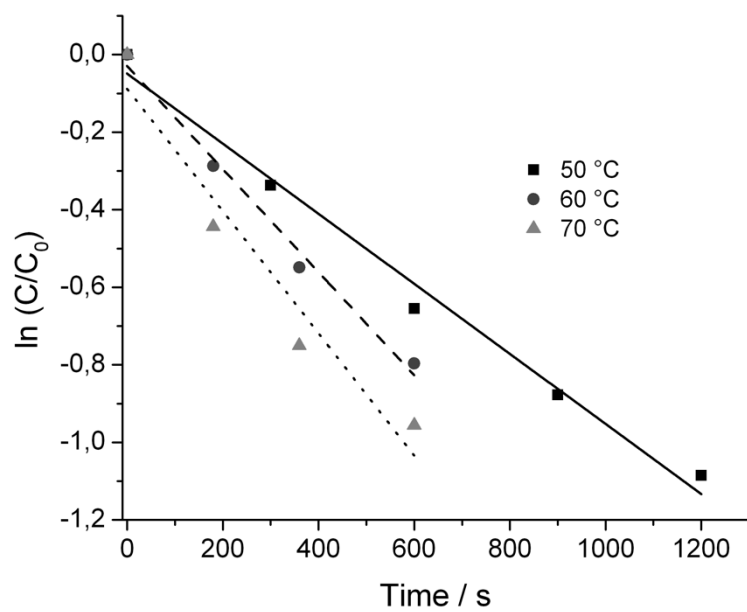
Figure S14: Logarithm of conversion over time of N-ethyl(N-propylcarbamato)maleimide **M2** at different temperatures.
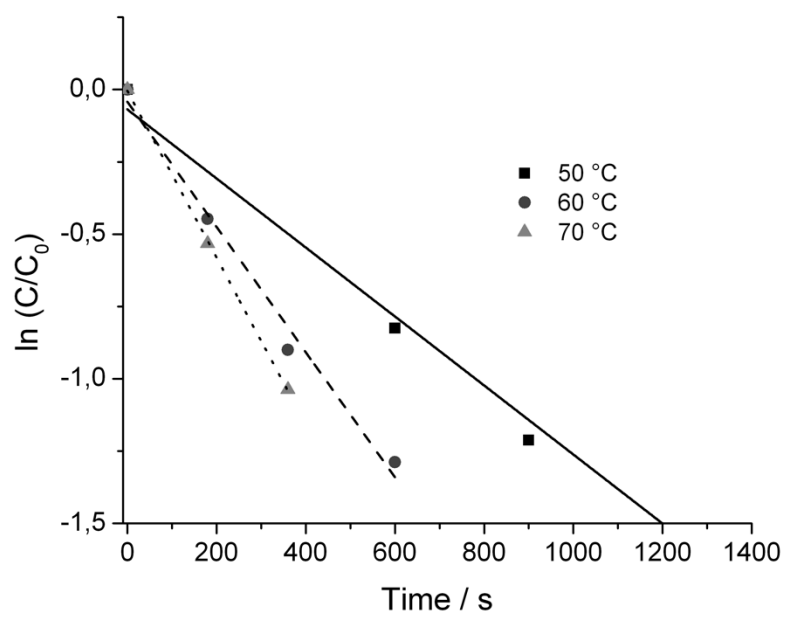
Figure S15: Logarithm of conversion over time of N-Phenylmaleimide **M3** at different temperatures.

Self-healing nanocomposites from silca-polymer core-shell nanoparticles

Tom Engel and Guido Kickelbick*

Inorganic Solid State Chemistry, Saarland University, Am Markt Zeile 3, 66125 Saarbrücken, Germany

SUPPORTING INFORMATION

Synthesis of Protected Maleic Anhydride – 3,6-Epoxy-1,2,3,6-tetrahydrophthalic Anhydride 1.

The synthesis was carried out following a modified literature procedure. In a 1 L three-neck round-bottom flask under argon atmosphere. 100 g (1.02 mol) of the maleic anhydride and 81.69 g (1.2 mol) of furan were dissolved in 500 mL of toluene. The mixture was stirred for 3 days at room temperature. A white precipitate formed during this time. The solid was collected by filtration and washed two times with cold diethyl ether. The filtrate was reduced by rotary evaporation to 80 mL and cooled to 4 °C overnight. A second crop crystallized, which was again collected by filtration and washed with diethyl ether. Finally, the crystals were dried in vacuum ($\approx$10−2 mbar) overnight. Yield: 151.65 g (0.913 mol; 89.5%).

^{1}H NMR (CDCl$_3$, 25 °C) δ ppm 3.01 (s, 2 H), 5.40 (s, 2 H), 6.57 (s, 2 H). ^{13}C NMR (CDCl$_3$, 25 °C) δ ppm 47.52 (CH), 81.40 (CHO), 136.67 (C=C), 175.29 (C=O).

IR (cm^{-1}): 3143 (2x C=C), 3099 (=C-H), 3089, 3066, 3033, 3000, 2991, 1857 (sym C=O), 1780 (asym C=O), 1309, 1282, 1230, 1211, 1193, 1145, 1083, 1018, 948, 921, 902, 877, 848, 821. Onset of decomposition (DSC, N$_2$, 15 K min^{-1}): 117.9 °C.

Elemental analysis (%): Calcd for C8H6O4: C 57.84, H 3.64, N 0.00; Found: C 56.75, H 3.71, N 0.00.

Synthesis of Protected (3-Hydroxypropyl)maleimide – 4-(3-hydroxypropyl)-10-oxa-4-azatricyclo[5.2.1.0²,⁶]dec-8-ene-3,5-dione 2.

In a 2 L reactor with double jacket heating and mechanical stirrer, reflux condenser and dropping funnel, 100 g (0.6019 mol) protected maleic anhydride were suspended in 2 L MeOH. 45.21 g (0.602 mol) 3-Aminopropan-1-ol were added drop wise and stirred at RT until all adducts were dissolved. The mixture was heated to reflux (57 °C) for 3 days. The solvent was removed in vacuum. The yellowish oil was dissolved in 500 mL of chloroform and washed 3 times with 200 mL of water. The organic layer was dried over sodium sulfate and concentrated in vacuum. Yield: 32.3 g (0.144 mol; 24.0 %)

^{1}H NMR (CDCl$_3$, 25 °C) δ ppm 1.78 (qt, J = 6.00 Hz, 2 H), 2.88 (s, 2 H), 3.53 (t, J = 6.00 Hz, 2 H), 3.66 (t, J = 6.00 Hz, 2 H), 5.28 (s, 2 H), 6.53 (s, 2 H). ^{13}C NMR (CDCl$_3$, 25 °C) δ ppm 30.32 (CH$_2$), 35.16 (CH$_2$N), 47.48 (CH), 58.63 (CH$_2$O), 80.96 (CHO), 136.51 (C=C), 176.94 (C=O).

IR (cm^{-1}): 3507 (OH), 3095 (=C-H), 3008 (=C-H), 2947 (C-H), 2874 (C-H), 1766 (sym C=O), 1689 (asym C=O), 1435, 1155, 1019, 878, 851. Elemental analysis (%): Calcd for C$_{11}$H$_{13}$O$_4$N: C 59.19, H 5.87, N 6.27; Found: C 57.71, H 5.80, N 5.98.

Synthesis of silica nanoparticles

The silica nanoparticles were synthesized according to a modified literature procedure. In a 2 L round-bottom flask, ethanol (1500 mL) was mixed with 45 mL of 25% ammonia and 30 mL of water and stirred for 10 min. Then 170 mL of TEOS were added. The solution was stirred for 1 days, and a part of the particles was isolated to characterize the unmodified sample. Part of the solvent was removed and and the particles were isolated and washed three times with ethanol by centrifugation at 13000 rpm and dried overnight in a vacuum oven (≈50 mbar) at 60 °C. Yield: 45 g

silica particles; TEM: diameter 42 ± 5.4 nm; DLS: diameter 44.8 ± 0.4 nm; surface

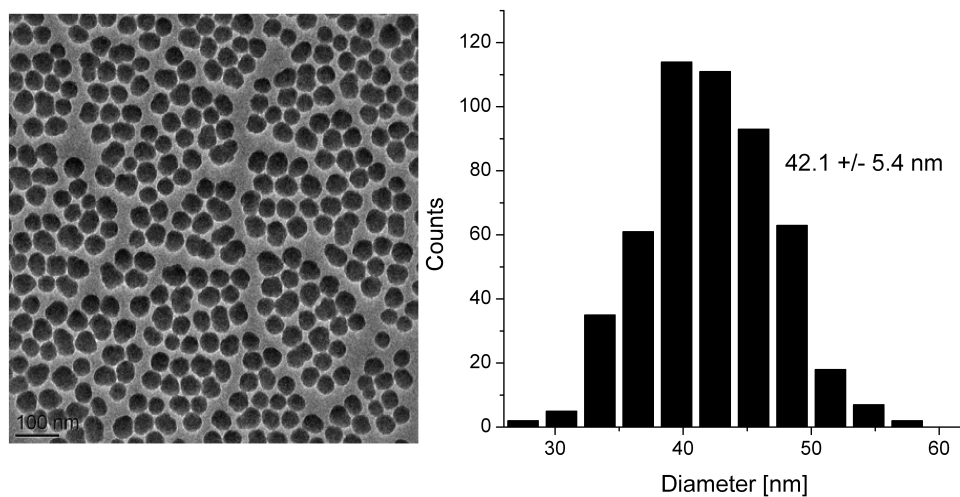area: BET 306 m^2 g^{-1}.

FIGURE S1: TEM IMAGE OF BARE SILICA AND THE CORRESPONDING
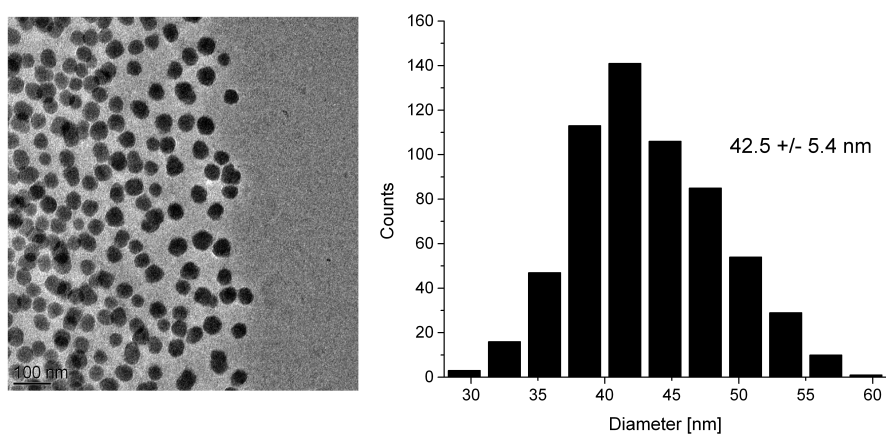
HISTOGRAM WITH DETERMINED AVERAGE DIAMETER.

Figure S2: TEM image of PBMA-co-FMA grafted silica and the corresponding histogram
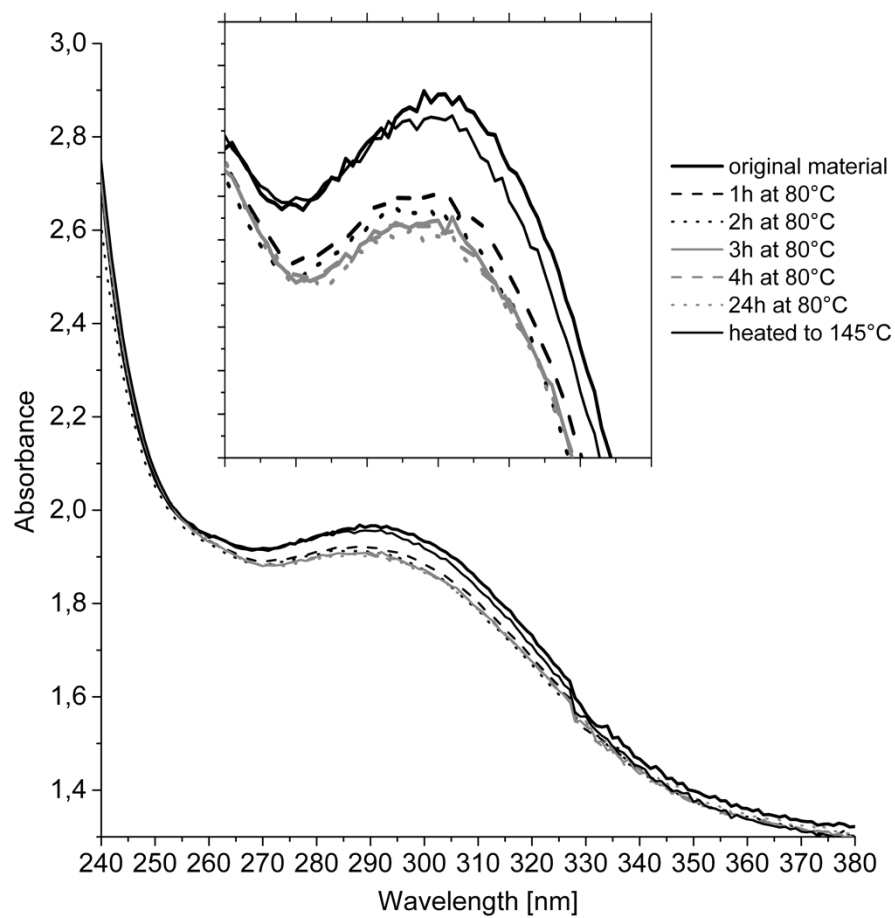
with determined average diameter.

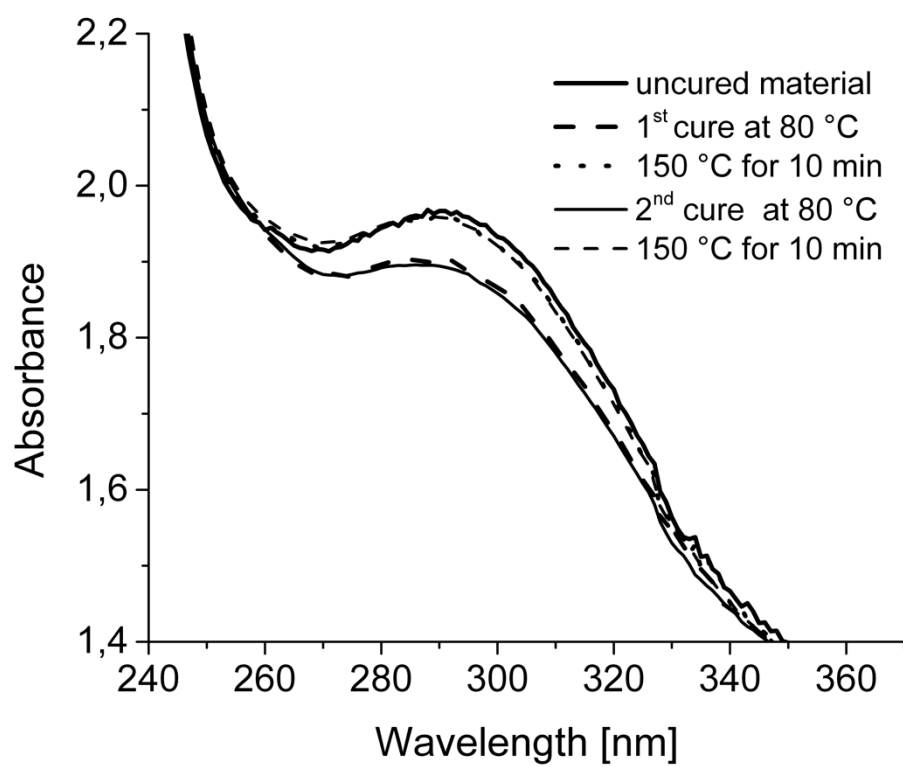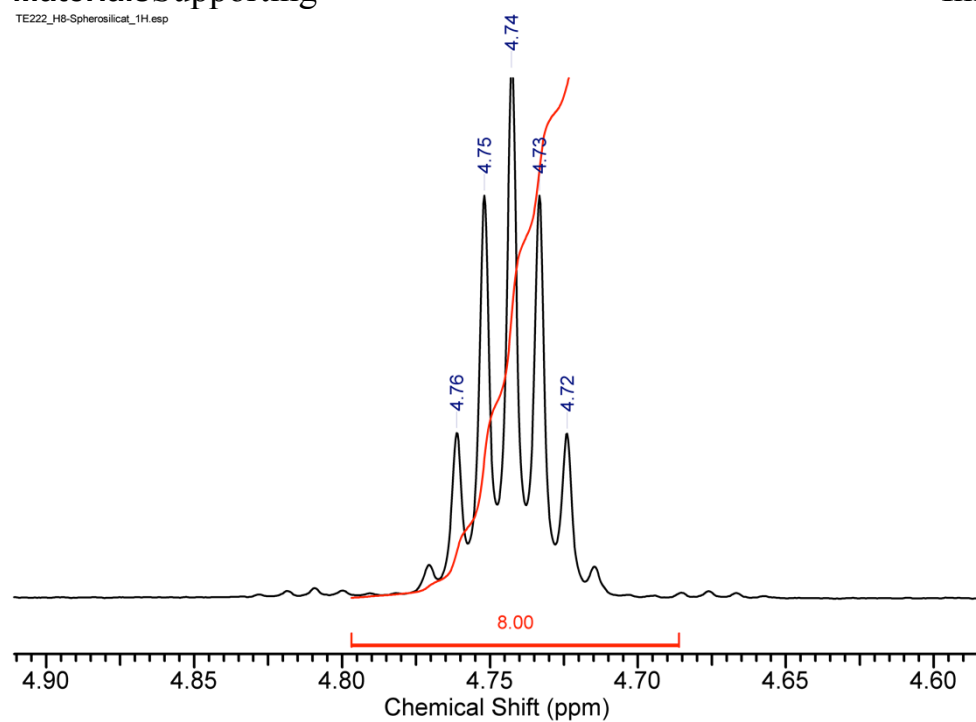Figure S3: UV/Vis spectra during curing of P(BMA-*co*-MiMA) with P(BMA-*co*-FMA)@SiO$_2$.

Figure S4: UV/Vis spectra of multiple curing cycles.

Furan-Modified Spherosilicates as Building Blocks for Self-Healing Materials Supporting   Information

Figure SI1: ^{1}H NMR of $Q_8M_8^H$.

Figure SI2: 1H NMR of $Q_8M_8^H$.

TE222_H8-Spherosilicat_29Si.esp

-1.88

-109.03

Chemical Shift (ppm)
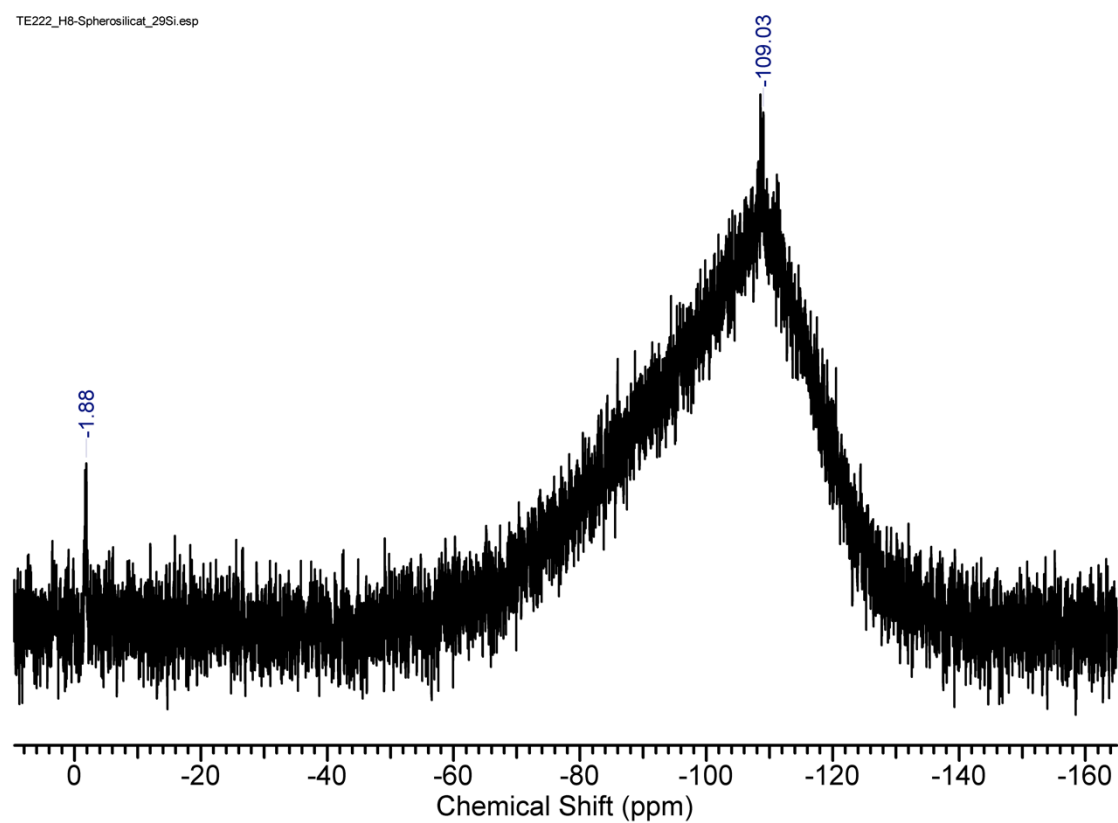
FIGURE SI3: ^{29}SI NMR OF $Q_8M_8^H$.

TE_MP2PDMS_1H.esp
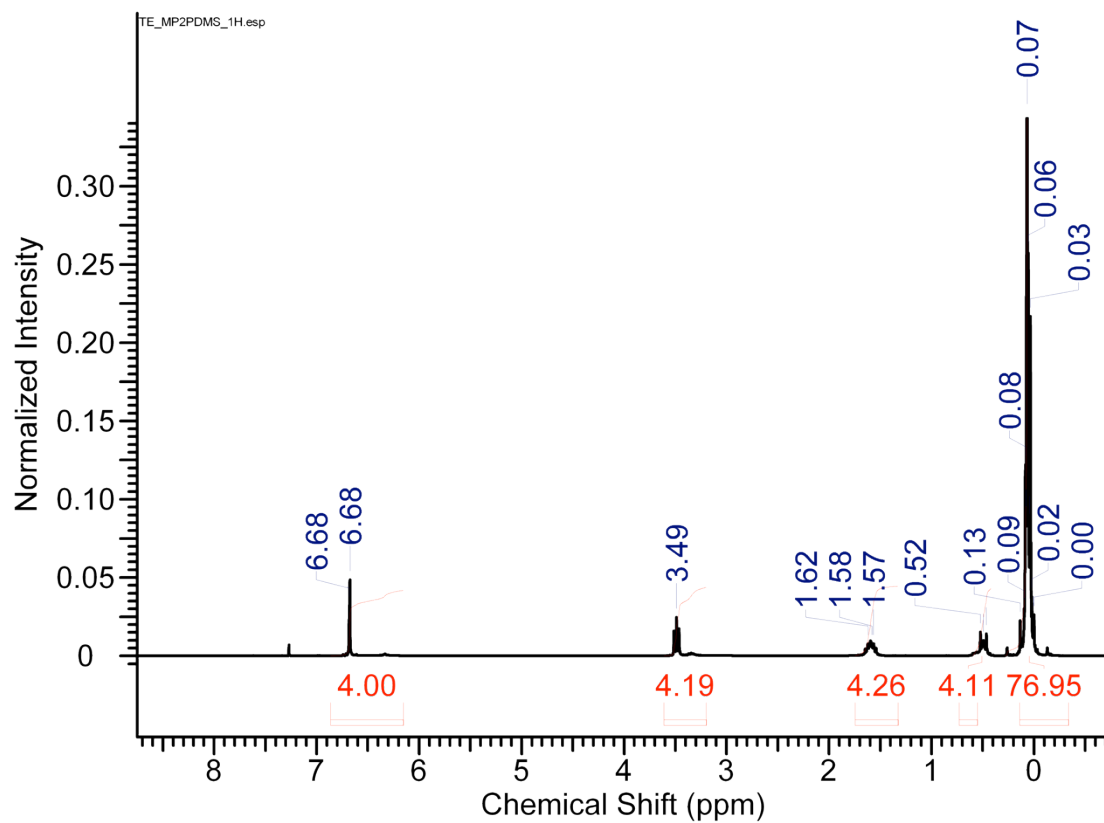
FIGURE SI4: ^{1}H NMR OF M$_2$-PDMS.

TE_MP2PDMS_13C.esp
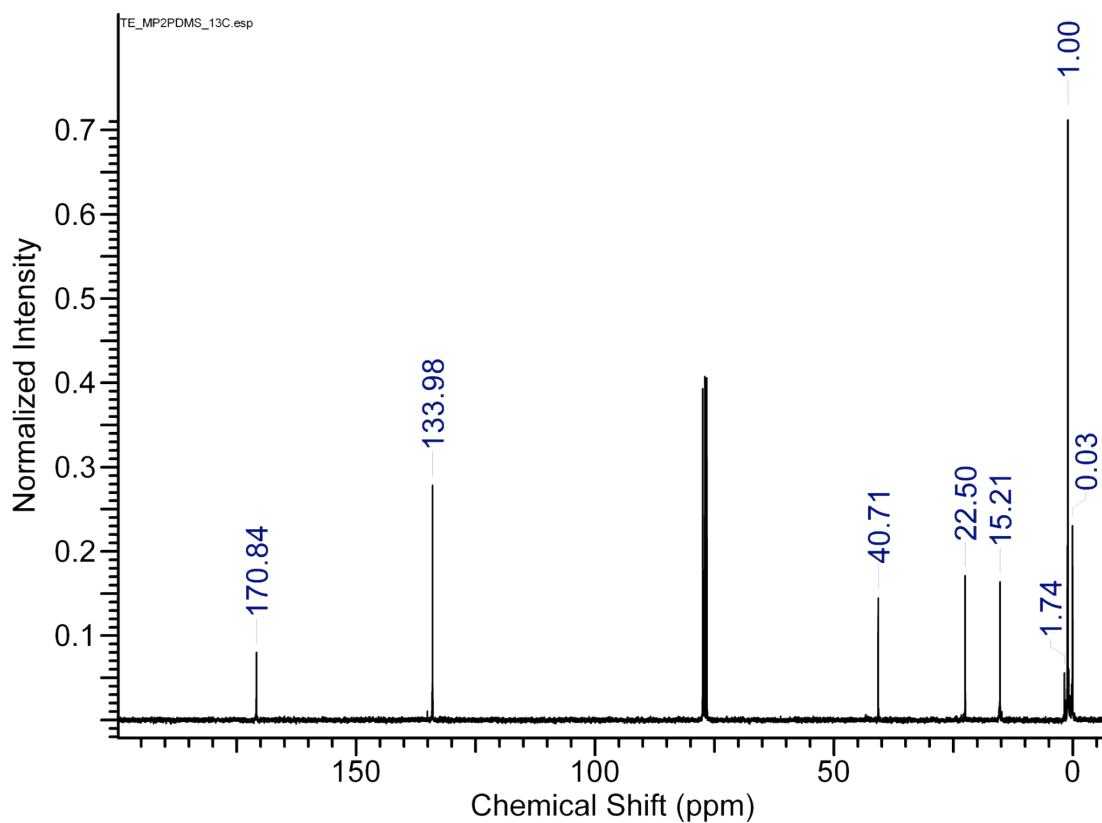
FIGURE SI5: ^{13}C NMR OF M$_2$-PDMS.

TE_MP2PDMS_29Si.esp
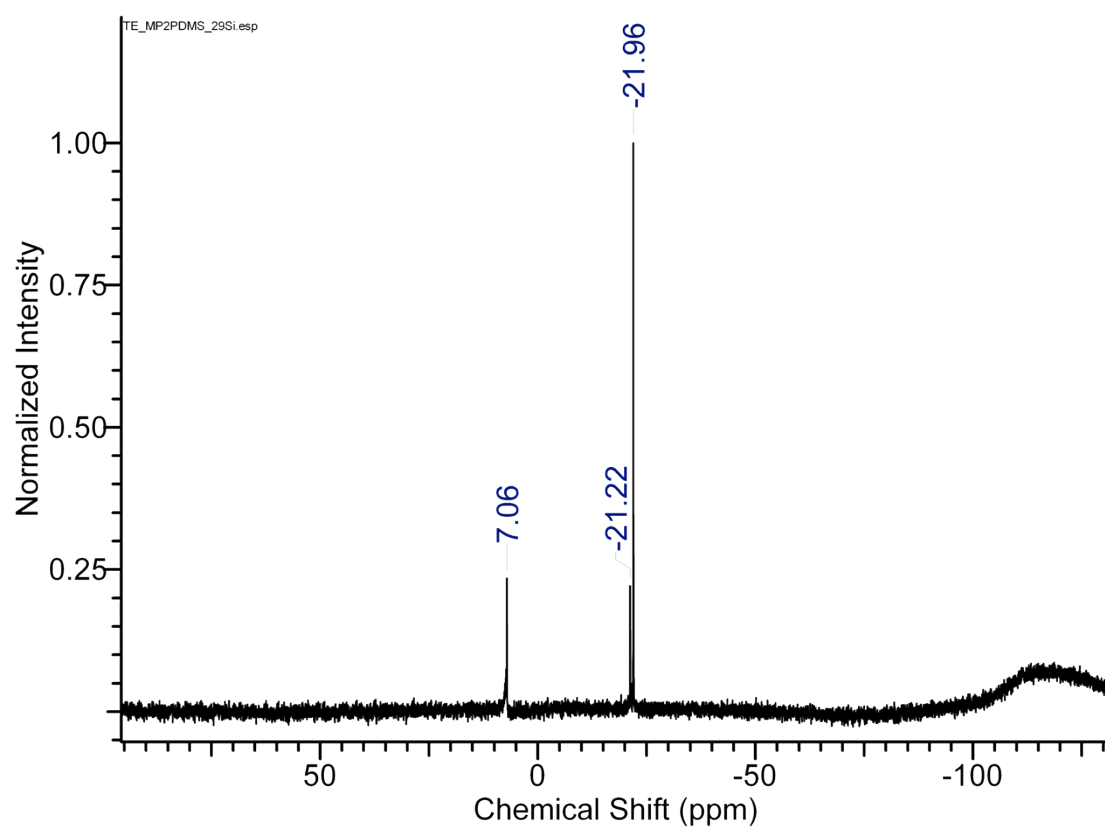
FIGURE SI6: ^{29}SI NMR OF M$_2$-PDMS.
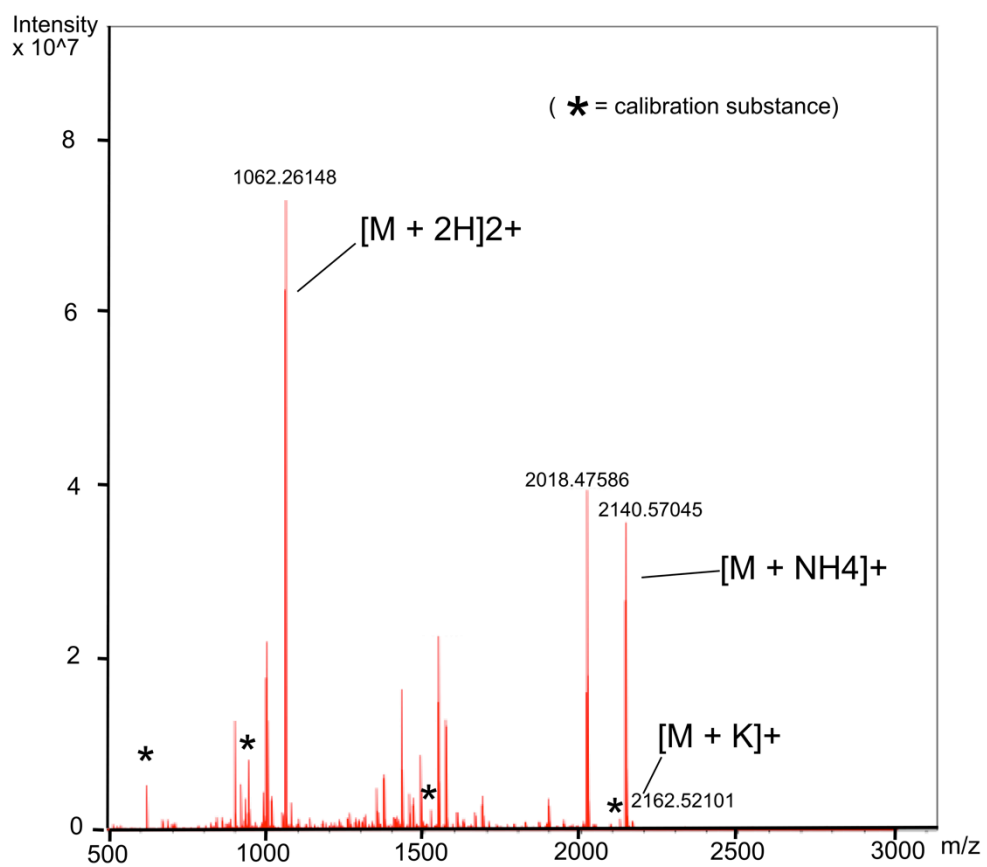
FIGURE SI7: ESI-MS SPECTRUM OF $Q_8M_8FAE_8$.
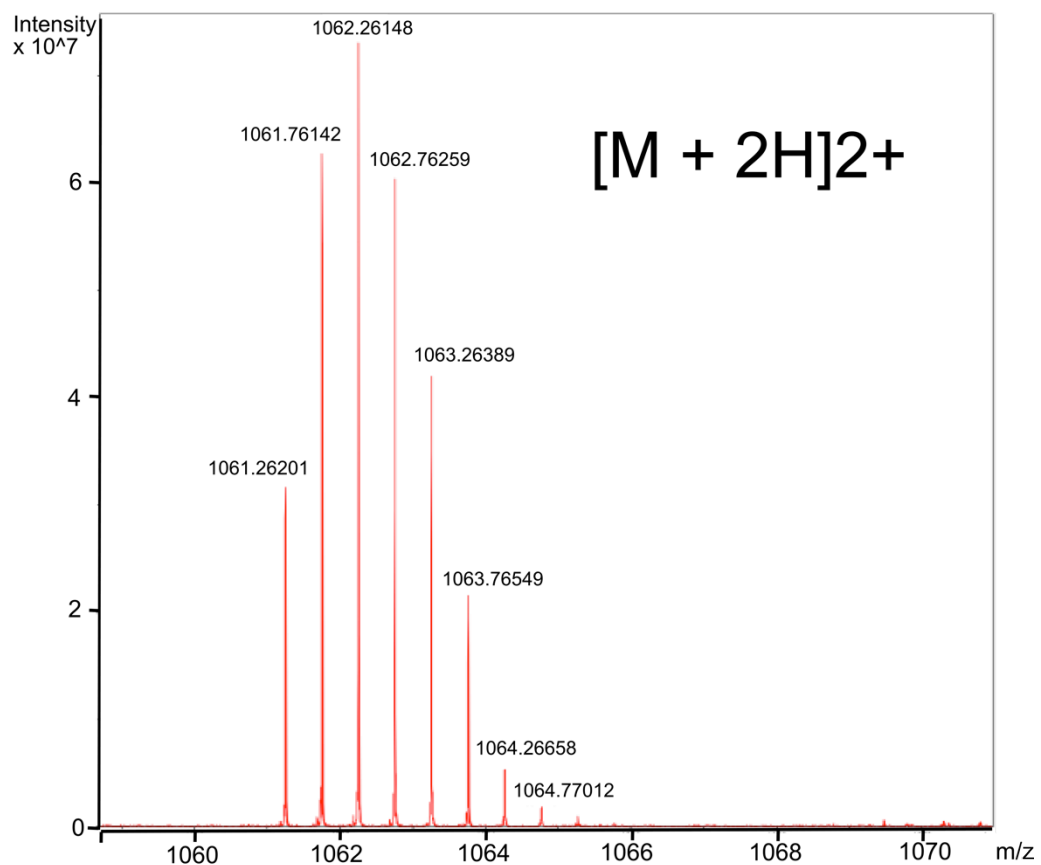
FIGURE SI8: ESI-MS OF $Q_8M_8FAE_8$ (DOUBLY CHARGED SPECIES)
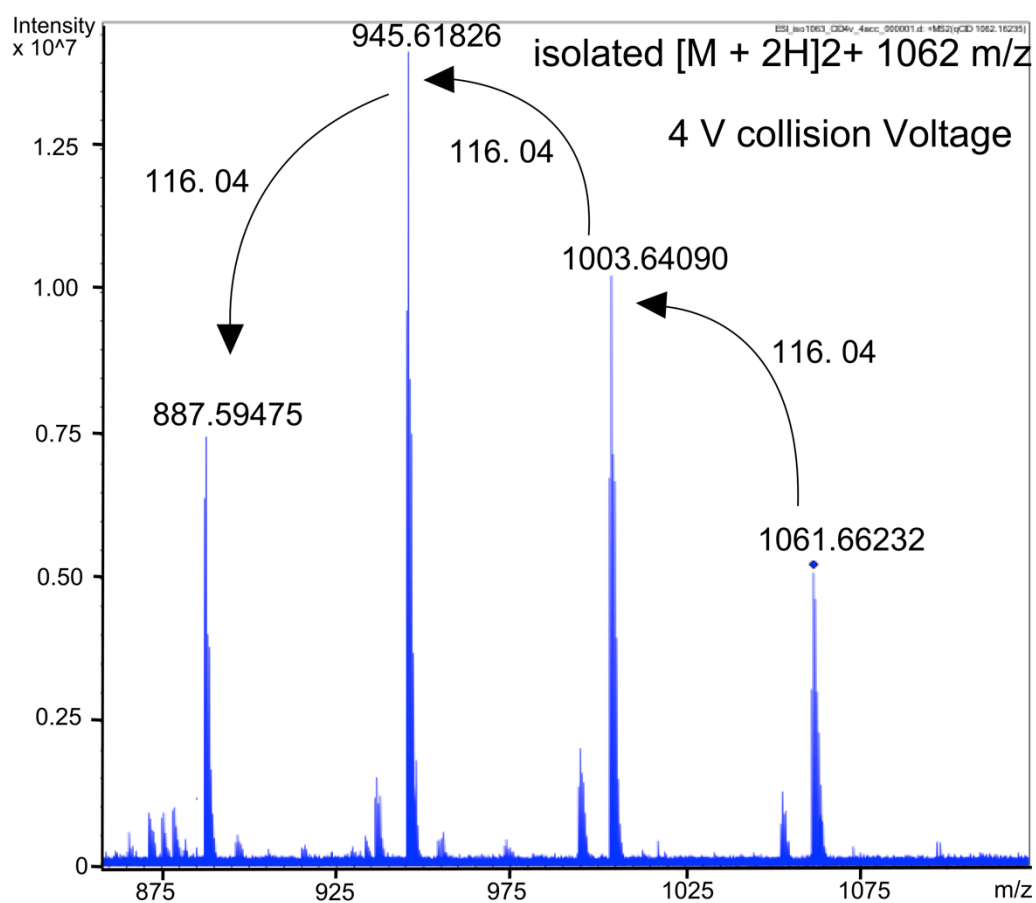
FIGURE SI9: MS/MS MODE, PRECURSOR IONS (1062 M/Z) WERE ISOLATED FIRST IN THE QUADRUPOLE AND EXTERNALLY ACCUMULATED IN THE HEXAPOLE FOR 0.1 S. FOR CID, 4 V COLLISION VOLTAGE WAS APPLIED.